

University of Alberta

Development and Testing of Insulating Shotcrete for the Application in
Underground Tunnels

by

Wei Victor Liu

A thesis submitted to the Faculty of Graduate Studies and Research
in partial fulfillment of the requirements for the degree of

Doctor of Philosophy

in

Mining Engineering

Department of Civil and Environmental Engineering

©Wei Victor Liu

Spring 2013

Edmonton, Alberta

Permission is hereby granted to the University of Alberta Libraries to reproduce single copies of this thesis and to lend or sell such copies for private, scholarly or scientific research purposes only. Where the thesis is converted to, or otherwise made available in digital form, the University of Alberta will advise potential users of the thesis of these terms.

The author reserves all other publication and other rights in association with the copyright in the thesis and, except as herein before provided, neither the thesis nor any substantial portion thereof may be printed or otherwise reproduced in any material form whatsoever without the author's prior written permission.

Abstract

The trapped geothermal heat in the infinite rock mass through which mine tunnels are excavated is a great threat to the safety of personnel and mine operating equipment in deep underground hot mines. In order to lessen the temperature inside the tunnel, a considerable amount of energy is being spent by the way of using ventilation and cooling systems to dissipate the heat. However, operational costs of the system increase quite considerably, especially as the mines get deeper. In this research, shotcrete is used both as a structural lining and as an effective thermal insulation to reduce the heat load on the ventilation and cooling system within such tunnels. The research was implemented in both the experimental and theoretical aspects.

The experimental aspect, focused on the development of thermal insulation shotcrete. Expanded perlite aggregate (EPA) was firstly introduced into cast concrete mixtures by replacing the sands volumetrically in different ratios. The obtained samples were under the tests of mechanical properties including unconfined compressive strength (UCS) and splitting tensile strength (STS), *etc.* And thermal properties were derived by the transient plane source (TPS) technique. About 22% to 80% thermal conductivity losses of samples were noticed with the EPA additions, however still with certain strength. And then field

shotcreting process was followed in the same mix design, it is found that the UCS and STS of most shotcrete samples were larger than that of cast samples, and the shotcreting process did not have obvious effects on the samples' thermal properties with regard to cast samples.

The theoretical aspect emphasised on the theoretical fundamental for thermal insulation on the surface of infinite rock mass. First, two-layered slab models were considered in both analytical and numerical means. Then, the cylindrical models that are more similar to tunnels for insulation were depicted further. Finally, a full three dimensional metal mine level was numerically simulated to evaluate the heat flow reductions in both full and partial insulation cases, on the basis of the thermal properties from the shotcrete. Results showed excellent heat load reductions in both full and partial insulations, with the developed shotcrete.

Acknowledgements

First, I sincerely give the greatest thanks to my supervisors, Dr. Derek Apel and Dr. Vivek Bindiganavile, for their continuous help and valuable friendship through my entire PhD program. Their professional guidance, innovative insights, and supportive encouragements are always the light of my academic road to overcome the darkness. I am also very grateful to Dr. Jozef Szymanski for his valuable suggestions and kind guidance on my research.

I would like to extend my gratitude to all the committee members for your precious time, comments and suggestions in my Doctoral final exam: Dr. Piotr Szmigiel, Dr. Doug Schmitt, Dr. Tim Joseph, Dr. Jozef Szymanski, Dr. Vivek Bindiganavile and Dr. Derek Apel. Special gratitude is given to Dr. Piotr Rudnicki for his great help in my previous Doctoral candidacy exam.

The experimental part formed a significant portion in this work. And every tiny progress involves the help of many staffs and students at the University of Alberta. Firstly, I am deeply thankful to our concrete lab technician Rizaldy Mariano, for his supportive attitude and actions in all my experiments. I also give my thanks to Greg Miller and Cameron West for the tests of elasticity modulus, the machinist Herb Green in Machine Shop for the manufacture of direct tensile test setup, and Robert Anusic in rock preparations and the direct tensile test setup. Many thanks

go to George Braybrook in the Scanning Electron Microscope (SEM) Laboratory for his help and patience on my shotcrete samples. I deeply acknowledge my colleagues Chaoshi Hu, Babak Nikbakhtan and Lang Liu for their great contributions to my shotcrete sample preparations. Also I would like to thank Farnaz Batool for her initial introduction to the usage of transient plane source (TPS) device and Nicolas Ginouse from Université Laval for the shotcrete experiment discussions.

The three dimensional numerical simulations were under great help from my colleague Mohammadali Sepehri, also lots of encouragements from him during all these years. Special thanks are given to him for all these things.

And I would like to give my deeply thanks to Chaoshi Hu, who acts as a brother to me during so many years. In my life and in my research, he is always my supporter.

And I wish to give my sincere gratitude to all my friends and the people who helped me through the program. Life is so good because of the help and love from you.

Finally, my greatest grateful words are dedicated to my wife Jingqi Sarah Yang; her endless love is always so patient and kind to support my completion of this research, and to my parents and parents-in-law for their unconditional love and support to me.

Table of Contents

Chapter 1 Introduction	1
1.1 Research background	3
1.2 Research scope	7
1.3 Research objective	8
1.4 Thesis outline	9
References	12
Chapter 2 Thermal characterization of a lightweight concrete containing expanded perlite for underground insulation	15
2.1 Introduction	15
2.2 Experiments	18
2.2.1 Materials	18
2.2.2 Mixes and test methods	18
2.3 Results and discussion	21
2.3.1 Density	21
2.3.2 Unconfined compressive strength	22

2.3.3 Splitting tensile strength	23
2.3.4 Direct tensile bond strength	25
2.3.5 Thermal conductivity and influence of moisture	26
2.3.6 Heat capacity	28
2.3.7 Thermal diffusivity	30
2.4 Conclusions	32
Tables in Chapter 2	34
Figures in Chapter 2	36
References	45
Chapter 3 Thermal properties of lightweight dry-mix shotcrete containing expanded perlite	49
3.1 Introduction	49
3.2 Material and methods	52
3.2.1 Materials and mixtures	52
3.2.2 Shotcreting process and sample preparation	53
3.2.3 Testing methods	55
3.3 Results and discussion	58

3.3.1 Density and water absorption.....	60
3.3.2 Unconfined compressive strength.....	63
3.3.3 Modulus of elasticity.....	65
3.3.4 Splitting tensile strength	66
3.4 Concluding remarks	71
Tables in Chapter 3	74
Figures in Chapter 3.....	76
References.....	88
 Chapter 4 Comparison of methods in theoretical analysis of thermal insulation for underground tunnels.....	 93
4.1 Introduction.....	93
4.2 One-dimensional slab model.....	96
4.2.1 Heat flow through one-dimensional slab model with a semi-infinite boundary	97
4.2.2 Analysis of heat flow through one-dimensional slab model with a finite length boundary	104
4.2.3 Equivalent overall heat transfer coefficient model	105

4.3 Discussion	106
4.3.1 Parameters used in analysis.....	106
4.3.2 Comparisons of models.....	107
4.3.3 Effects of thermal insulation in slab models.....	113
4.4 Effects of thermal insulation in cylindrical models	115
4.4.1 Analytical cylindrical model without insulation.....	115
4.4.2 Model K for cylindrical insulation.....	116
4.5 Concluding remarks	117
Nomenclature in Chapter 4	119
Tables in Chapter 4	121
Figures in Chapter 4.....	124
References.....	130
 Chapter 5 Theoretical study on cylindrical models of heat flow and thermo-elastic stress in underground tunnels.....	 133
5.1 Introduction.....	133
5.2 One-dimensional cylindrical model	136
5.2.1 Solutions for a cylindrical model with a semi-infinite boundary	138

5.2.2 ABAQUS model with finite length boundary.....	141
5.2.3 Theory related to thermal stresses.....	141
5.3 Discussion.....	143
5.3.1 Sources of parameters used in analysis.....	143
5.3.2 Comparative analysis of cylindrical models	144
5.3.3 Effects of thermal insulation.....	150
5.3.4 Thermal stresses.....	152
5.4 Concluding remarks	155
Appendix.....	157
Nomenclature in Chapter 5	158
Tables in Chapter 5	161
Figures in Chapter 5.....	163
References.....	170
Chapter 6 Full three-dimensional modelling for thermal insulation effects of shotcrete in a typical underground mine	172
6.1 Introduction.....	172
6.2 Numerical model.....	175

6.2.1 Field access	175
6.2.2 Geometry of model	175
6.2.3 Simulated scenarios	176
6.2.4 Heat transfer coefficient.....	177
6.2.5 Heat transfer modelling in ABAQUS®	178
6.3 Results and discussion	179
6.3.1 Temperature distribution.....	179
6.3.2 Factors affecting heat loads before applying shotcrete with EPA	180
6.3.3 Influence of virgin rock temperature on heat load reductions	181
6.3.4 Influence of thermal properties of the rock on heat load reductions .	182
6.3.5 Comparisons of partial-insulation tunnels	183
6.3.6 Benefits estimation.....	184
6.4 Conclusions.....	185
Appendix.....	187
Tables in Chapter 6	188
Figures in Chapter 6.....	191
References.....	198

Chapter 7 Conclusion..... 201

7.1 Research summary 201

7.2 Conclusions..... 202

7.3 Contributions..... 204

7.4 Recommendations for future research 205

List of Tables

Table 2-1 Mix proportions of experimental concrete	34
Table 2-2 Testing results of all five mixes.....	35
Table 3-1 Mix proportions of shotcrete and corresponding rebound	74
Table 3-2 Exponential fitting parameters for UCS with days.....	74
Table 3-3 Exponential fitting parameters for STS with days.....	75
Table 3-4 Heat capacity for shotcrete samples	75
Table 4-1 Models descriptions.....	121
Table 4-2 Input parameters	122
Table 4-3 Eigenvalues of Model F.....	122
Table 4-4 Thermal insulation effects in different models at 1 year	123
Table 5-1 Input parameters	161
Table 5-2 Thermal insulation effects at 1 year ($ Fo = 18.9 $).....	162
Table 6-1 Ventilation nodes and airflows.....	188
Table 6-2 Virgin rock properties.....	189
Table 6-3 Shotcrete properties	189
Table 6-4 Benefits of shotcrete containing EPA.....	190

List of Figures

Figure 2-1 The EPA used in the study	36
Figure 2-2 Aggregate size sieve analysis	36
Figure 2-3 The setup of direct tensile bond strength	37
Figure 2-4 The setup of TPS 1500	37
Figure 2-5 Relationship between EPA replacement percentage and concrete density	38
Figure 2-6 Relationship between EPA replacement percentage and UCS	38
Figure 2-7 UCS reduction with respect to P0 (Controlling mix)	39
Figure 2-8 Correlation between 28-day compressive strength and oven-dry density	39
Figure 2-9 Relationship between EPA replacement percentage and splitting tensile strength	40
Figure 2-10 Relationship between UCS and STS	40
Figure 2-11 Direct tensile testing photos at different failure locations	41
Figure 2-12 Direct tensile testing result	42
Figure 2-13 Relationship between EPA replacement percentage and thermal properties	42
Figure 2-14 Thermal conductivity and diffusivity reduction with respect to P0 ..	43

Figure 2-15 Relationship between moisture content and oven-dry conductivity (48hrs) reduction with respect to air-dry (48hrs) conductivity	43
Figure 2-16 Relationship between oven-dry conductivity, oven-dry diffusivity and oven-dry density.....	44
Figure 2-17 Relationship between predicted specific heat capacity and tested specific heat capacity	44
Figure 3-1 Grading distributions of sands, EPA and blended aggregates	76
Figure 3-2 Shotcreting against panels.....	77
Figure 3-3 Coring machine for the sample drilling	77
Figure 3-4 Test setup for modulus of elasticity	78
Figure 3-5 Test setup for UPV	78
Figure 3-6 TPS probe schematic and setup.....	79
Figure 3-7 Effects of EPA on densities of shotcrete.....	79
Figure 3-8 Effects of EPA on water absorptions of shotcrete.....	80
Figure 3-9 SEM images of small samples	80
Figure 3-10 UCS developments with days	81
Figure 3-11 EPA effects on UCS of shotcrete and cast samples	81
Figure 3-12 Stress-strain curves of shotcrete samples	82
Figure 3-13 Effects of EPA on the modulus of elasticity of shotcrete	82
Figure 3-14 STS developments with days	83

Figure 3-15 Correlation between UCS and STS	83
Figure 3-16 Original temperature data of SP25 from TPS	84
Figure 3-17 Thermal conductivity and diffusivity of samples.....	85
Figure 3-18 Linear fitting between moisture contents and the air-dry by oven-dry thermal conductivity ratio	86
Figure 3-19 Correlation between UPV and thermal conductivity	86
Figure 3-20 Correlation between UPV and thermal diffusivity.....	87
Figure 4-1 Schematic of underground temperature distribution.....	124
Figure 4-2 Temperature profiles of Model A, E and G at 1 year.....	124
Figure 4-3 Surface heat fluxes of Model A, E and G with time	125
Figure 4-4 Temperature changes of Model A, E and G with time at different locations	125
Figure 4-5 Sensitivity analysis of Model E's outer boundary length	126
Figure 4-6 Eigenvalues	126
Figure 4-7 Interface temperatures of Model B, F and H with time	127
Figure 4-8 Surface heat fluxes of Model B, F, and H with time.....	127
Figure 4-9 Surface heat fluxes of Model C and I with time	128
Figure 4-10 Surface heat fluxes of Model D and J with time	128
Figure 4-11 Integration for accumulated heat flux	129
Figure 4-12 Surface heat fluxes of Model C and M with time	129

Figure 5-1 Temperature field in cylindrical tunnel.....	163
Figure 5-2 Dimensionless surface temperature with dimensionless time.....	164
Figure 5-3 Temperature distributions at one year.....	164
Figure 5-4 Surface temperature gradient with time	165
Figure 5-5 Temperature gradient distributions at one year.....	165
Figure 5-6 Heat penetration depth (D_p) with time	166
Figure 5-7 ABAQUS solutions with different outer boundary lengths	166
Figure 5-8 ABAQUS solutions with different out boundary lengths (small time scale)	167
Figure 5-9 Integration of surface temperature gradient	167
Figure 5-10 Surface s_{11} with time	168
Figure 5-11 Surface s_{22} and s_{33} with time.....	168
Figure 12 u_{11} , s_{11} , s_{22} and s_{33} distributions at one year	169
Figure 6-1 Mine tunnel layout	191
Figure 6-2 Ventilation nodes and airflow distribution.....	191
Figure 6-3 Rock mass geometry	192
Figure 6-4 Cross section of tunnels	192
Figure 6-5 Shotcrete layer.....	193
Figure 6-6 Meshing of model	194
Figure 6-7 Temperature distribution.....	194

Figure 6-8 Close cut-view.....	195
Figure 6-9 Heat load in 4 different rocks with fully-insulated shotcrete CP0	196
Figure 6-10 Heat load reductions in 4 different rocks with different fully-insulated shotcrete	196
Figure 6-11 Schematic of heat flux vectors	197
Figure 6-12 Comparison of heat load reductions in Rock D for partial-insulations	197

List of Symbols

Chapter 2

f_c Unconfined compressive strength (MPa)

f_{STS} Splitting tensile strength (MPa)

R^2 Coefficient of determination of fitting

α Thermal diffusivity (m^2 / s)

k Thermal conductivity ($\text{W} / (\text{m K})$)

C_p Specific heat capacity ($\text{J}/(\text{kg K})$)

ρ Density (kg/m^3)

R_m Mass ratio of ingredients

T Temperature (K)

x, y, z Location on Cartesian coordinate system

q''' volumetric heat generation rate (W/m^3)

Chapter 3

L Sample length (mm)

D Sample diameter (mm)

t time (day), the unit in Equation (3.1) and Equation (3.2)

f_c Unconfined compressive strength (MPa)

a_1, b_1, c_1 Parameters obtained by curve fitting

- f_{STS} Splitting tensile strength (MPa)
- a_2, b_2, c_2 Parameters obtained by curve fitting
- R^2 Coefficient of determination of fitting
- α Thermal diffusivity (m^2 / s)
- k Thermal conductivity ($\text{W} / (\text{m K})$)
- $k_{A/O}$ Thermal conductivity ratio, $k_{A/O} = k_{air-dry} / k_{oven-dry}$
- C_p Specific heat capacity ($\text{J}/(\text{kg K})$)
- ρ Density (kg/m^3)
- $\Delta\bar{T}$ Average transient temperature increase (K)
- r The radius of the Kapton probe (m)
- t Measuring time (s), the unit in Equation (3.3)
- τ Dimensionless time $\tau = \sqrt{at}/r$
- P_o Output power (W)
- v Velocity (m/s)

Chapter 4

- D_p Heat penetration depth (m)
- T Temperature (K)
- T_0 Initial temperature (K)
- T_V Virgin rock temperature (K)
- T_R Reference temperature (K)

- T_a Air temperature (K)
- T_s Tunnel surface temperature (K)
- T_{in} Interface temperature (K)
- x Space coordinate (m)
- r Distance with respect to axis of cylindrical opening (m)
- r_o Cylindrical opening radius (m)
- δ Thickness of the insulation layer (m)
- L Outer boundary length (m)
- t Time (s)
- τ Ending time (s)
- k, k_1, k_2 Thermal conductivity (W / (m K))
- C_p Specific heat capacity (J/(Kg K))
- $\alpha, \alpha_1, \alpha_2$ Thermal diffusivity (m² / s)
- λ Dimensionless parameter α_2 / α_1
- K_s Expression for convenience: $K_s = \sqrt{\frac{\alpha_1}{\alpha_2}}$
- K_e Expression for convenience: $K_e = \frac{k_2 K_s}{k_1}$
- h Heat transfer coefficient (W / (m² K))
- h_{eff} Equivalent overall heat transfer coefficient (W / (m² K))
- θ Dimensionless temperature: $\theta = (T - T_V) / (T_a - T_V)$
- ζ Dimensionless length: $\zeta = x / \delta$

Fo Dimensionless time, known as *Fourier number*, $Fo = (\alpha t) / \delta^2$

Bi Dimensionless heat transfer coefficient, known as *Biot number*,

$$Bi = (h \delta) / k$$

q_s Surface heat flux (W/m^2)

Q_s Total accumulated heat flow through surface (J/m^2)

\bar{q}_s Average surface heat flux (W/m^2)

β Eigenvalues

p Parameter in Laplace transformation

$Re(p)$ Real part of p

Chapter 5

A_1, A_2 Integration constants

u variable for integration in *Bessel equations*, without any physical meaning

Y_0, Y_1, J_0, J_1 Bessel equations

D_p Heat penetration depth (m)

T Temperature (K)

T_0 Initial Temperature (K)

T_V Virgin rock temperature (K)

T_R Reference temperature (K)

T_a Air temperature (K)

T_s Tunnel surface temperature (K)

T_{in} Interface temperature (K)

r distance with respect to axis of cylindrical opening (m)

r_o Cylindrical opening radius after shotcreting (m)

r_{in} Cylindrical opening radius before shotcreting (m)

δ Thickness of the insulation layer (m)

t Time (s)

k, k_1, k_2 Thermal conductivity (W / (m K))

$\alpha, \alpha_1, \alpha_2$ Thermal diffusivity (m² / s)

α_e Linear coefficient of thermal expansion (1/K)

λ Dimensionless parameter α_2 / α_1

h Heat transfer coefficient (W / (m² K))

ψ Dimensionless temperature: $\psi = (T - T_V) / (T_a - T_V)$

ψ_s Surface dimensionless temperature: $\psi_s = (T_s - T_V) / (T_a - T_V)$

θ The angle in cylindrical coordinate system

G Dimensionless temperature gradient

G_s Tunnel surface dimensionless temperature gradient

Q_s Accumulative dimensionless surface temperature gradient

$\overline{G_s}$ The average tunnel surface dimensionless temperature gradient

G_p Goch-Patterson flux

ξ Dimensionless length: $\xi = r / r_o$

Fo Dimensionless time, known as *Fourier number*: $Fo = (\alpha_2 t) / r_o^2$

Bi Dimensionless heat transfer coefficient, known as *Biot number*:

$$Bi = (h r_o) / k_2$$

q_s Surface heat flux (W/m^2)

R Dimensionless time dependant outer boundary

ν Poisson's ratio

E Young's modulus (GPa)

u_r Radial displacement (m)

σ_r Radial stress (Pa)

σ_θ Tangential stress (Pa)

σ_z Axial stress (Pa)

u_{11} Dimensionless radial displacement: $u_{11} = u_r / r_o$

s_{11} Dimensionless radial stress: $s_{11} = \sigma_r / E$

s_{22} Dimensionless tangential stress: $s_{22} = \sigma_\theta / E$

s_{33} Dimensionless axial stress: $s_{33} = \sigma_z / E$

Chapter 6

h Heat transfer coefficient ($\text{W} / (\text{m}^2 \text{K})$)

List of Abbreviations

EPA	Expanded perlite aggregate
VRT	Virgin rock temperature
UCS	Unconfined compressive strength
STS	Splitting tensile strength
TPS	Transient plane source
Oven-dry	OD
Air-dry	AD
BC	Boundary condition
UPV	Ultrasonic pulse velocity
LVDT	Linear variable differential transducer
SEM	Scanning electron microscope

Chapter 1 Introduction

Deeper underground mining operations are being constructed all across the world, along with the booming global demands for mineral resources. The geothermal heat diffusing from rock mass into underground tunnels is proportional with the mining depth, and it has become a major concern as the heat hazards to restrain deeper underground mining developments (Hartman et al., 1998, Spalding, 1949). In deep mines, geothermal heat is actually the primary heat load contributor (Pickering and Tuck, 1997, Rawlins and Phillips, 2001), which approximately accounts for 50% to 90% of the total heat load depending on different geological conditions. Thus the geothermal heat control in underground hot mines is the most important and demanding issue to ensure a suitable working environment.

In order to excavate deeper for productions and ensure the health and safety of mine workers, mostly, a larger amount of mine ventilation and cooling capacity has to be installed to reduce this geothermal heat, until the required mine atmosphere conditions (Tuck, 1997) have reached, this in sequence causes an extra substantial energy consumption costs of the ventilation and cooling system. It is known that the costs of the ventilation and refrigeration system would increase exponentially along with greater depth (Bottomley and van Rensburg,

1987, Sheer et al., 1984). Therefore, it raises great concerns and motivations to reduce the geothermal heat loads into underground openings.

It is generally believed that the application of insulation layer of lower thermal conductivity on the rock surface of openings is an effective means to abate heat loads (Bottomley, 1985, Bottomley and van Rensburg, 1987, Chellam, 1992, Wagner, 2010). However, until now, thermal insulation in underground hot mines has not been widely applied yet. The reasons behind this fact can be divided into the following two categories. **First**, the strict criterions of insulation materials selection have narrowed the road of underground mine insulation. Since the insulation layer in application is expected to perform well in some of the key aspects, for instance, the thermal resistance, flammability, toxicity, durability, mechanical strength, field logistics, and price, *etc.* Take one case for example, polyurethane was proposed in mine insulation before by previous researchers (Bottomley and van Rensburg, 1987), in that study, the polyurethane does have the benefits of thermal insulation. However, it does not meet the criterions in flammability and toxicity, and it is also costly for the raw materials, besides, additional logistics has to be applied exclusively for its usage. Thus, the application of the insulation polyurethane can be very tough. **Second**, the theoretical fundamental and mechanism of using insulation in underground hot mines are not adequate enough to describe its effects in insulation applications.

This specific thermal insulation is actually the transient heat conduction problem in a semi-infinite virgin rock mass applied with a finite length insulation layer that has heat convection and radiation boundary with the ventilation air. However, inadequate systematic mathematical explanations and descriptions have been found in regard to the insulation effects in underground openings. For example, Bottomley (Bottomley, 1985) used an equivalent heat transfer coefficient support the theory to use thermal insulation in underground openings, without explaining any more details. Ashworth (Ashworth, 1992) used heat conduction analytical solutions in steady state, even this is in practice a time-dependant transient conduction problem.

1.1 Research background

In 1994, the U.S. Bureau of Mines (USBM) (USBM, 1994) initiated the idea of using a new type of shotcrete for thermal insulation in deep underground hot mines by adding expanded perlite into the shotcrete mixture, holding the compressive strength of 20.68 MPa at 90 days, and a 25% reduction of geothermal heat loads. In other words, their newly developed shotcrete not only performs well as the rock support, but also functions excellently as the insulation layer. Unfortunately, this research was abandoned hastily due to the sudden closure of USBM in 1995. Inspired by the promising preliminary results provided

by USBM, continuing research in shotcrete containing expanded perlite has been conducted by the research group including the current author. In order to improve the understanding of this research, it is necessary to introduce the backgrounds of both the expanded perlite and shotcrete in the subsequent paragraphs.

Raw perlite is a natural siliceous volcanic rock that is in the amorphous and glassy form of magma containing 2-5% water (Kramar and Bindiganavile, 2010). The raw perlite would undergo substantial volume expansion from 4 to 20 times above the temperature of 870°C (Ciullo, 1996) after the evaporation of water, it results in producing the porous lightweight expanded perlite. The expanded perlite has been widely used in concrete or mortar as building materials for its excellent performance at thermal and acoustical insulation, fire resistance and reduced weight. Perlite applications include but are not limited to the tile, stucco, pool, brick, block/masonry, slab, roof deck, roof fill, pipe coating, oil-gas and geothermal wells, *etc* (Anon, 1961, Gallus et al., 1979, Singh and Garg, 1991). Early in 1940s, expanded perlite was used as lightweight aggregates in the concrete field (Brouk, 1949) to manufacture the lightweight structural concrete block, in which the expanded perlite aggregates (EPA) were blended with normal aggregates in a proper percentage to get enough strength and good property of thermal insulation.

The shotcrete technique, with concrete sprayed pneumatically on the rock surface, is frequently used in support of underground openings after the excavation. The fundamental difference between shotcrete and normal concrete is that the shotcrete is compacted by its own high momentum after shooting. In 1907, shotcrete process was firstly invented and used by Carl Akeley to repair a museum in Chicago (Morgon, 2006), and then in 1930s, shotcrete started to be introduced for the application of underground rock support, to prevent rock fall (Morgan, 1991). After 1970s, there was a rapid development of shotcreting for the use in underground rock support, and currently, the mining industry has become a major consumer of shotcrete, whose annual consumption is estimated to be over 200,000 m³ in North America (Rispin and Brooks, 2001).

As introduced above, since shotcrete is routinely used in underground mines, adding expanded perlite into shotcrete would not add any extra costs on field logistics. And expanded perlite itself does not have any toxicity according to mice experiments (Sakai and Nagao, 1985), besides, expanded perlite is widely used as fire retardants to reduce the flammability of other materials (Kasai et al., 1979). Moreover, the costs of expanded perlite in volume are very low (Bolen, 2004), thanks to its low bulk density of about 71 kg/m³ (Liu et al., 2011). Therefore, most the criterions of materials selections are met for the usage of shotcrete containing expanded perlite in underground mine insulation. Only the thermal

resistance and mechanical performances, these two key criteria are left to be studied.

The theoretical analysis has two distinctive parts. The first part is the analytical analysis, namely, the analysis of solutions from closed-form mathematical equations generated from principles of heat transfer (Sukhatme, 2011). One difficulty is in determining the outer boundary in the infinite rock mass region. In addition, the application of insulation layer makes it even more complicated because of the two-layered system. Even with this assumption by considering it as a one dimensional transient heat conduction problem in a two-layer slab, namely, the finite length insulation layer and the infinite rock mass layer. The analytical solutions of simplified transient conduction in composite slabs are still found to be too sophisticated to solve, especially the solutions relating to eigenvalues, even in the most recent studies for the theory of heat transfer (de Monte, 2000, de Monte 2006, Lu and Tervola, 2005, Sun and Wichman, 2004).

The second part is the numerical analysis, executed in the finite element method (FEM) based ABAQUS[®] software (Abaqus Users Manual), as the FEM is currently the mainstream numerical tool in rock engineering, because of its benefits and maturity in processing the non-linearity and in-homogeneity of rock mass, the complexity of opening geometry, rock/structure interaction and the tunneling method (Jing, 2003, Jing and Hudson, 2002, Liu et al., 2008). Further,

ABAQUS[®] is an available powerful commercial FEM software which has a wide application in thermal analysis, as well as the mechanical stress analysis (DSIMULIA). Generally speaking, analytical analysis with specific mathematical solutions is considered as the most precise and reliable source, however, the analytical solutions depend heavily on the simplified model geometries with limited input parameters. The more practical way is to use the numerical analysis, which is more compatible of solving real problems which have complicated geometries with non-linear and non-homogeneous conditions; nevertheless, the accuracy and trustworthiness of the numerical analysis are doubted without confirmation from the analytical analysis. Therefore, both the analytical analysis and numerical analysis are compared in this research to clarify the feasibility of thermal insulation in underground mines. Before going to large scale model, the numerical models are verified firstly by comparing with analytical models in details. Then a large mine level scale is to be studied for the evaluation of thermal insulation with the newly developed shotcrete.

1.2 Research scope

The research has concentrated on the development of shotcrete with low thermal conductivity for the insulation applications in underground hot mines. Taking the advantage of low thermal conductivity, the insulation shotcrete layer on the rock

surface of mine openings serves as a thermo-barrier to partially block the heat flow from rocks to the mine atmosphere. Moreover, the structural role of shotcrete as the rock support has also been evaluated according to systematic experiments for its various mechanical properties. Furthermore, based on the newly developed insulation shotcrete, the effects of the thermal insulation by shotcrete have been assessed by theoretical analysis in both analytical and numerical ways, from single tunnel scale to full mine level scale. The theoretical fundamental and mechanism of thermal insulation in the infinite hot rock mass have been extensively studied and explored.

1.3 Research objective

The primary objective is to develop a new type of shotcrete by adding expanded perlite aggregate (EPA) into the mixture, on the purpose of improving the thermal performance for mine insulation. At the same time, the mechanical performance of shotcrete is ensured for structural use in underground support. Another objective is to deduct and describe the theoretical fundamental and mechanism of thermal insulation in underground openings surrounded by infinite rock mass. Based on the theory, the assessments of thermal insulation effects are going to be concluded for applications and practical guidance.

1.4 Thesis outline

This thesis is presented in a paper based format, conforming to which, the major chapters, from Chapter 2 to Chapter 6, are 5 contributions to the thermal insulation shotcrete developments and applications. Among them, Chapter 2 and Chapter 3 focus on the new shotcrete developments and its properties; And from Chapter 4 to Chapter 6, these 3 chapters emphasize on the theoretical fundamental and mechanism of thermal insulation by using the innovated shotcrete in this research. The summary of each chapter is briefly introduced as follows.

Chapter 2 aims to investigate the use of expanded perlite aggregate (EPA) in mortar, a simulated shotcrete, for further application of shotcrete to thermal insulation of underground mines. Mixes were designed according to the typical proportions of underground shotcrete, with the sand volumetrically substituted by expanded perlite. Tests of samples were conducted at four ages. Transient plane source technique was utilized to measure the thermal properties. The results showed reduced weight, decreased thermal conductivity, deteriorated thermal diffusivity, and sacrificed mechanical strength with perlite addition.

Chapter 3 has the aim to apply thermal insulation on hot mines by introducing the lightweight expanded perlite aggregate (EPA) into shotcrete. Mixes containing different EPA portions were sprayed out through dry-mix shotcreting machine into standard testing panels for mechanical and thermal properties test.

Mechanical properties from a series of tests, including density, uniaxial compressive strength (UCS), modulus of elasticity, splitting tensile strength (STS), and ultrasonic pulse velocity (UPV), were investigated in various ages. Moreover, the transient plane source technique was employed to measure shotcrete's thermal properties, and the influence of moisture contents, respectively. The results illustrated the reduced density, sacrificed UCS, STS, modulus of elasticity and UPV with additions of EPA, and the benefits of decreasing thermal conductivity and diffusivity for thermal insulation. It is found that UCS and STS were larger for shotcrete whereas its thermal properties demonstrated no obvious difference comparing with cast samples in same proportions.

Chapter 4 concerns about the heat flow through the parent rock mass and the rock-insulation interface as well as the insulation itself. The thermal characteristics, accompany with heat flow through the semi-infinite rock mass and the insulation layer were made analytically and numerically using a variety of slab models as applicable to underground mines. The results derived were thought to be sufficiently accurate for practice. And promising heat abatement effects from insulation were observed in these theoretical models with good agreement.

Chapter 5 has analysed the heat flow and the induced thermal stresses in both analytical and numerical cylindrical models. Further, thermal insulation effects of shotcrete were also evaluated with these theoretical models and it is found that all

the models gave results in close agreements with one another. Therefore, this study has provided the theoretical proof for advantages in applying shotcrete as the thermal insulation layer in underground mines.

Chapter 6 has conducted a full three dimensional numerical simulation based on a typical deep underground metal mine in North America. The field data of airflows in the ventilation system was adopted to define the inner boundary of tunnels. The results have confirmed the fact that innovated shotcrete applied either fully or partially around the tunnels can achieve excellent heat load reduction effects.

Chapter 7 is the summery and conclusions of this thesis as well as the future research recommendations.

References

- Abaqus Users Manual, V. 6.10-1. *Dassault Systemes Simulia Corp., Providence, RI.*
- Anon (1961) Perlite roof deck and insulating concrete. *Concrete Construction*, 6, 95-97.
- Ashworth, E. (1992) Heat flow into underground openings: Significant factors. *Mining Engineering*. University of Arizona, USA.
- Bolen, W. P. (2004) Perlite, by U.S. Geological Survey.
- Bottomley, P. (1985) The reduction in heat flow due to the insulation of rock surfaces in mine airways. *2nd US Mine Ventilation Symposium*. Reno, NV.
- Bottomley, P. & van Rensburg, B. (1987) The insulation of rock surfaces-an empirical study. *Journal of the Mine Ventilation Society of South Africa*, 40, 41-45.
- Brouk, J. J. (1949) Perlite aggregate: Its properties and uses. *Journal of the American Concrete Institute*, 46, 185-190.
- Chellam, S. (1992) Thermal insulation of underground mine workings at deep levels. *Department of Mining Engineering*. Rapid City, South Dakota, South Dakota School of Mines and Technology.
- Ciullo, P. A. (1996) The industrial minerals. *Industrial minerals and their uses: a handbook and formulary*. Westwood, New Jersey, Noyes Publication.
- de Monte, F. (2000) Transient heat conduction in one-dimensional composite slab. A natural analytic approach. *International Journal of Heat and Mass Transfer*, 43, 3607-3619.
- de Monte , F. (2006) Multi-layer transient heat conduction using transition time scales. *International Journal of Thermal Sciences*, 45, 882-892.
- DSIMULIA (2004) Heat Transfer and Thermal-Stress Analysis with Abaqus.
- Gallus, J. P., Watters, L. T. & Pyle, D. E. (1979) Performance of oilwell cementing compositions in geothermal wells. *Old SPE Journal*, 19, 233-241.
- Hartman, H. L., Mutmansky, J. M., Ramani, R. V. & Wang, Y. J. (1998) Environmental control of the mine atmosphere. *Mine ventilation and air conditioning. Third Edition*.
- Jing, L. (2003) A review of techniques, advances and outstanding issues in numerical modelling for rock mechanics and rock engineering. *International Journal of Rock Mechanics and Mining Sciences*, 40, 283-353.

- Jing, L. & Hudson, J. A. (2002) Numerical methods in rock mechanics. *International Journal of Rock Mechanics and Mining Sciences*, 39, 409-427.
- Kasai, A., Yamagishi, K., Komazawa, K., Ito, H. & Nunomura, A. (1979) Fire-retardant boards made of pulp sludge and perlite, 5: The effect of thickness and rock-wool fiber on the flammability and bending strength of the boards. *Journal of the Hokkaido Forest Products Research Institute*.
- Kramar, D. & Bindiganavile, V. (2010) Mechanical properties and size effects in lightweight mortars containing expanded perlite aggregate. *Materials and Structures*, 44, 735-748.
- Liu, H. Y., Small, J. C. & Carter, J. P. (2008) Full 3D modelling for effects of tunnelling on existing support systems in the Sydney region. *Tunnelling and Underground Space Technology*, 23, 399-420.
- Liu, W. V., Apel, D. B. & Bindiganavile, V. (2011) Thermal characterisation of a lightweight mortar containing expanded perlite for underground insulation. *International Journal of Mining and Mineral Engineering*, 3, 55-71.
- Lu, X. & Tervola, P. (2005) Transient heat conduction in the composite slab-analytical method. *Journal of Physics A: Mathematical and General*, 38, 81.
- Morgan, D. R. (1991) Steel fiber reinforced shotcrete for support of underground openings in Canada. *Concrete International*, 13, 56-64.
- Morgon, D., R. (2006) Advances in shotcrete technology for infrastructure rehabilitation. IN Morgon, D., R. (Ed.) *Shotcrete: A Compilation of Papers*.
- Pickering, A. J. & Tuck, M. (1997) Heat: sources, evaluation, determination of heat stress and heat stress treatment. *Mining Technology*, 79, 147-56.
- Rawlins, C. A. & Phillips, H. R. (2001) Reduction of mine heat loads. *7th International Mine Ventilation Congress*. Krakow, Poland.
- Rispin, M. & Brooks, J. (2001) A shotcrete in North American underground mines: Yesterday, today and tomorrow. *CIM bulletin*, 94, 76-79.
- Sakai, T. & Nagao, S. (1985) Twenty-eight week toxicity study of perlite powder in mice. *The Journal of toxicological sciences*, 10, 83.
- Sheer, T. J., Burton, R. C. & Bluhm, S. J. (1984) Recent developments in the cooling of deep mines. *The South African Mechanical Engineer*, 34.
- Singh, M. & Garg, M. (1991) Perlite-based building materials -- a review of current applications. *Construction and Building Materials*, 5, 75-81.
- Spalding, J. (1949) *Deep Mining*. Mining Publications, London.
- Sukhatme, S. P. (2011) Transient and multidimensional heat conduction. *A Text Book on Heat Transfer*. Cambridge, Massachusetts, Phlogiston Press.

- Sun, Y. & Wichman, I. S. (2004) On transient heat conduction in a one-dimensional composite slab. *International Journal of Heat and Mass Transfer*, 47, 1555-1559.
- Tuck, M. A. (1997) Control of mine climate. *Mining Technology*, 79, 215-220.
- USBM (1994) An 'insulating' shotcrete for heat abatement in deep mines. *Technology News* 434.
- Wagner, H. (2010) The management of heat flow in deep mines / . Management von Wärmeströmen in tiefliegenden Bergwerken. *Geomechanics and Tunnelling*, 3, 609-621.

Chapter 2 Thermal characterization of a lightweight concrete containing expanded perlite for underground insulation¹

2.1 Introduction

With deeper mineral exploitations in Canada and other mining countries, the temperature in the earth's crust increases substantially with depth, on average 25-30°C/km in most countries (Fridleifsson et al., 2008). For example, the local rock temperature could reach approximately 80°C at the mining depth of 2000 m in an Arizona copper deposit (ADMMR, 2004). In deep mines, geothermal heat is considered to be the primary heat load contributor (Pickering and Tuck, 1997, Rawlins and Phillips, 2001), which accounts for 50% to 90% of the total heat load depending on different geological conditions. Thus the geothermal heat control in underground mines is the most important and demanding issue to ensure a suitable working environment. Currently, most Canadian mines are using the ventilation and cooling systems to control the underground mine climate (Hall et al., 1984). However, total energy consumption and operational costs increase significantly at greater mining depths, larger ventilation and refrigeration

¹ A version of this Chapter has been published as a journal paper: Liu, W. V., Apel, D. B. & Bindiganavile, V. (2011) Thermal characterisation of a lightweight mortar containing expanded perlite for underground insulation. *International Journal of Mining and Mineral Engineering*, 3, 55-71.

requirements, as well as tighter environmental health and safety regulations. Therefore, among those geothermal heat control methods, the one which can reduce geothermal heat loads and ventilation and refrigeration requirements simultaneously for the benefit of energy conservation is urgently demanded. Many studies (Bottomley, 1985, Bottomley and van Rensburg, 1987, Chellam, 1992, Howarth and Gillies, 1987) have proved that an excellent candidate is the use of low heat conductive materials with enough mechanical strength for mine insulation. The insulation layer on the rock surface of mine openings serves as a thermo-barrier to reduce the heat flow from the rock to the mine atmosphere. Insulation is also considered to be the most cost-effective technique for carbon dioxide abatement, in terms of energy conservation (Enkvist et al., 2007). Previous studies (Bottomley, 1985) reported a 50-70% reduction of geothermal heat load in the fully-insulated situation, and a 25-40% reduction in the partially-insulated case (un-insulated floor of tunnel). Since the energy consumption in cooling systems reduces correspondingly with the heat load abatement, a fair amount of energy can be saved by insulation. However, until now, the insulation technique has not been widely used in hot mines around the world due to lack of appropriate insulation material.

The shotcrete technique, with concrete sprayed pneumatically on the rock surface, is frequently used in support of underground openings. Better thermal properties

can be expected with the addition of some lightweight aggregates described in ASTM C332 (ASTM, 2009a). In 1994, the U.S. Bureau of Mines (USBM) (USBM, 1994) initiated the idea and the experiment to produce an improved shotcrete for heat insulation in deep mines by adding expanded perlite into the mixture, with the compressive strength of 20.68 MPa at 90 days, and a 25% reduction of geothermal heat load. It means that the improved shotcrete may not only perform well in mine support, but may also function excellently in rock insulation. Unfortunately, this promising work was suddenly stopped due the closure of USBM in 1995. Therefore, it is quite necessary and viable to conduct experiments and analysis for the insulation shotcrete application on the purpose of carbon abatement and energy conservation.

Raw perlite is a kind of naturally occurring siliceous volcanic rock, which is in the amorphous and glassy form of magma containing 2-5% water (Kramar and Bindiganavile, 2010). The water would be vaporized to expand the volume substantially from 4 to 20 times above the temperature of 870°C (Ciullo, 1996), to end up producing the lightweight porous expanded perlite. Expanded perlite has been widely used for its good properties in thermal and acoustical insulation, fire resistance and reduced weight (Ciullo, 1996). However, little literature was found in its mining application.

In the interest of insulation shotcrete research, expanded perlite was selected as the replacement aggregate, also termed as expanded perlite aggregate (EPA), to preliminarily investigate the use of EPA in cast mortars, holding with the next plan to further the study in shotcreting technology.

2.2 Experiments

2.2.1 Materials

In this experiment, Type GU Portland cement (CSA, 2009) was used. The expanded perlite aggregate (EPA) as shown in Figure 2-1 was obtained from a local supplier in Canada. The water absorption and bulk density of the EPA were 100% and 71.49 kg/m^3 , individually. The water absorption and bulk density of the sands were 2.04%, 1675.67 kg/m^3 , respectively. Figure 2-2 states the results of sieve analysis of sand and EPA, both of them distribute in the ACI shotcrete aggregate zone #1 (ACI, 2005) as demonstrated in Figure 2-2. No other chemical admixtures were added.

2.2.2 Mixes and test methods

In order to preliminarily simulate the underground shotcrete, the typical underground ordinary wet-mix shotcrete proportions were consulted in the mix design (ACI, 2009). Five mixes were prepared using 0%, 25%, 50%, 75% and 100% replacement ratios of sand by EPA, shown as P0 to P100, respectively. The

mix proportions are shown in Table 2-1. Water/cement ratio was kept as 0.45 in all five mixes. The EPA and sand were pre-soaked in water, which were calculated from the water absorption of EPA and sand, separately, so that the absorption of aggregates would not affect the water/cement ratio. A laboratory drum mixer was used for mixing the entire batch. The making and curing procedure of test samples complied with ASTM C192 (ASTM, 2007). For each mix, forty-seven cylindrical samples in the size of 75 mm diameter \times 150 mm height were prepared for unconfined compressive strength (UCS), splitting tensile strength (STS) and thermal properties tests. Tests for each mix were conducted at four different curing ages (1st day, 3rd day, 7th day, 28th day). For each age, three samples were for the UCS of the concrete, in accordance with ASTM C39 (ASTM, 2009b), eight samples were for the STS, in accordance with ASTM C496 (ASTM, 2004a). Three left-over samples were for the thermal test as well as some further tests.

2.2.2.1 Setup of direct tensile bond strength test

Moreover, typical rocks including sandstone, limestone and granite were used in this study for the investigation on the bond strength between these concrete mixes and rocks. As illustrated in Figure 2-3, direct tensile testing setup per ASTM D2936 (ASTM, 2008) was designed for pure direct tensile loading. The key

component of the design can be seen in Figure 2-3(a), two roller chains connected to steel heads function as straight linkages to make sure the tensile loading is in the line of the same plane without bending. And the sample preparation of this bond strength test can be interpreted under the help of Figure 2-3(b). First, rock sample were cored out into the diameter of 50 mm, and then the length of rock cores were cut to 50 mm by using a diamond rock saw to obtain a sound roughness (Austin et al., 1995, Austin et al., 1999) for all the rock samples; After this, rocks samples were pre-placed into the cylindrical molds of 50 mm diameter and 100 mm height. Second, these five concrete mixes were casted into theses rock occupied molds, and then after curing for 28 days, the bonded samples were taken out from the molds, and the concrete ends were cut by the diamond rock saw to obtain the sample length of 100 mm. At last, the rock-concrete samples were adhered to steel heads by the high strength glue, and curing for at least 24 hours for the loading test.

2.2.2.2 Setup of the test of thermal properties

The thermal properties were tested by the Thermal Constants Analyzer TPS 1500, which uses the transient plane heat source method (TPS) described by ISO 22007-2.2 (ISO, 2008). The transient plane heat source method, or hot disk technique, based on the three-dimensional non-steady state heat conduction in the

sample, was firstly proposed and described by Gustafsson (Gustafsson, 1967, Gustafsson, 1990) , then the theory was discussed and analyzed in details from the first principles in heat conduction by He (He, 2005). The TPS 1500 device can rapidly measure the thermal conductivity at a range of 0.01 to 400 W/(m·K), the volumetric heat capacity up to 5 MJ/(m³·K), the thermal diffusivity from 0.1 to 100 mm²/s, with an accuracy better than 5%, and a reproducibility better than 1%, the measuring time can be adjusted from 20 to 1280 seconds. The cast cylindrical sample was sliced into two or more pieces using a rock saw, to 18.5 mm in thickness, which was calibrated to be larger than the probing depth. Surfaces of the pieces must be flat enough to ensure good thermal contact. In the tests, with a 6.403 mm radius Kapton probe, an output power of 0.23 W, and a measuring time of 30 s were calibrated by several comparative tests. The TPS 1500 used in this study is shown in Figure 2-4.

2.3 Results and discussion

2.3.1 Density

Figure 2-5 and Table 2-2 demonstrated the fresh, 28th day hardened and oven-dry densities of the mixtures with different EPA volume proportions. It is observed that all the three densities had an apparent decreasing trend with the increased amount of EPA, due to the porous structure and much lower bulk density of EPA.

For the oven-dry density, the highest value was 2139.21 kg/m³ at P0, and the lowest one was 1169.07 kg/m³ at P100.

2.3.2 Unconfined compressive strength

The results of the unconfined compressive strength (UCS) tests were summarized in Figure 2-6 and Table 2-2. For each mix, the compressive strength increased with the curing ages. It is also found that the 1st day compressive strength was much of the same for all mixes, and both the 3rd and 7th day strength in all mixes showed a decreasing trend except P25 and P50, which had similar values, whereas the 28th day strength displayed clear reductions with the increasing EPA replacement ratio. The overall trend shows that UCS decreased with the addition of EPA, however, it is interesting to notice that the UCS of P50 was larger than that of P25 at the 3rd and 7th day, that is in contrast with the overall trend, this contrast between P25 and P50 may be attributed to the early pozzolanic effect of EPA, which has rich contents of SiO₂ and Al₂O₃, it is probably the P50 mixture had a stronger pozzolanic strength effect caused by EPA than the P25 did during those two early ages, this EPA pozzolanic effect was also found in other studies (Demirboğa et al., 2001, Erdem et al., 2007, Urhan, 1987, Yu et al., 2003). However, generally, the increase of EPA replacement ratio led to substantial drop of compressive strength, as Figure 2-7 shows, around 60% reductions were achieved by comparing the strength of P100 and P0 in the 3rd, 7th and 28th day.

This overall reduction trend is probably caused by the weak porous microstructure of EPA (Demirboğa et al., 2001), thus the interfacial transition zone (ITZ) is weakened by the addition of EPA, and the porous EPA also increases the porosity of the concrete dramatically, as seen from the density drop, to decrease the strength. In all, the strength decreasing effects must be stronger than the pozzolanic effect of EPA to reach the general increasing trend.

Figure 2-8 gives a good power relationship with the coefficient of determination ($R^2=0.97$) between the 28th day compressive strength and the oven-dry density. It demonstrates that the compressive strength would reduce with the decreasing densities. Similar relationships were also mentioned by other researchers (Albayrak et al., 2007, Türkmen and Kantarcı, 2007, Zhang and Gjvorv, 1991).

2.3.3 Splitting tensile strength

Splitting tensile strength (STS) is considered to be a more trustworthy index than beam flexural strength for the tensile strength of concrete (Thomas and Ries, 2006). Thus, it was chosen in this study to evaluate the tensile properties of those mixes. Figure 2-9 and Table 2-2 report the results of STS tests in all mixes. Basically, the STS showed a very similar trend like the UCS with respect to the increasing EPA replacement ratio. In general, STS dropped with the addition of EPA. Correspondingly, the STS of P50 was also larger than that of P25 due to the possible pozzolanic effect of EPA described previously in Section 2.3.2. In Figure

2-10, the scatters of all the mixes at all ages were plotted together. We noted the power relationship between the 28th day UCS and STS, in Equation (2.1), and the overall power relationship between the UCS and STS at all ages in Equation (2.2). The Equation (2.3) recommended by ACI 363R-92 (ACI, 1992) was also curved as the comparison of the obtained fittings.

$$f_{STS} = 0.36(f_c)^{0.66} ; R^2 = 0.97 \quad (2.1)$$

$$f_{STS} = 0.28(f_c)^{0.72} ; R^2 = 0.91 \quad (2.2)$$

$$f_{STS} = 0.59(f_c)^{0.5} ; 21 \text{ MPa} < f_c < 83 \text{ MPa} \quad (2.3) \text{ (ACI, 1992)}$$

where f_c is unconfined compressive strength (MPa), f_{STS} is splitting tensile strength (MPa), R^2 is the coefficient of determination.

As shown in Figure 2-10, Equation (2.1) showed an excellent power regression line for scatters in the 28th day, and scatters at earlier ages conformed to a similar but not identical curve plotted by Equation (2.1); this indicated that the UCS and STS strength gain rates were performing similarly but not the same with curing time. Generally, Equation (2.2) can still well describe the relationships between UCS and STS of all the scatters, though with a little less reliable R^2 of 0.91. As seen in the curve of Equation (2.3), the test results could roughly be in the range of $\pm 10\%$ of Equation (2.3), as suggested by ACI 363R-92 (ACI, 1992); However, the Equation (2.2) with a real number of 0.72 gave better accuracy than Equation

(2.3) with a real number of 0.5. This agreed with previous findings (Gardner and Poon, 1976, Oluokun et al., 1991).

2.3.4 Direct tensile bond strength

As shown in Figure 2-11, the direct tensile loading can lead to two categories of failures, namely, the bond interface failure and non-bond interface failure. For example, as seen in Figure 2-11(a) and (b), these two belong to the bond interface failure, that occurs in the interface between the rock and the concrete. And in Figure 2-11(c) and (d), failures happen in either the rock part or the concrete part. Therefore, two charts in Figure 2-12 were made to summarize the direct tensile testing results of all samples for sandstone, limestone and granite after applying P0, P25, P50, P75 and P100, respectively. From Figure 2-12(a) and (b), we can notice that all sandstone-concrete samples failed at the sandstone parts, at an average of about 1.2 MPa. The obtained strength for sandstone here is also consistent with the pure tension test results for bond strength of sandstone with shotcrete (Hahn and Holmgren, 1979). In other words, this confirms us the fact that the bond strength between sandstone and concrete containing EPA is larger than the direct tensile strength of sandstone itself. And we can find the fact that the bond interface failures only occurred at samples of limestone and granite applying P0, P25 and P50. Since P75 and P100 parts would have failures themselves at about 1.8 MPa and 1.25 MPa, separately. As for the influence of

EPA additions on rock-shotcrete interface bond strength, no apparent trend can be observed in either the limestone or granite groups. From one hand, the additions of EPA can somehow increase the bond strength in granite group; from another hand, adverse effects were also noticed in the limestone group. Nevertheless, one certain finding is that the bond strength of concrete after additions of EPA would still maintain at a substantial level, which is higher than the direct tensile strength of sandstone (about 1.2 MPa). And because all the surfaces of rocks were prepared by the diamond saw, resulting in a relatively smooth surface, the bond strength can be expected even larger values under rough surfaces which give more contact areas (Austin et al., 1995).

2.3.5 Thermal conductivity and influence of moisture

The thermal conductivity results measured by TPS 1500 in air-dry (48 hours natural drying in 21°C room air,) and oven-dry (48 hours oven-drying in 110° ± 5°C oven) (ASTM, 2004b) conditions are listed in Figure 2-13(a) and Table 2-2. The air-dry thermal conductivity was in the range of 2.516 to 0.685 W/(m·K), and the oven-dry thermal conductivity from 1.831 to 0.379 in all the five mixes. It was found that the thermal conductivity decreased dramatically with the increased amount of EPA. The reason for the thermal conductivity decrease may be attributed to the porous structure of EPA and the low thermal conductivity (0.04 W/(m·K)) of EPA itself (Khan, 2002, Topçu and Işıkdağ, 2007). Figure 2-14

displays the percentage of reductions with respect to the controlling mix P0; for example, in oven-dry conditions, around 60% thermal conductivity reduction can be observed with 75% EPA replacement and about 80% thermal conductivity reduction was achieved by 100% EPA replacement. Thermal conductivity indicates the ability of the material to conduct heat. According to Fourier's law of conduction, the heat flux (W/m^2) is proportional with the thermal conductivity ($W/(m\cdot K)$) in a determined temperature gradient (K/m). In other words, in a determined temperature gradient condition, the heat flux can be reduced 60% and 80% by using P75 and P100, respectively. The upper limit of the working climate wet-bulb temperature in underground mines is $27^\circ C$ (Hall et al., 1984), and the virgin rock temperature which though increases with the depth underneath the earth, can be assumed to be constant at a certain mining level, thus the temperature gradient is reasonably constant at the ideally simplified situation. Therefore, the thermal conductivity becomes the key factor for geothermal heat flux control by insulation method. Figure 2-15 reveals a strong linear relationship between the moisture content and the thermal conductivity, by comparing the thermal conductivity between oven-dry and air-dry samples. The increasing moisture content absolutely increases the thermal conductivity values, because the thermal conductivity of dry air ($0.026 W/(m\cdot K)$) is far more less than that of water ($0.6 W/(m\cdot K)$) at $20^\circ C$ (Sukhatme, 2011b). When the free water and physically

bound water were removed by oven-drying, the low thermal conductivity air replaced the water in the vacancies of the concrete pores; this eventually resulted in the drop of thermal conductivity in oven-dry conditions. As seen in Figure 2-16, the thermal conductivity is strongly related with the oven-dry density in the power law with a reliable R^2 of 0.998. It indicates that the samples with lower oven-dry density would have lower thermal conductivity. These two advantages enhanced the feasibility of using this material for mine insulation.

2.3.6 Heat capacity

The TPS 1500 can not only obtain the results of thermal conductivity, but also the values of thermal diffusivity and heat capacity. The relationships between the three parameters are defined as follows:

$$\alpha = \frac{k}{\rho C_p} \quad (2.4)$$

where α is the thermal diffusivity (m^2/s), k is the thermal conductivity ($\text{W}/(\text{m}\cdot\text{K})$), ρ density (kg/m^3), C_p specific heat capacity ($\text{J}/(\text{kg}\cdot\text{K})$), the denominator of Equation (2.4), ρC_p , is called volumetric heat capacity ($\text{J}/(\text{m}^3\cdot\text{K})$).

The results of thermal diffusivity and volumetric heat capacity are listed in Table 2-2. Figure 2-13(b) and (c) plot the values of thermal diffusivity and volumetric heat capacity in both air-dry and oven-dry conditions. Figure 2-13(d) transforms the volumetric heat capacity into specific heat capacity by dividing the corresponded density. Basically, the specific heat capacity showed an increasing

trend, with the exception of P50 and P75, namely, the specific heat capacity of P75 was smaller than that of P50. The increasing trend is primarily caused by the substantially increased mass proportion of water in mix design, since the specific heat capacity of bound water, 2200 J/ (kg·K) (Bentz et al., 2011, Waller et al., 1996), is far more larger than other components in the mixes as shown in Table 2-1. However, the fluctuations of these curves in Figure 2-13(b) and (c) proved that other components rather than water were also affecting the overall specific heat capacity. In order to clarify the effects of the mix components on specific heat capacity, one previous prediction model (Bentz, 2007, Bentz et al., 2011, Choktaweeakarna et al., 2009) in Equation (2.5) was introduced and modified to compare the tested results of specific heat capacity:

$$C_p^{mo} = C_p^{fw} R_m^{fw} + C_p^{bw} R_m^{bw} + C_p^c R_m^c + C_p^s R_m^s + C_p^E R_m^E \quad (2.5)$$

where C_p is the specific heat capacity (J/(kg·K)), R_m is the mass ratio of ingredients (%), the subscripts of mo , fw , bw , c , s , E are mortar, free water, bound water, cement, sand and EPA, individually. The values of the specific heat capacity of free water, bound water, cement, sand and EPA in the calculation were 4180, 2200, 740, 710, 837 J/(kg·K), respectively (Bentz et al., 2011, Karakoc and Demirboga, 2010, Zähringer et al., 2001). The predicted results by the model were compared with the tested results of specific heat capacity in Figure 2-17. It has

proved that Equation (2.5) could still roughly predict the tested results, and the accuracy was still in the promising range.

2.3.7 Thermal diffusivity

The thermal diffusivity indicates the ability of the material to adjust its temperature to that of the surroundings. For underground mines, higher thermal diffusivity means quicker adjustment for liners to reach the virgin rock temperature. For the mining insulation application, lower thermal diffusivity is preferred to minimize the early heat flux which peaks in the first few days after excavation. Initially, it is a transient heat conduction process, thermal diffusivity is very critical for the heat flux in early stages, as shown in Equation (2.6), which is the basic equation for general three-dimensional transient heat conduction in rectangular coordinate system. Assuming the material is isotropic, stationary, its thermal conductivity doesn't depend on temperature. However, after enough long time, the conduction may be simplified as the quasi-steady/steady state, as shown in Equation (2.7), then thermal conductivity, is the most important parameter of insulation material to control the heat flux. The equations (Sukhatme, 2011a) are displayed as follows:

$$\frac{\partial^2 T}{\partial x^2} + \frac{\partial^2 T}{\partial y^2} + \frac{\partial^2 T}{\partial z^2} + \frac{q'''}{k} = \frac{1}{\alpha} \frac{\partial T}{\partial t} \quad (2.6)$$

$$\frac{\partial^2 T}{\partial x^2} + \frac{\partial^2 T}{\partial y^2} + \frac{\partial^2 T}{\partial z^2} + \frac{q'''}{k} = 0 \quad (2.7)$$

where $T(x, y, z, t)$ is the temperature (K) in location (x, y, z) at time t (s), k is the thermal conductivity (W/(m·K)), q''' is the volumetric heat generation rate (W/m³), α the thermal diffusivity (m²/s).

As Figure 2-13(c) demonstrates, the thermal diffusivity deteriorated with the increased volume portion of EPA. It is easy to understand this drop, by comparing Figure 2-13(a) and (b) and noting Equation (2.4), the decreasing thermal conductivity divided by the increasing volumetric heat capacity gave the deteriorating trend of thermal diffusivity. The reduction percentiles of thermal diffusivity in different EPA proportions with respect to the P0 (controlling mix) were scattered in Figure 2-14, the air-dry thermal diffusivity reductions were approximately from 25% to 75% in P25 to P100 mixes, respectively, and that of the oven-dry samples were in the range of 5% to 65%, individually. This indicated that the samples, with certain amounts of moisture could probably expect more thermal diffusivity drop than that of oven-dry samples, as the EPA added. This conclusion could be very practical when it applies to the humid underground environment. Figure 2-16 also displays the non-linear power curve fitting between the oven-dry density and oven-dry thermal diffusivity by viewing the right Y-axis. Though not as good as the regression curve of thermal conductivity, it was still in good shape with the R^2 of 0.90. These obtained equations could be useful to supply with predictions for further studies.

2.4 Conclusions

According to the study, we can draw the following conclusions:

1. The density of the mixes is reduced dramatically by adding the EPA volume proportions.
2. Unconfined compressive strength (UCS) and splitting tensile strength (STS) generally decreased with increasing EPA replacement ratio, and the pozzolanic effect of EPA in P50 mix was obvious at early ages. All the mixes, even the P100 mix, could still maintain relatively good mechanical properties. As seen, 20% to 60% UCS loss at the 28th day was observed from the P25 to the P100 mix, and this gave a good point of the structural use in underground mines.
3. Substantial direct tensile bond strength between various rocks and concrete from P0 to P100 were obtained to ensure further applications on rock surface.
4. Dramatic thermal conductivity reductions were achieved by the use of EPA. As seen, 22% to 80% thermal conductivity losses were noticed from the P25 to the P100 mix, and the loss ratio of thermal conductivity appeared more than that of UCS and STS.
5. Strong power relationships were found in oven-dry density versus UCS, STS versus UCS, and oven-dry density versus oven-dry thermal conductivity, and

oven-dry density versus oven-dry thermal diffusivity. An excellent linear relationship was found in moisture versus thermal conductivity reduction.

6. One previous model was modified and compared with the tested results of specific heat capacity, namely, specific heat capacity of hardened concrete is approximately the weighted mean value of individual specific heat capacity of ingredient with respect to its corresponded mass ratio; And acceptable match was found between the model predicted results and tested results.

Tables in Chapter 2

Table 2-1 Mix proportions of experimental concrete

Mix number	P0	P25	P50	P75	P100
Replacement percentage (%)	0	25	50	75	100
Cement (kg/m ³)	519.5	519.5	519.5	519.5	519.5
w/cm	0.45	0.45	0.45	0.45	0.45
Water(kg/m ³)	233.8	233.8	233.8	233.8	233.8
Sand (kg/m ³)(Oven-dry)	1623.5	1217.6	811.7	405.9	0.0
EPA (kg/m ³)(Oven-dry)	0.0	17.3	34.6	52.0	69.3

Table 2-2 Testing results of all five mixes

EPA replacement percentage (%)	0	25	50	75	100
Fresh concrete density(kg/m ³)	2192.7	2101.2	1929.7	1698.0	1397.8
Hardened density(kg/m ³)	2303.0	2151.5	1989.9	1757.6	1444.4
Oven-dry density(kg/m ³)	2139.2	1974.6	1844.8	1525.3	1169.1
1st day UCS(MPa)	12.32	11.35	11.80	10.98	7.71
3rd day UCS(MPa)	27.31	22.19	22.41	16.40	11.50
7th day UCS(MPa)	33.86	27.95	28.56	22.08	13.50
28th day UCS(MPa)	43.78	40.70	32.96	22.64	16.87
1st day STS(MPa)	1.46	1.28	1.49	1.46	1.32
3rd day STS(MPa)	2.86	2.14	2.85	2.28	2.07
7th day STS(MPa)	3.15	2.92	3.18	2.35	2.24
28th day STS(MPa)	4.33	4.08	3.87	2.73	2.32
Air-dry samples moisture content (%)	7.58	8.87	12.18	17.86	27.96
Air-dry(48hrs) thermal conductivity(W/(m·K))	2.5164	2.0696	1.7532	1.1565	0.6852
Air-dry(48hrs) thermal diffusivity(mm ² /s)	1.1562	0.8487	0.5587	0.4701	0.2682
Air-dry(48hrs) volumetric heat capacity(MJ/(m ³ ·K))	2.1764	2.4385	3.1378	2.4602	2.5544
Oven-dry(48hrs) thermal conductivity(W/(m·K))	1.8313	1.4450	1.1830	0.7351	0.3799
Oven-dry(48hrs) thermal diffusivity(mm ² /s)	0.9977	0.9363	0.6584	0.6141	0.3438
Oven-dry(48hrs) volumetric heat capacity(MJ/(m ³ ·K))	1.8354	1.5433	1.7968	1.1972	1.1050

Figures in Chapter 2



Figure 2-1 The EPA used in the study

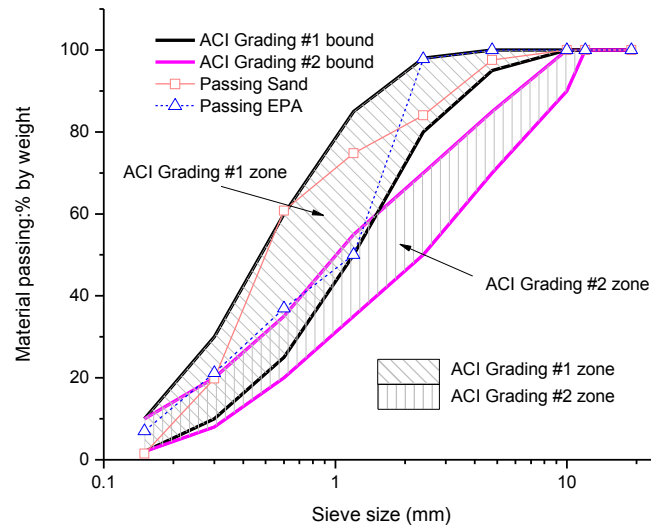
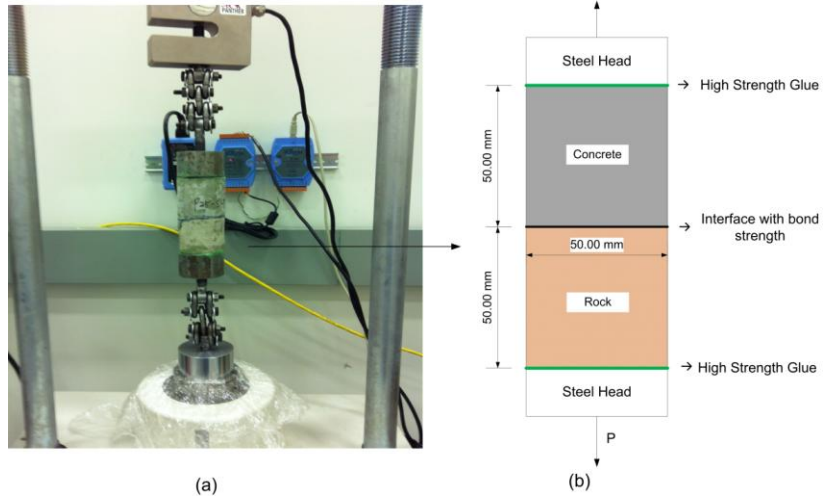
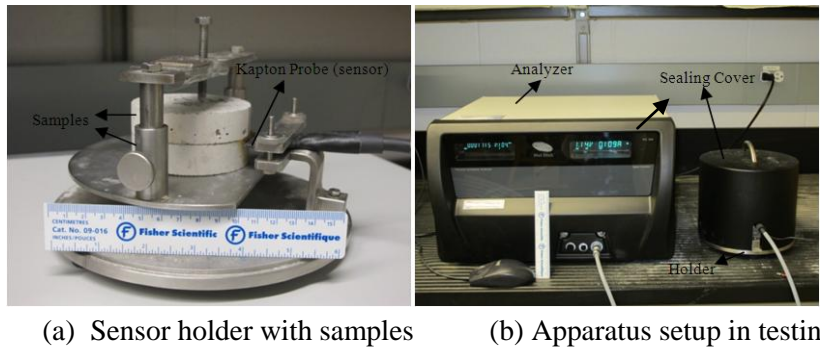


Figure 2-2 Aggregate size sieve analysis



(a) Testing frame with sample (b) Schematic of sample

Figure 2-3 The setup of direct tensile bond strength



(a) Sensor holder with samples (b) Apparatus setup in testing

Figure 2-4 The setup of TPS 1500

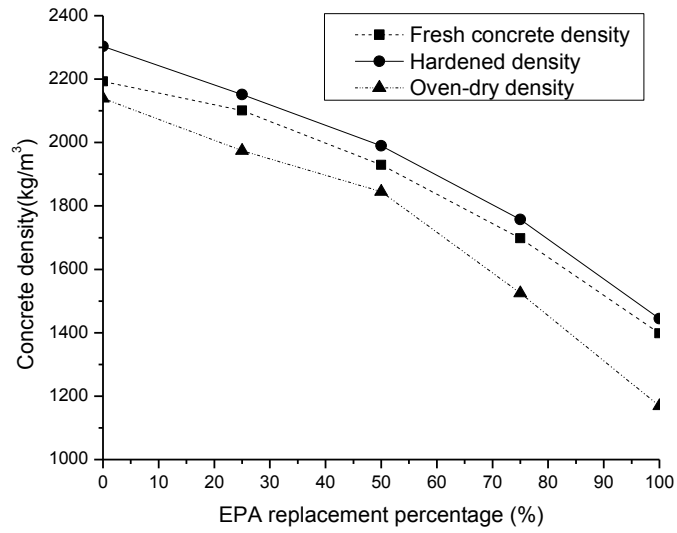


Figure 2-5 Relationship between EPA replacement percentage and concrete density

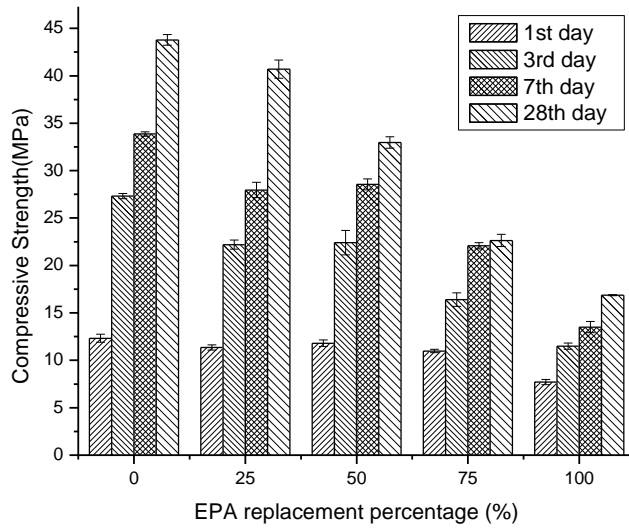


Figure 2-6 Relationship between EPA replacement percentage and UCS

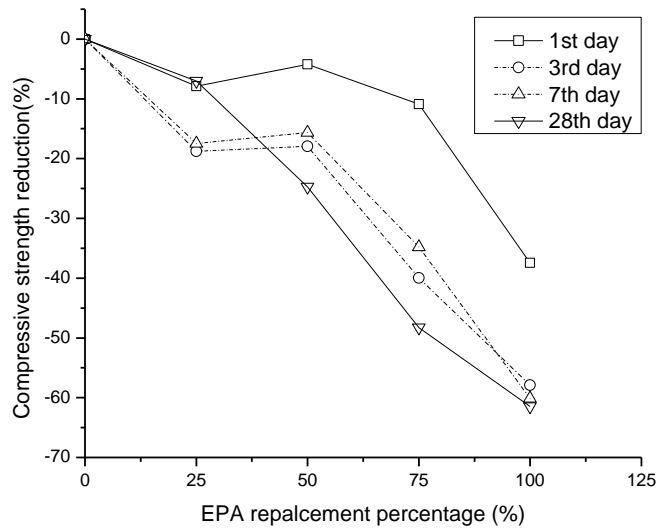


Figure 2-7 UCS reduction with respect to P0 (Controlling mix)

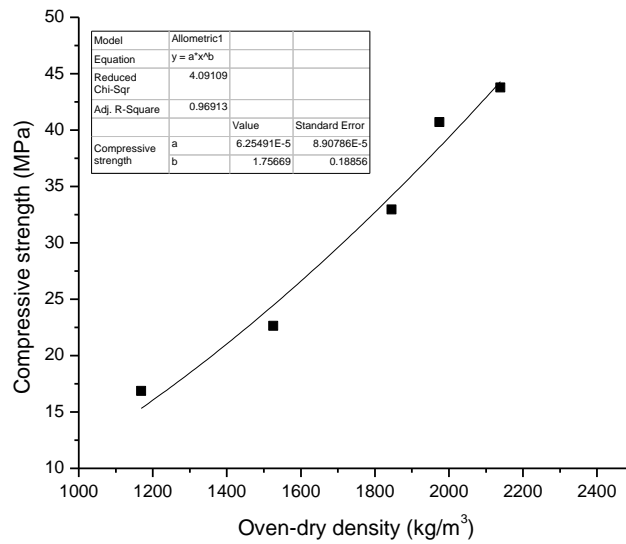


Figure 2-8 Correlation between 28-day compressive strength and oven-dry density

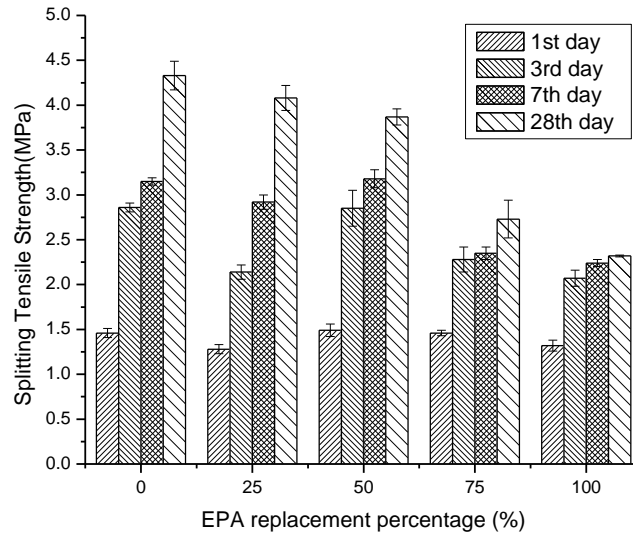


Figure 2-9 Relationship between EPA replacement percentage and splitting tensile strength

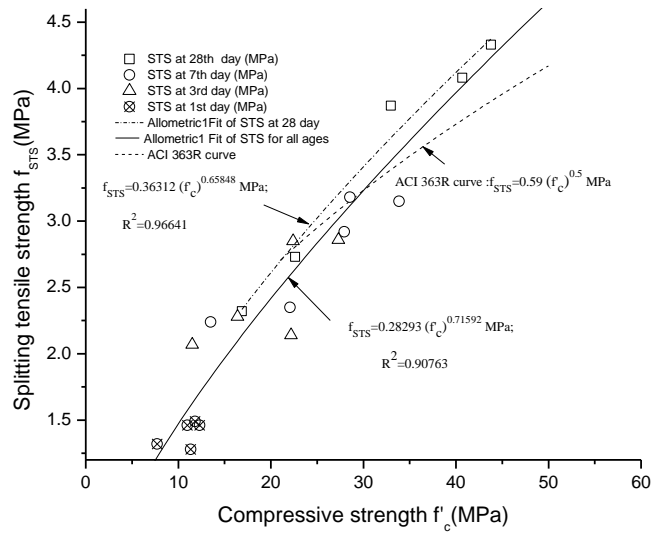
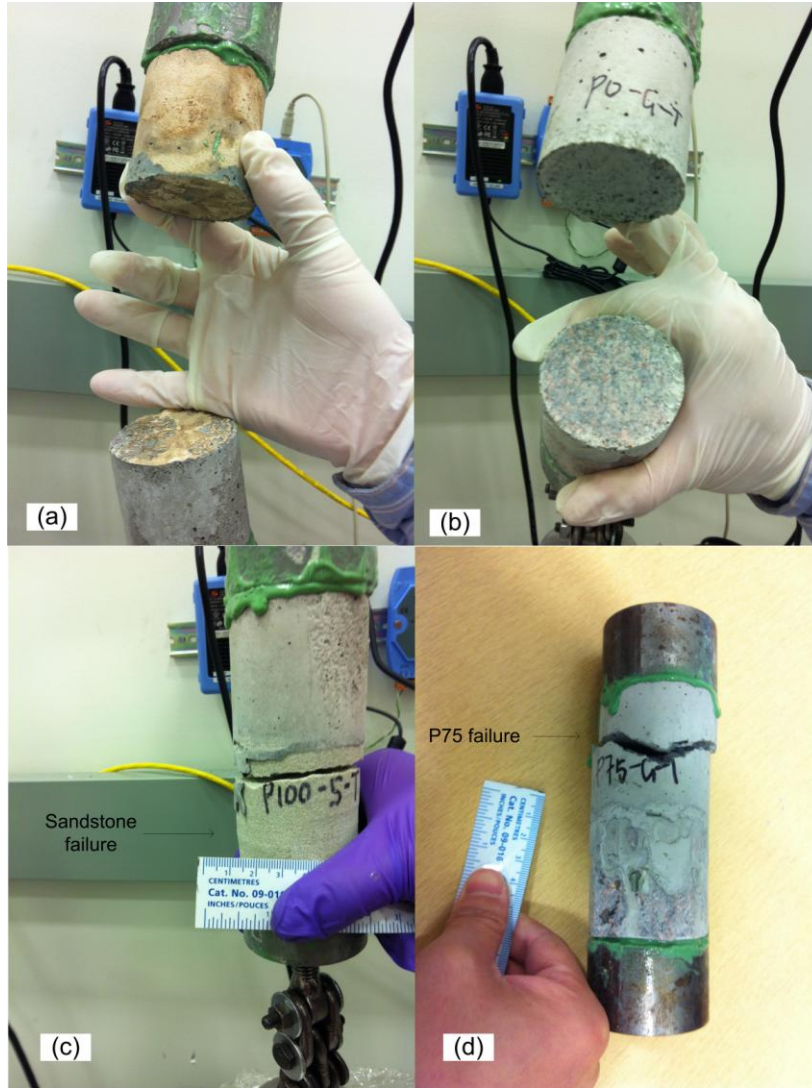


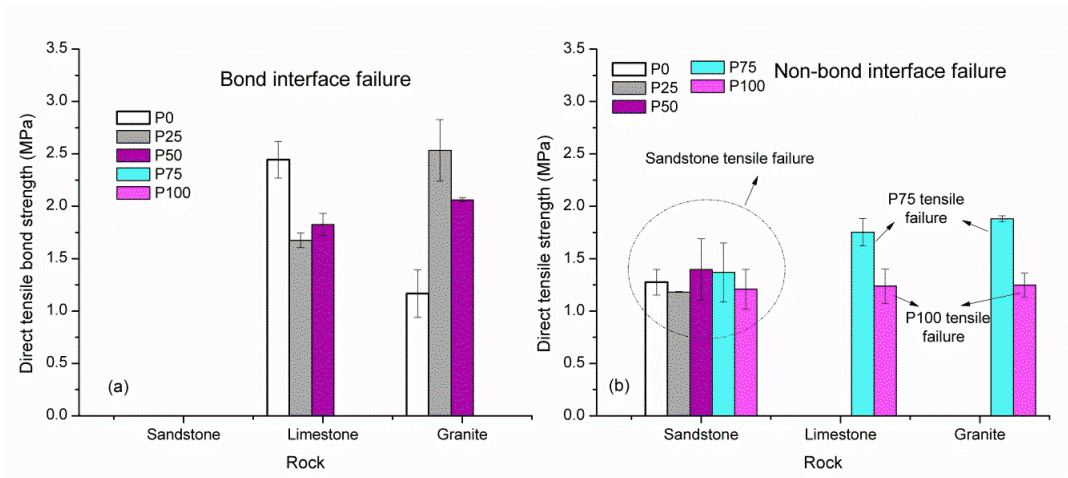
Figure 2-10 Relationship between UCS and STS



(a) Failure at limestone interface (b) Failure at granite interface

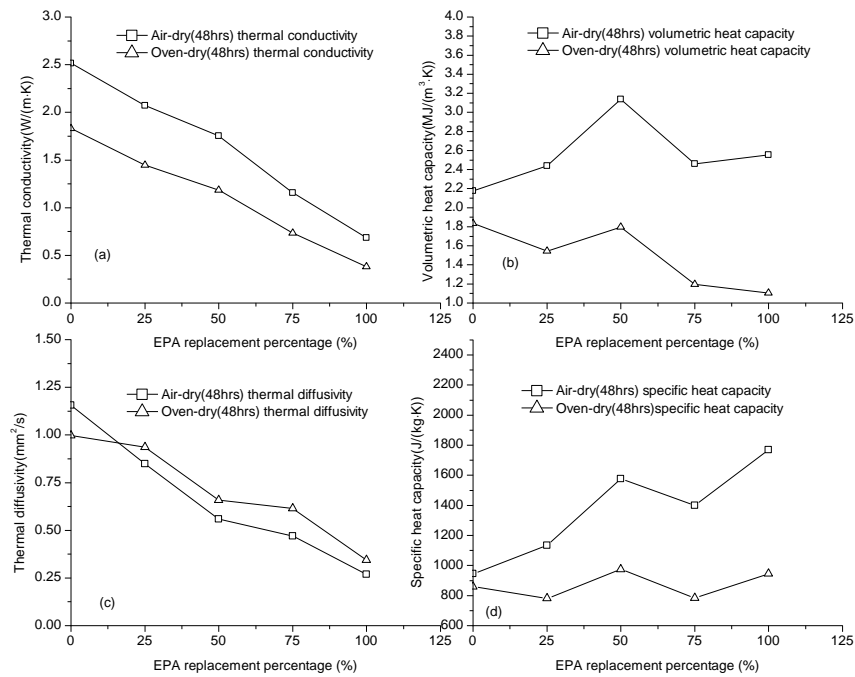
(c) Failure at sandstone (d) Failure at P75

Figure 2-11 Direct tensile testing photos at different failure locations



(a) Results of bond interface failure (b) Results of non-bond interface failure

Figure 2-12 Direct tensile testing result



(a) Thermal conductivity (b) Volumetric heat capacity
(c) Thermal diffusivity (d) Specific heat capacity

Figure 2-13 Relationship between EPA replacement percentage and thermal properties

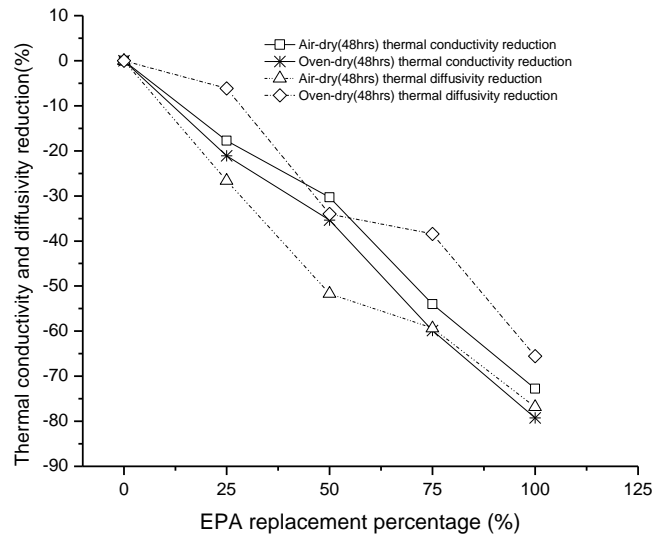


Figure 2-14 Thermal conductivity and diffusivity reduction with respect to P0

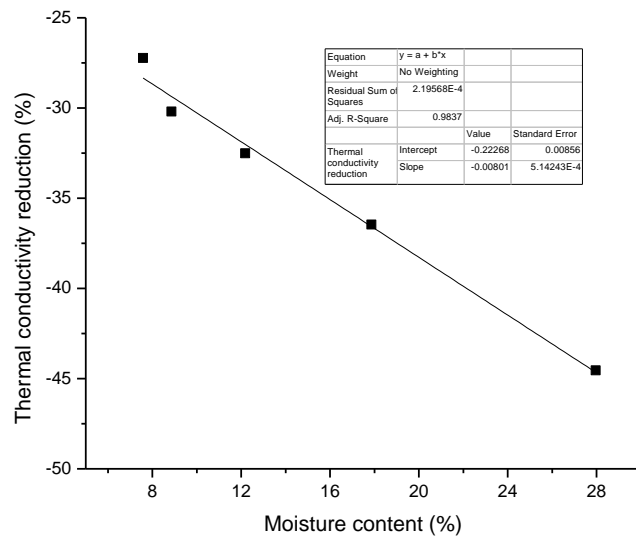


Figure 2-15 Relationship between moisture content and oven-dry conductivity (48hrs) reduction with respect to air-dry (48hrs) conductivity

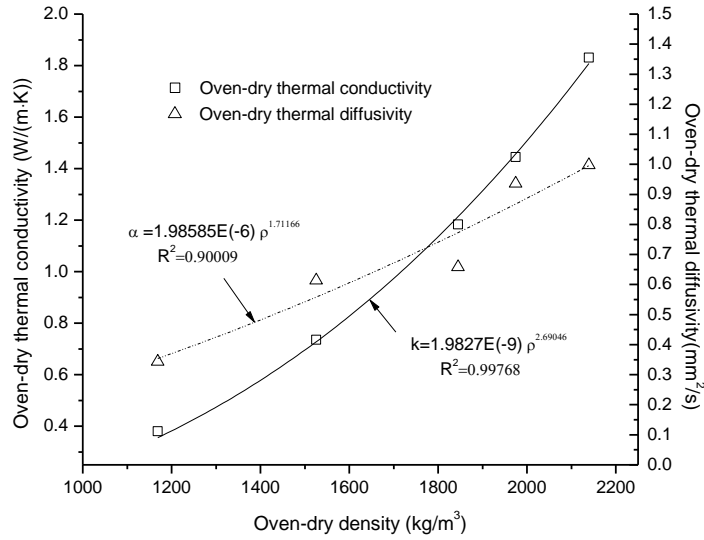


Figure 2-16 Relationship between oven-dry conductivity, oven-dry diffusivity and oven-dry density

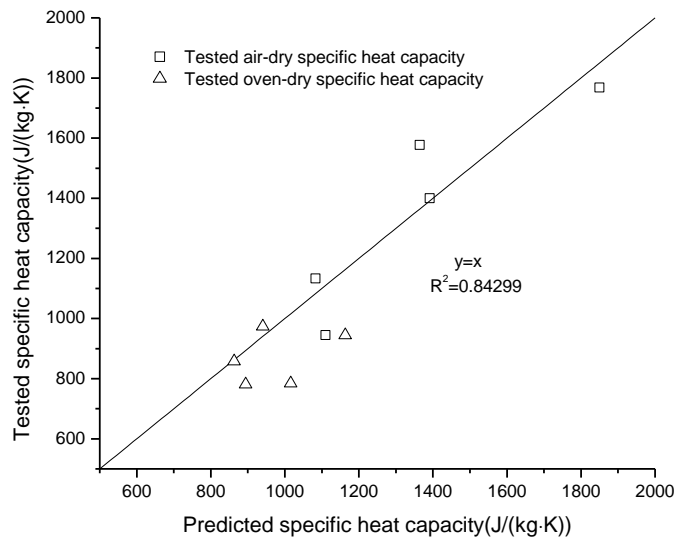


Figure 2-17 Relationship between predicted specific heat capacity and tested specific heat capacity

References

- ACI (1992) State-of-the-Art report on high-strength concrete (ACI-363R). Farmington Hills, MI, American Concrete Institute.
- ACI (2005) Guide to shotcrete (506R-05). Farmington Hills, MI, American Concrete Institute.
- ACI (2009) Guide for specifying underground shotcrete (506.5R-09). Farmington Hills, MI, American Concrete Institute.
- ADMMR (2004) Resolution Copper takes over. *Arizona Mineral Resource Newsletter*. West Washington, Arizona Department of Mines & Mineral Resource.
- Albayrak, M., Yörükoglu, A., Karahan, S., Atllhan, S., Yilmaz Aruntas, H. & Girgin, I. (2007) Influence of zeolite additive on properties of autoclaved aerated concrete. *Building and Environment*, 42, 3161-3165.
- ASTM (2004a) Standard test method for splitting tensile strength of cylindrical concrete specimens (ASTM C496/C 496M-04). West Conshohocken, Pennsylvania, ASTM International.
- ASTM (2004b) Standard test method for total evaporable moisture content of aggregate by drying (ASTM C556). West Conshohocken, Pennsylvania, ASTM International.
- ASTM (2007) Standard practice for making and curing concrete test specimens in the laboratory (ASTM C192/C 192M-07). West Conshohocken, Pennsylvania, ASTM International.
- ASTM (2008) Standard test method for direct tensile strength of intact rock core specimens (ASTM D2936). West Conshohocken, Pennsylvania, ASTM International.
- ASTM (2009a) Standard specification for lightweight aggregates for insulating concrete (ASTM 332). West Conshohocken, Pennsylvania, ASTM International.
- ASTM (2009b) Test method for compressive strength of cylindrical concrete specimens (ASTM C39/C39M-09a). West Conshohocken, Pennsylvania, ASTM International.
- Austin, S., Robins, P. & Pan, Y. (1995) Tensile bond testing of concrete repairs. *Materials and Structures*, 28, 249-259.
- Austin, S., Robins, P. & Pan, Y. (1999) Shear bond testing of concrete repairs. *Cement and Concrete Research*, 29, 1067-1076.
- Bentz, D. P. (2007) Transient plane source measurements of the thermal properties of hydrating cement pastes. *Materials and Structures*, 40, 1073-1080.

- Bentz, D. P., Peltz, M. A., Durán-Herrera, A., Valdez, P. & Juárez, C. A. (2011) Thermal properties of high-volume fly ash mortars and concretes. *Journal of Building Physics*, 34, 263-275.
- Bottomley, P. (1985) The reduction in heat flow due to the insulation of rock surfaces in mine airways. *2nd US Mine Ventilation Symposium*. Reno, NV.
- Bottomley, P. & van Rensburg, B. (1987) The insulation of rock surfaces-an empirical study. *Journal of the Mine Ventilation Society of South Africa*, 40, 41-45.
- Chellam, S. (1992) Thermal insulation of underground mine workings at deep levels. *Department of Mining Engineering*. Rapid City, South Dakota, South Dakota School of Mines and Technology.
- Choktaweekarna, P., Saengsoy, W. & Tangtermsirikul, S. (2009) A model for predicting the specific heat capacity of fly-ash concrete. *ScienceAsia*, 35, 178-182.
- Ciullo, P. A. (1996) The industrial minerals. *Industrial minerals and their uses: a handbook and formulary*. Westwood, New Jersey, Noyes Publication.
- CSA (2009) *CAN/CSA A23.1/A23.2: Concrete Materials and Methods of Concrete Construction/Methods of Tests and Standard Practices for Concrete*, Mississauga, Ontario, Canada, Canadian Standard Association.
- Demirboğa, R., Örüng, I. & Gül, R. (2001) Effects of expanded perlite aggregate and mineral admixtures on the compressive strength of low-density concretes. *Cement and Concrete Research*, 31, 1627-1632.
- Enkvist, P., Nauclic, T. & Rosander, J. (2007) A cost curve for greenhouse gas reduction. *McKinsey Quarterly*, 1, 34.
- Erdem, T. K., Meral, Ç., Tokyay, M. & Erdogan, T. Y. (2007) Use of perlite as a pozzolanic addition in producing blended cements. *Cement and Concrete Composites*, 29, 13-21.
- Fridleifsson, I. B., Bertani, R., Huenges, E., Lund, J. W., Ragnarsson, A. & Rybach, L. (2008) The possible role and contribution of geothermal energy to the mitigation of climate change. *IPCC Scoping Meeting on Renewable Energy Sources*. Luebeck, Germany.
- Gardner, N. J. & Poon, S. M. (1976) Time and temperature effects on tensile, bond, and compressive strengths. *Journal of the American Concrete Institute*, 73, 405-409.
- Gustafsson, S. E. (1967) A non-steady-state method of measuring the thermal conductivity of transparent liquids. *Zeitschrift Naturforschung Teil A*, 22, 1005.

- Gustafsson, S. E. (1990) Transient plane source techniques for thermal conductivity and thermal diffusivity measurements of solid materials. *Review of Scientific Instruments*, 62, 797-804.
- Hahn, T. & Holmgren, J. (1979) Adhesion of shotcrete to various types of rock surfaces. *4th International Congress on Rock Mechanics*. Montreux, Switzerland, A. A. Balkema.
- Hall, A. E., Mathews, K. E. & Gangal, M. K. (1984) Ventilation and refrigeration requirements and costs in deep Canadian mines. Ottawa, Ontario, Canada Centre for Mineral and Energy Technology, Mining Research Laboratories.
- He, Y. (2005) Rapid thermal conductivity measurement with a hot disk sensor: Part 1. Theoretical considerations. *Thermochimica Acta*, 436, 122-129.
- Howarth, D. F. & Gillies, A. D. S. (1987) An examination of insulation used on mine refrigeration chilled water pipes. *Geotechnical and Geological Engineering*, 5, 83-91.
- ISO (2008) Plastics — Determination of thermal conductivity and thermal diffusivity —Part 2:Transient plane heat source (hot disc) method. Geneva, Switzerland, International Organization for Standardization.
- Karakoc, M. B. & Demirboga, R. (2010) HSC with expanded perlite aggregate at wet and dry curing conditions. *Journal of Materials in Civil Engineering*, 22, 1252-1259.
- Khan, M. I. (2002) Factors affecting the thermal properties of concrete and applicability of its prediction models. *Building and Environment*, 37, 607-614.
- Kramar, D. & Bindiganavile, V. (2010) Mechanical properties and size effects in lightweight mortars containing expanded perlite aggregate. *Materials and Structures*, 44, 735-748.
- Oluokun, F. A., Burdette, E. G. & Deatherage, J. H. (1991) Splitting tensile strength and compressive strength relationships at early ages. *ACI Materials Journal*, 88, 115-121.
- Pickering, A. J. & Tuck, M. (1997) Heat: sources, evaluation, determination of heat stress and heat stress treatment. *Mining Technology*, 79, 147-56.
- Rawlins, C. A. & Phillips, H. R. (2001) Reduction of mine heat loads. *7th International Mine Ventilation Congress*. Krakow, Poland.
- Sukhatme, S. P. (2011a) Heat conduction concepts, thermal resistance, and the overall heat transfer coefficient. *A Text Book on Heat Transfer*. Cambridge, Massachusetts, Phlogiston Press.
- Sukhatme, S. P. (2011b) Some thermophysical properties of selected materials. *A Text Book on Heat Transfer*. Cambridge, Massachusetts, Phlogiston Press.

- Thomas, A. H. & Ries, J. P. (2006) Lightweight concrete and aggregate. IN Lamond, J. F. & Pielert, J. H. (Eds.) *Significance of tests and properties of concrete and concrete-making materials*. West Conshohocken, ASTM International.
- Topçu, İ. B. & Işıkdag, B. (2007) Manufacture of high heat conductivity resistant clay bricks containing perlite. *Building and Environment*, 42, 3540-3546.
- Türkmen, İ. & Kantarcı, A. (2007) Effects of expanded perlite aggregate and different curing conditions on the physical and mechanical properties of self-compacting concrete. *Building and Environment*, 42, 2378-2383.
- Urhan, S. (1987) Alkali silica and pozzolanic reactions in concrete. Part 1: Interpretation of published results and an hypothesis concerning the mechanism. *Cement and Concrete Research*, 17, 141-152.
- USBM (1994) An 'insulating' shotcrete for heat abatement in deep mines. *Technology News* 434.
- Waller, V., De Larrard, F. & Roussel, P. (1996) Modelling the temperature rise in massive HPC structures. *4th International Symposium on Utilization of High-Strength/High-Performance Concrete*. Paris, France, RILEM.
- Yu, L. H., Ou, H. & Lee, L. L. (2003) Investigation on pozzolanic effect of perlite powder in concrete. *Cement and Concrete Research*, 33, 73-76.
- Zähringer, K., Martin, J. P. & Petit, J. P. (2001) Numerical simulation of bubble growth in expanding perlite. *Journal of Materials Science*, 36, 2691-2705.
- Zhang, M. H. & Gjvorv, O. E. (1991) Mechanical properties of high-strength lightweight concrete. *ACI Materials Journal*, 88, 240-247.

Chapter 3 Thermal properties of lightweight dry-mix shotcrete containing expanded perlite²

3.1 Introduction

Shotcrete, also termed as sprayed concrete, refers to a cement-based mixture that is projected pneumatically at high velocity towards the target surface (Warner, 1995). Further, it is stipulated that it must be compacted by its own momentum (Yoggy, 2000). This technique has been widely used on many different construction applications in civil engineering, such as repair of structures, corrosion protection, swimming pool, fire protection coatings, and thin shell dome, as well as in mines where it is used most commonly as tunnel liners (Banthia et al., 1994, Beaupré 1994, Leung et al., 2005, Morgan et al., 1998). The mining industry has now become a major consumer of shotcrete especially for use in underground rock support (Hoek and Brown, 1990), so much so that the annual consumption of shotcrete in North America is estimated to be over 200,000 m³ (Rispin and Brooks, 2001).

There are two methods of producing shotcrete namely; the dry-mix and the wet-mix processes, and both of them are routinely used in tunnels and mines. Specifically,

² The content of this Chapter has been prepared and submitted as a journal manuscript: Liu, W. V., Apel, D. B. & Bindiganavile, V. S. (2012) Thermal properties of lightweight dry-mix shotcrete containing expanded perlite. *Indian Concrete Journal* (submitted)

the dry-mix process is the one wherein the dry ingredients, including cement, aggregates, and any admixture (but as a powder) are pneumatically conveyed from the spraying equipment through the delivery hose to the spraying nozzle, at which point a water ring introduces the water under pressure from another hose. The water mixes with the dry ingredients inside the nozzle and the fresh mix is then projected to the target at high velocity. Because of this distinctive production process, shotcrete differs from the conventional cast concrete in rheology and hardened properties (Leung et al., 2005) (Banthia et al., 1994). However, barring a single report from the USBM (USBM, 1994), no research has yet been undertaken to characterize its thermal properties, especially as resulting from lightweight inclusions.

As the demand for minerals increases the world over, the depth of mining also increases considerably and working deep in the belly of the earth becomes a necessity. The working face has to contend with higher and higher temperatures due to the geothermal heat trapped in the surrounding rocks. Therefore, to make the tunnels and shafts safe as well as comfortable for the miner, the demand on ventilation and cooling systems is rising (Hartman et al., 1998). This in turn leads to an escalating operation cost and therefore to the cost of the mineral itself. It is here that the application of an insulation which is also mechanically sound takes importance (Bottomley, 1985, Bottomley and van Rensburg, 1987, Chellam,

1992). Shotcrete has been extensively used as a support to tunnels and its mechanical performance including resistance to rock burst has been widely documented (Hoek and Brown, 1990, Kaiser and Tannant, 2001, Yi, 1996). Attention is now focused on its thermal characteristics to explore its dual role as an insulating liner.

In this study, expanded perlite aggregate (EPA) was incorporated as a lightweight substitute for sand. Raw perlite occurs in nature as a siliceous volcanic rock, which contains 2-5% water (Kramar and Bindiganavile, 2010). After heating at over 870°C, this water vaporizes and causes the volume expanding from 4 to 20 times (Ciullo, 1996) and thereby form the lightweight porous expanded perlite. It is well known that expanded perlite can be blended with normal aggregates in suitable proportions to achieve a variety of benefits including lightweight, superior thermal resistance, acoustic insulation and shrinkage resistance in conventional cement-based systems (Brouk, 1949). The material has been applied in tiles, stucco, brick, block/masonry, precast products, roof fill, pipe coating, oil-gas and geothermal wells, *etc.* (Anon, 1961, Gallus et al., 1979, Pirogov et al., 1972, Probert and Giani, 1976, Reichard, 1971, Singh and Garg, 1991, Steiger and Hurd, 1978). While extensive studies have been made on the mechanical and thermal properties of concrete containing expanded perlite (Demirboğa and Gül, 2003, Karakoc and Demirboga, 2010, Sengul et al., 2010, Topçu and Işıklıdağ,

2008), limited information is available with regard to its use in the mining industry. To the authors' knowledge, the only prior study was done by the U.S. Bureau of Mines (USBM) (USBM, 1994) who sprayed an insulation of shotcrete containing expanded perlite, to achieve a thermal conductivity of 0.36 W/(m K), and the 90th day's unconfined compressive strength (UCS) of 20.68 MPa. Unfortunately, this promising research track was apparently discontinued following the disintegration of USBM in 1995.

The objective of this study is to investigate the thermal effects of expanded perlite's addition as fine aggregate in dry-mix shotcrete, and illustrate the corresponding mechanical properties. Further, this study also highlights the process dependence of thermal properties by comparing those derived for shotcrete with the corresponding conventionally cast counterpart.

3.2 Material and methods

3.2.1 Materials and mixtures

The expanded perlite aggregate (EPA), Type GU Portland cement (CSA, 2009) and sand were locally sourced in Edmonton. The EPA is mainly composed of SiO₂ (70-75%) and Al₂O₃ (12-18%). Given its porous structure (Kramar and Bindiganavile, 2010), it was rated to absorb water at 100% of its dry mass and had a bulk density of 71.49 kg/m³ in oven-dry conditions. The sand was moist with

2.04% water and had a bulk density of 1675 kg/m^3 in oven-dry conditions. As shown in Table 3-1, mixes were designed in accordance with ACI 506.5R-09 (ACI, 2009). The sieve analyses of EPA and the sand used along with their blends were conducted as per ASTM C 126 (ASTM, 2006b) using a mechanical shaker. As plotted in Figure 3-1, the grain size distribution for the aggregates in all the mixes were within the shotcrete grading zone No.1 given in ACI 506R-05 (ACI, 2005). Besides the reference mix with no EPA, 4 other mixes were produced where sand was replaced with EPA at 4 rates of volumetric substitution namely, 25, 50, 75, and 100%. One set of 5 mixes were cast conventionally and were designated CP0, CP25, CP50, CP75 and CP100. A second set was sprayed using the dry-mix process so that these resulting five mixes were designated as SP0, SP25, SP50, SP75 and SP100, respectively.

3.2.2 Shotcreting process and sample preparation

The dry-mix shotcrete was prepared with the assistance of a local industrial facility. A certified nozzleman and a gun operator were in charge of the whole process of shooting. Shotcrete panels conforming to ASTM C1140 (ASTM, 2011) with the standard size of 610 mm (width) \times 610 mm (length) \times 89 mm (depth) were prepared. In this study, three specimens were prepared for each mix, and so 15 wooden panels were crafted earlier to yield this standard specimen size. The fine aggregate and cement were pre-mixed in a drum mixer for each batch, and

they were then stored in sealed bags for use. The SP0 batch was pre-mixed in the late afternoon on the day before the shooting, whereas the other 4 mixes were pre-mixed early in the morning of the shoot. As shown in Figure 3-2, all five mixes were shot on the same day, inside a specially fabricated hut. A plastic sheet was placed on the floor to collect the rebound after each mix shooting. The panels were propped on the hut's facing wall at an angle of 45°. After shotcreting, all panels were immediately finished and covered with plastic wraps and then transported to the curing room that was set to a temperature of 25 ± 2 °C and relative humidity of $100 \pm 5\%$ in accordance with ASTM C511 (ASTM, 2009a). Cores were drilled (50 mm diameter) from each panel per ASTM C1604 (ASTM, 2005) as illustrated in Figure 3-3. The specimens were scheduled for mechanical tests at 6 different curing ages namely, after 1 day, 3 days, 5 days, 7 days, 14 days and 28 days. Specifically, 3 cored replicates were drilled for the unconfined compressive strength (UCS) as per ASTM C42 (ASTM, 2012). 4 cored cylinders were slated for the splitting tensile strength (STS) complying with ASTM D3967 (ASTM, 2008). Note that on the 14th day, in addition to the UCS, the cored cylinders were also evaluated for the modulus of elasticity. At the end of the 28th day, an extract from a fractured specimen was examined under the Scanning Electron Microscope (SEM). Three cored cylinders were designated to establish the density and volume of permeable voids as per ASTM C642 (ASTM, 2006a)

and three more were slated for the thermal characterization. Thus, 49 cores in total were drilled out for each mix. The drilled cores were end ground using a grinding wheel. As a result, the Length/Diameter ratio (L/D) for the shotcrete cylinders was between 1 and 1.78. And only shotcrete cores in Grade 1 and Grade 2 specified in ACI 506.2-95 (ACI, 1995) were accepted as testing samples.

3.2.3 Testing methods

Firstly, the density and water absorption were determined according to ASTM C 642 (ASTM, 2006a). The microstructure for all shotcrete samples, SP25 through SP100, and also of the cast reference sample, CP0, were determined using scanning electron microscopy at 100 times magnification. Further, the mechanical properties namely, the unconfined compressive strength (UCS), the splitting tensile strength (STS) and the modulus of elasticity were evaluated as per ASTM C42 (ASTM, 2012), ASTM D3967 (ASTM, 2008) and ASTM C469 (ASTM, 2002), respectively. Figure 3-4 illustrates the set up to measure the modulus of elasticity with three linear variable differential transducers (LVDTs) to record axial deformations. In case of the shotcrete samples, the mechanical properties were corrected for the aspect ratio for each specimen as per ASTM C42 (ASTM, 2012). Besides these tests, the mechanical properties were also estimated through the non-destructive technique of measuring the ultrasonic pulse velocity (UPV), as per ASTM C597 (ASTM, 2009b) and demonstrated in Figure 3-5. It is hoped

that the results will help establish the correlation between the measured UPV and the inherent material response.

In order to evaluate the thermal properties, a thermal constants analyser that is based on the transient plane source method (TPS) and conforms to ISO 22007-2.2 (ISO, 2008) was employed. The Hot-Disk method of TPS technique was developed by Gustafsson (Gustafsson, 1990) during 1990s and it is being used widely to characterize thermal properties of construction materials (Log and Gustafsson, 2004). This technique is found to yield rapidly and simultaneously, information on the thermal conductivity and thermal diffusivity (Al-Ajlan, 2006, Bentz, 2007, Bouguerra et al., 2001, Huang and Liu, 2009, Log and Gustafsson, 2004). The key component of the TPS device is the combined heat source/temperature sensor as shown in Figure 3-6, and it actually contains the electrically conductive Nickel bifilar spirals, sandwiched by two thin Kapton sheets. It is also known as the Kapton probe in this device. Figure 3-6 (a) and Figure 3-6(b) are schematic views of the Kapton probe itself. And Figure 3-6(c) and Figure 3-6(d) are the actual view of the probe for testing. The probe is shown sandwiched between two shotcrete cylindrical sample disks each of whose thickness is 15 mm. The concrete cylinders and shotcrete cores were sawn to 15 mm thickness first and then the Kapton probe with the radius (r) of 6.403 mm was put between the two halves. In order to get accurate thermal properties, it is important that the

penetration depth, i.e. the minimum distance into the specimen at which there is no temperature change, does not exceed the sample's thickness. For the samples examined here, the calibrated constants were found to be the following: for an output power, P_o , equal to 0.1 W, the probe detected 200 points for the average temperature increase ($\Delta\bar{T}$), within an interval, t , of 20 s. Under this condition, the penetration depth was around 9 mm, which was less than the sample's thickness of 15 mm.

Figure 3-16 has briefly demonstrated the testing data analysis of TPS for the shotcrete sample SP25 here. Figure 3-16 (a) has recorded the relationship between the average transient temperature increase ($\Delta\bar{T}$) and measuring time (t), Figure 3-16(b) has shown the linear plot for the function $\Delta\bar{T}$ versus $D(\tau)$. $D(\tau)$ is a known dimensionless specific time function (Gustafsson, 1990). It is worthwhile to mention that the plot in Figure 3-16(b) was made straight and liner after a series of computational iterations to obtain the optimised thermal diffusivity (α). And at the same time, thermal conductivity (k) was calculated from the slope of this linear fitting. It is necessary to clear the fact that 9 points were skipped as shown in Figure 3-16(a). This can be helpful to eliminate the influence of Kapton insulation layer at initial time (ISO, 2008). Therefore, both thermal conductivity and thermal diffusivity are obtained by this one quick TPS test simultaneously. As indicated Figure 3-16, the average transient temperature increase ($\Delta\bar{T}$) on the

bifilar spiral of Kapton probe has been given the exact analytical solution (Gustafsson, 1990) as follows,

$$\Delta\bar{T} = P_o(\pi^{3/2}rk)^{-1}D(\tau) \quad (3.1)$$

$$\tau = \sqrt{\alpha t}/r \quad (3.2)$$

where $\Delta\bar{T}$ is the average transient temperature increase (K); P_o is the output power; r is the radius of the Kapton probe (m); k is the thermal conductivity of the testing sample (W/(m K)); $D(\tau)$ is a known dimensionless specific time function (Gustafsson, 1990), which depends on τ ; τ is the dimensionless time; α is the thermal diffusivity (m²/s); and t is the measuring time (s).

Apparently, for Formula (3.1) and (3.2), the parameters $\Delta\bar{T}$, P_o , r and t are all known parameters, whereas only k and α are unknown. Then for solutions, a series of computational iterations were conducted to fit the function $\Delta\bar{T}$ versus $D(\tau)$, until an optimised thermal diffusivity (α) was found to obtain the linear straight line. And thermal conductivity (k) was calculated from the slope of the straight line. In a word, all thermal testing data are under the same analysis procedure as shown in Figure 3-16.

3.3 Results and discussion

Results of tests on the shotcrete samples namely, SP0, SP25, SP50, SP75 and SP100 are compared with those from the cast samples (Liu et al., 2011). The

rebound associated with spraying each mix is listed in Table 3-1. It was found that the pre-mixed powder for the SP0 mix underwent setting overnight due to moist sand. Thus, this mix was ignored in further discussion. Nevertheless, it appears from Table 3-1 that there was an increase in the rebound with an increase of the amount of EPA in the fine aggregate. An earlier study on the effect of particle density on rebound in dry-mix shotcrete revealed that a lower density was beneficial to the reduction of rebound (Bindiganavile and Banthia, 2009). The results of the present investigation clearly contradict this premise. Note that in that study, the aggregate density ranged from 600-15,000 kg/m³, whereas in this investigation, the bulk density of EPA was less than 72 kg/m³. As demonstrated by Armelin and Banthia (Armelin and Banthia, 1998a, Armelin and Banthia, 1998b), the tendency for a particle to rebound is a trade off between its ability to indent the substrate on the one hand, and its susceptibility to ejection on the other. Bindiganavile and Banthia (Bindiganavile and Banthia, 2009) illustrated that assuming the lightweight aggregate reached the substrate, and it was more likely to resist ejection than a denser aggregate. However, the particle, as light as EPA, may not even be able to reach the substrate in the first place. The authors confirm that when spraying the SP100 mix, a large portion of dry material, predominantly EPA particles were seen fanning out from the stream and clearly not reaching the substrate. One may question whether the resulting wastage is to be classified as

rebound or perhaps a special case of overspray. Nevertheless, it appears that in the case of dry-mix shotcreting, there exists a lower limit to the particle density, below which the benefit on rebound is not witnessed.

3.3.1 Density and water absorption

As seen in Figure 3-7, several different densities were obtained for shotcrete samples from SP25 to SP100. It is easy to note the fact that all the densities of both shotcrete and cast samples were reduced a lot with the increasing replacement ratio of EPA. These densities reductions, especially the trend of apparent density, which has eliminated the influence of permeable pore space, can preliminarily prove that the shotcreting process based on the replacement of normal weight sands by lightweight EPA has been applied successfully. We also got the oven-dry density comparisons with previous cast samples (Liu et al., 2011). It is found that SP25, SP50 and SP75 have minor differences of about 100 kg/m³ from cast sample CP25 with 25% replacement of sands by EPA, CP50 and CP75, respectively. However, the oven-dry density of SP100, as the outlier, shows a much larger gap between that of CP100. This outlier may be caused by the dry-mix shotcreting process and the large amount of EPA that is in 100% replacement ratio. Holding the fact that EPA is highly absorptive, with an estimation of 100% water absorption, previous casting process had enough time in pre-damping and in the drum mixer with water to let the EPA absorb adequate

water. Apparently, in the dry-mix shotcreting process, the dry materials (only cement and EPA) only had very short time to meet the water in the nozzle. This is definitely inadequate for this large amount of EPA to form a paste that has enough fluidity. Thus the nozzleman per his shooting experience adjusted an excessive water amount into the mix, leading to a lower density mix SP100. On the other hand, the situations of SP25, SP50 and SP75 were better for water mixing in shotcreting nozzle, the nozzleman managed to control them to be similar to previous casting batches from the oven-dry bulk density comparisons in Figure 3-7.

In Figure 3-7, it is also interesting to mention that the margins between the oven-dry density and density after immersion as well as the density after immersion and boiling are actually the water absorption contents. Figure 3-8 is the plotting which depicts the relationship between oven-dry density and water absorption after immersion and after immersion and boiling. Nevertheless, no apparent effects are found for boiling by comparisons of the two curves except that in SP100. Nonlinearly, two extraordinary exponential expressions as tagged in Figure 3-8 were found suitable to correlate the water absorption of shotcrete samples and their corresponding oven-dry bulk densities. Generally speaking, the shotcrete's water absorption went up with the additions of EPA substantially, namely, for the batches from SP25 to SP100, the absorption changed from about a

low value of 5% to as high as 50-60%. The reason of abundant water absorption increase may be found in the SEM images as indicated in Figure 3-9. Figure 3-9(a) contains all the small samples mounted on stubs, and labels marked in blue ink read as 0, 25, 50, 75 and 100 represented CP0, SP25, SP50, SP75 and SP100, separately. The following Figure 3-9(b), Figure 3-9(c), Figure 3-9(d), Figure 3-9(e), and Figure 3-9(f), are SEM images under 100 times magnification for CP0, SP25, SP50, SP75 and SP100, correspondingly. It is worth mentioning that one cast sample CP0 was also put in the test as reference taking place of the discarded SP0. First, overview of the prepared samples in Figure 3-9(a) by tracing the white spots which are EPA can result in a general finding of the increasing EPA from CP0 to SP100. As for Figure 3-9(f), the most porous units are found in the image for SP100, and then some porous units are noticed on the image centre of Figure 3-9(e) for SP75, and also on the upper part of Figure 3-9(d) for SP50. No such porous units have been found in either CP0 or SP25. Therefore, the absence of porous units also matches SP25's low water absorption value. It can be concluded that the porous structure is strongly related to shotcrete samples' water absorption. In other words, the absorption of shotcrete can be reflected from its SEM microstructure, a more porous structure may lead to a more absorptive shotcrete.

3.3.2 Unconfined compressive strength

Testing results of the unconfined compressive strength (UCS) have been illustrated in Figure 3-10 and Figure 3-11. Again, previous UCS testing results (Liu et al., 2011) of cast batches are included here for the purpose of comparisons. It is essential to mention that the UCS values presented for shotcrete in this study were after the considerations of the Length/Diameter ratio (L/D) that is between 1 and 1.78. Therefore, strength correction factor was applied via ASTM C42 (ASTM, 2012) for getting the standard values. Figure 3-10 focuses on the UCS developments with time within 28 days. It has been found that a general form of exponential expression in Formula (3.3) can fit the UCS developments with days for both the shotcrete and cast samples very excellently, Formula (3.3) is shown as below,

$$f_c = a_1 + b_1 e^{c_1 t} \quad (3.3)$$

where f_c is the UCS (MPa), t is the time in days, a_1, b_1 and c_1 are parameters obtained by fitting, they are listed in Table 3-2 along with coefficient of determination (R^2). Staring from Table 3-2, and then referring to Figure 3-10, we can find that a_1 values are roughly the 28th day UCS values. Before the time at about 14th day, UCS curves had a more rapidly upward trend, and after 14th day, they levelled out to the stable stage until 28th day. By comparing Figure 3-10(a) and Figure 3-10(b), it is very not difficult to observe higher UCS values for SP25

and SP75, and similar values for SP50. And because the 50 mm core barrel was used for the shotcrete samples for closer L/D to standard, these UCS values are considered to be underestimated, in other words, larger UCS values can be expected under the size of 75 mm (ASTM, 2005, Bartlett and MacGregor, 1994), which is the size for the moulds of cast samples (Liu et al., 2011). These larger UCS values may come from the effects of better compaction in the shotcreting process with great momentum. Figure 3-10(b) has indicated the fact that the UCS values drop with the increasing volume of EPA in proportions. Similar observations were also obtained by other researchers (Karakoc and Demirboga, 2010, Sengul et al., 2010, Topçu and Işıklıdağ, 2008). This trend can be attributed to the porous microstructure of EPA itself, and possible weaker interfacial transition zone influenced by the introduction of EPA. Unlike cast samples, the uncertain water/cement ratio must be the factor that can affect the USC values of shotcrete samples. From the well known Abrams' water/cement ratio rule (Kumar and Monteiro, 1993), larger water/cement ratio leads to higher porosity that in sequence weakens the matrix of concrete. Therefore, three factors, in terms of extent of compaction, percentage of EPA and water/cement ratio, are believed as primary issues to determine the UCS of shotcrete values. It is then of interest to have noticed the flat UCS curve for SP100 without gaining too much strength from the 1st to 28th day, with an exponential expression bearing R^2 of 0.94, this

discrepancy of low UCS values in SP100 may also come from the excess water additions as explained in its low density during the dry shotcreting process.

In order to clarify the correlation between the oven-dry density and UCS values, The UCS values was scattered with power function fittings in Figure 3-11. These two curves look similar to each other, whereas the shotcrete curve seems like have a more climbing trend than that of cast samples regarding to their oven-dry densities.

3.3.3 Modulus of elasticity

Figure 3-12 describes the stress-strain responses before failure for SP25 to SP100, in four distinctive curves from top to bottom. Then modulus of elasticity was calculated from the formula in C469 (ASTM, 2002), namely, from the first point that has 40% ultimate load and the second point that is mostly near to the strain of 50 millionths. Then, the obtained modulus of elasticity values from about 3.5 GPa to 16 GPa are plotted and fitted with the power functions regarding to oven-dry bulk density in Figure 3-13. In the mean time, comparison has been performed with the red curve of modulus values calculated from the empirical formula in ACI 213 (ACI, 2003), which is also shown within Figure 3-13. It is found that all the elasticity of modulus values except SP25, are well depicted by this empirical ACI curve.

3.3.4 Splitting tensile strength

The results of splitting tensile strength (STS) test, also well known as Brazilian test, are displayed in Figure 3-14. Basically, similar trends are noticed as that in Figure 3-10 for UCS. It is interesting to mention that the STS results of 50 mm diameter core may be larger than that from 75 mm shotcrete cores, namely, their values are to some extent overestimated, yielding to Bažant's size effect law (Bažant, 1984, Bažant et al., 1991). However, comparisons were still made with the STS results from 75 mm cast cylinders. Again a general form of exponential expression in Formula (3.4) is found to be suitable for the STS formation with days for both the shotcrete and cast samples. Formula (3.4) is displayed as follows,

$$f_{STS} = a_2 + b_2 e^{c_2 t} \quad (3.4)$$

where f_{STS} represents the STS (MPa), t is the time in days, a_2 , b_2 and c_2 are parameters obtained by fitting, they are listed in Table 3-3 along with coefficient of determination (R^2). However, several poor fittings with lower R^2 numbers ($R^2 < 0.9$) are witnessed in Table 3-3. Comparing STS curves with the ones of UCS, it seems like the results of UCS are distributed in a more reliable way, which can be fitted better. Therefore, the relationship between UCS and STS has raised great interest here. Then Figure 3-15 pops out to show three different groups of relationships between UCS and STS. All three groups are under the description of

power functions, the first one is the ACI 363R curve (ACI, 1992) as marked in the graph, the second is the relationship obtained from all the cast samples containing EPA (Liu et al., 2011), the third one is the curve fitted from all the shotcrete samples. From the first to the third curve, the arguments of the power functions have increased from 0.5 to 0.925. The ACI 363R curve (ACI, 1992) with the argument of 0.5 is the suggestion for normal weight high strength ($21 \text{ MPa} < f_c < 83 \text{ MPa}$) concrete, whereas other researchers also published the arguments of 0.79 and 0.8 (Gardner and Poon, 1976, Oluokun et al., 1991) with present authors' 0.72 (Liu et al., 2011) from cast samples. The data from the shotcrete samples suggest a nearly linear relationship with a 0.9 power. This effect of consolidation is consistent with research on self compacted concrete wherein a power-law with an exponent of 1.04 was obtained (Sekhar and Rao, 2008).

3.3.5 Thermal properties

3.3.5.1 Thermal conductivity

Figure 3-17(a) and (b) give us the thermal conductivity of shotcrete and cast samples (Liu et al., 2011) in both air-dry (48 hours in atmosphere) with the additions of EPA. Generally speaking, thermal conductivity goes down with the increasing amount of EPA. Because EPA is known to have a very low thermal

conductivity of 0.04 W/(m K) (Khan, 2002, Topçu and Işıkdağ, 2008), it is evident to see the increasing effects on reducing thermal conductivity with more portions of EPA. Without considering the influence of moisture contents, another important issue is from the comparisons between oven-dry shotcrete and cast samples by viewing Figure 3-17 (a) and (b) together, or even point by point from left to right (SP100 to SP25 in orders), there are no obvious differences between shotcrete samples and cast sample in terms of conductivity values, except an outlier of SP100 with the lowest value of about 0.2 W/(m K) . SP100's lower value than that of CP100 can also be explained by its excess water injection as discussed in previous sections, the larger water/cement ratio led to an even more porous structure, which can be witnessed from the SEM image in Figure 3-9(f). As a result, SP100 matrix contains more dry air that has the thermal conductivity of only 0.026 W/(m K) (Sukhatme, 2011). And also, the shotcreting process results in greater compaction than with conventional casting. Nevertheless, it is evident that the thermal conductivity of shotcrete samples was less than or comparable to that for identical mixes cast conventionally. While not dealing with the shotcrete process, Nguyen *et al.* (Nguyen et al., 2010) also found that superior compaction does not lead to obvious change of thermal conductivity.

From Figure 3-17(a) and (b), another observation is that air-dry samples' curves are all above oven-dry samples' curves; this means air-dry samples possess larger

values of thermal conductivity than oven-dry samples. One evident characteristic in air-dry samples are the moisture contents. Consequently, Figure 3-18 was plotted for the correlation between air-dry conductivity/oven-dry conductivity ratios and moisture contents. Two outstanding linear relationships were found for shotcrete and cast samples, respectively. The reason why moisture contents would increase thermal conductivity is because that the thermal conductivity value of water is 0.6 W/(m K) (Sukhatme, 2011), once the pores filled with dry air are occupied by water, the values of thermal conductivity are definitely expected to be higher.

3.3.5.2 Thermal diffusivity and heat capacity

Except thermal conductivity, thermal diffusivity can also be obtained by TPS at the same time. As shown in Figure 3-17(c) and (d), the effects of EPA additions can reduce thermal diffusivities for both shotcrete and cast samples. By comparing Figure 3-17(c) and (d), especially the points representing individual samples, we can make the conclusion that no obvious difference has been noticed between shotcrete and cast samples regarding the oven-dry thermal diffusivities. And by noticing the air-dry curves in both Figures 3-17(c) and (d), the moisture contents' role on thermal diffusivity becomes unclear, because two graphs lead to conflicting influences. More works are expected to explore rules on this part.

As for the thermal properties, there is another important parameter that is closely related thermal conductivity and thermal diffusivity. Actually, the above three parameters, provided any two are known, the third one that is volumetric heat capacity can be calculated via the basic formula among them.

$$\rho \cdot C_p = k/\alpha \quad (3.5)$$

where α is the thermal diffusivity (m^2/s); k is the thermal conductivity ($\text{W}/(\text{m K})$); ρ is the corresponding density (kg/m^3); C_p is the specific heat capacity ($\text{J}/(\text{kg K})$); and ρC_p together is known as the volumetric heat capacity ($\text{J}/(\text{m}^3 \text{K})$). One point has to be mentioned here is the calculation of the specific heat capacity (C_p), whose value needs also the involvement of density (ρ), which is an independent parameter. The reason why we specifically mention the specific heat capacity (C_p) here, it is because this parameter is commonly used in the mainstream finite element method software, such as ABAQUS[®] (Abaqus Users Manual). The values of both specific heat capacity and the volumetric heat capacity have been listed in Table 3-4. Overall speaking, air-dry samples have larger heat capacities than oven-dry samples. Nevertheless, SP25 has an opposite way. It is for sure that more efforts will be needed before we can figure out this phenomenon clearly.

3.3.5.3 Correlation with UPV

Figure 3-19 has found the notable exponential relationship between the ultrasonic pulse velocity (UPV) and thermal conductivity. We can notice that the thermal conductivity rises with the increasing values of UPV, the air-dry curve almost parallels with the oven-dry curve. Similar exponential relationship was also found on other's work (Karakoc and Demirboga, 2010).

Figure 3-20 is the graph which describes correlation between UPV and thermal diffusivity, again an exponential relationship was found here. In an overview, the thermal diffusivity increases with the UPV's additions. However, the shapes of curves for air-dry and oven-dry samples differ a little bit with each other.

From above correlations, we can lead to the conclusion that UPV has exponential correlations with both thermal conductivity and diffusivity. And more work can be done to find the empirical equations for practical applications to predict thermal properties through UPV.

3.4 Concluding remarks

This paper investigated the use of expanded perlite aggregate (EPA) as a lightweight inclusion to achieve a thermally more resistant structural material for underground insulation. Five mixes, with increasing EPA/sand ratio were prepared both conventionally and through dry-mix shotcreting. The thermal

constants were evaluated using a device based on the transient plane heat source method. The results show that dry-mix shotcrete with up to 75% of sand substituted with EPA offers superior thermal properties without compromising its mechanical performance. The principal findings are enumerated as follows:

1. The addition of expanded perlite as substitution to sand results in a reduction in the density of the mixes. When these mixes were sprayed through the dry-mix shotcrete process, all but one had similar values of rebound. However, substituting the sand entirely with EPA had twice the rebound, which is likely due to its significantly low particle density. The water demand was seen to increase due to dry-mix shotcreting at all levels of EPA dosage.
2. The unconfined compressive strength (UCS) and splitting tensile strength (STS) of shotcrete samples were generally found to be higher than of conventionally cast samples. The effect of density on the UCS was not influenced by the shotcreting process. However, the STS/UCS ratio was higher in case of dry-mix shotcrete than with the conventionally cast series.
3. The thermal conductivity and the thermal diffusivity of the mix dropped with an increase in the EPA content and no significant difference was observed between the cast and sprayed samples. Superior compaction and higher water demand associated with the shotcrete process did not noticeably affect these

thermal constants. As well, these parameters correlate with the ultrasonic pulse velocity (UPV).

Tables in Chapter 3

Table 3-1 Mix proportions of shotcrete and corresponding rebound

Mix number	Replacement percentage (%)	Cement (kg/m ³)	Sand (kg/m ³)(OD)	EPA (kg/m ³)(OD)	Rebound (%)
SP0*	0	519.5	1623.5	0.00	21.0
SP25	25	519.5	1217.6	17.3	11.4
SP50	50	519.5	811.7	34.6	16.6
SP75	75	519.5	405.9	52.0	15.0
SP100	100	519.5	0.00	69.3	29.1

*SP0 was pre-mixed by drum mixer one day before the shooting process to tighten schedule, but the mix started to hydrate, resulting in hardened blocks. However, it was still shot to obtain the rebound.

Table 3-2 Exponential fitting parameters for UCS with days

Mix number	$f_c = a_1 + b_1 e^{c_1 t}$			R^2
	a_1	b_1	c_1	
SP25	44.68272	-37.0525	-0.20975	0.94424
SP50	31.73912	-22.5118	-0.16013	0.97335
SP75	26.91529	-31.7094	-0.59609	0.90735
SP100	4.774130	-3.95559	-0.07978	0.93549
CP0	43.07098	-37.8425	-0.24202	0.92402
CP25	40.84724	-32.8135	-0.15673	0.95123
CP50	32.46282	-28.0970	-0.30360	0.96764
CP75	22.96191	-17.1607	-0.34589	0.97421
CP100	16.79469	-10.6182	-0.19099	0.94213

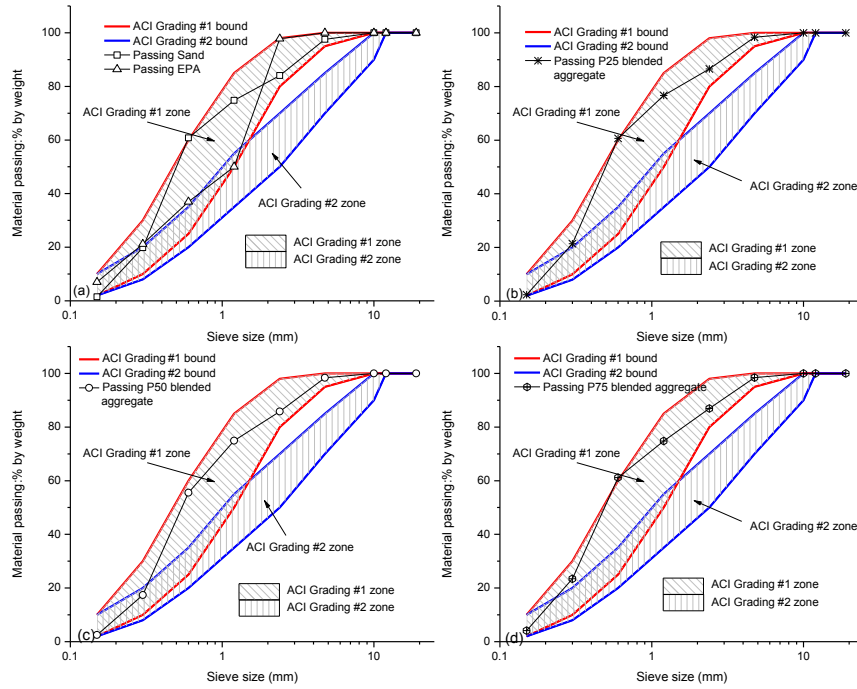
Table 3-3 Exponential fitting parameters for STS with days

Mix number	$f_{STS} = a_2 + b_2 e^{c_2 t}$			
	a_2	b_2	c_2	R^2
SP25	6.83474	-6.63106	-0.25857	0.96404
SP50	4.41345	-4.07704	-0.35996	0.99537
SP75	4.28686	-4.49955	-0.49625	0.97789
SP100	1.26116	-0.85845	-0.06595	0.8253
CP0	4.27525	-3.19344	-0.19042	0.80818
CP25	4.11873	-3.24321	-0.14935	0.98988
CP50	3.73280	-3.06415	-0.34383	0.85569
CP75	2.58595	-1.92383	-0.54863	0.77931
CP100	2.28852	-2.00927	-0.73070	0.98873

Table 3-4 Heat capacity for shotcrete samples

Mix number	Volumetric heat capacity	Specific heat capacity	Volumetric heat capacity	Specific heat capacity
	(MJ/(m ³ K))	(J/kg K)	(MJ/(m ³ K))	(J/kg K)
	Air-dry shotcrete		Oven-dry shotcrete	
SP25	1.26	568.36	1.65	793.56
SP50	1.58	814.89	1.37	783.12
SP75	1.50	807.30	1.22	735.76
SP100	0.72	688.67	0.48	641.77

Figures in Chapter 3



(a) EPA and sands distribution; (b) SP25 distribution;

(c) SP50 distribution; (d) SP75 distribution

Figure 3-1 Grading distributions of sands, EPA and blended aggregates



Figure 3-2 Shotcreting against panels



Figure 3-3 Coring machine for the sample drilling

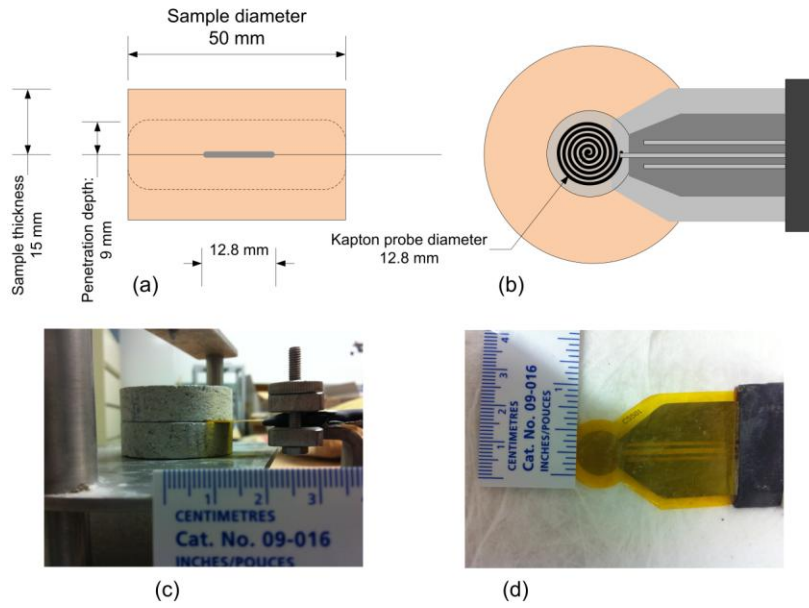


Figure 3-4 Test setup for modulus of elasticity



Figure 3-5 Test setup for UPV

Kapton probe and shotcrete samples



(a) Schematic of front view of the probe and two sample halves; (b) Schematic of plan view of the probe and one sample half; (c) Front view of the probe and two sample halves; (d) Plan view of the probe

Figure 3-6 TPS probe schematic and setup

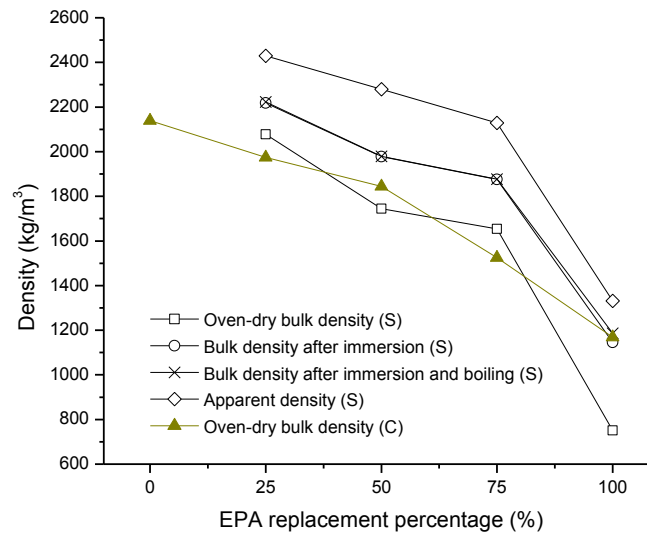


Figure 3-7 Effects of EPA on densities of shotcrete

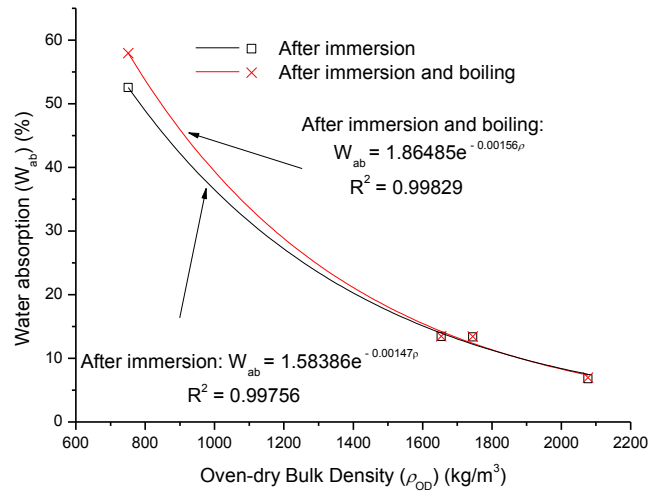
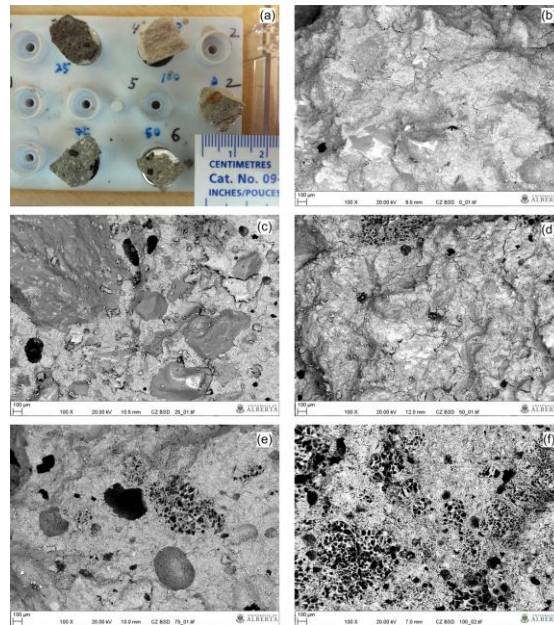
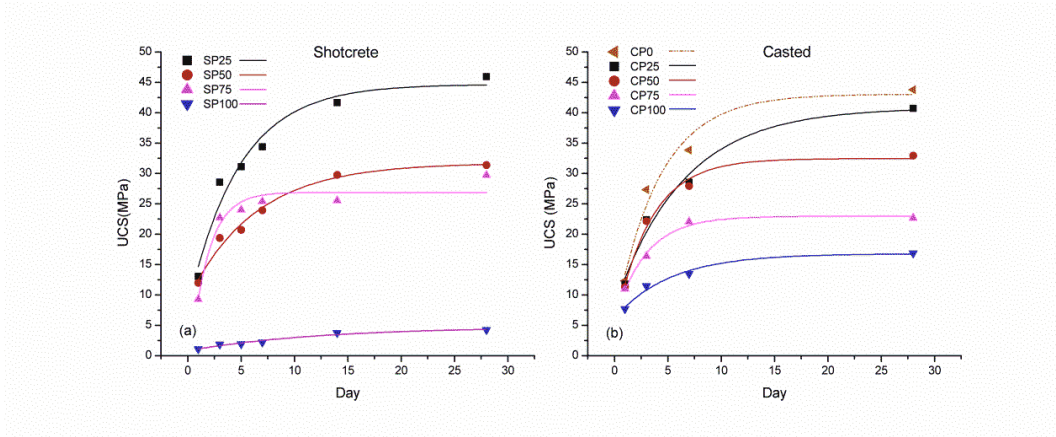


Figure 3-8 Effects of EPA on water absorptions of shotcrete



(a) Small samples prepared for SEM test, labeled with blue ink; (b) SEM image of cast sample CP0; (c) SEM image of shotcrete sample SP25; (d) SEM image of shotcrete sample SP50; (e) SEM image of shotcrete sample SP75; (f) SEM image of shotcrete sample SP100

Figure 3--9 SEM images of small samples



(a) Shotcrete samples;

(b) Cast samples

Figure 3-10 UCS developments with days

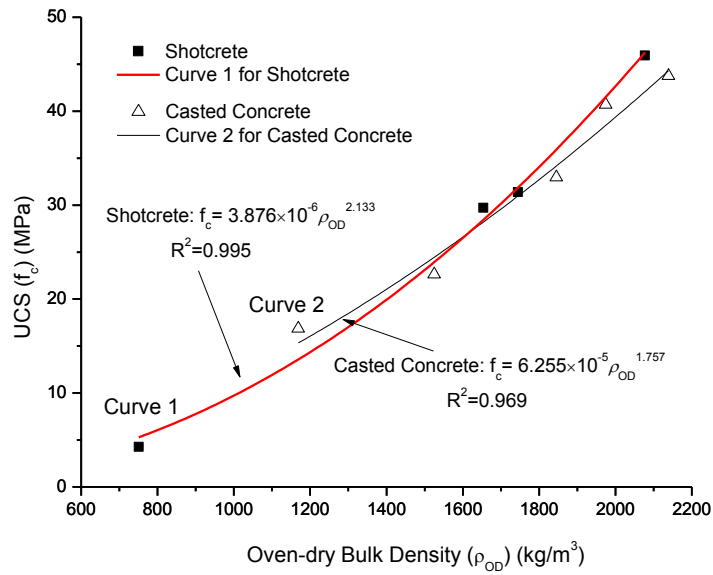


Figure 3-11 EPA effects on UCS of shotcrete and cast samples

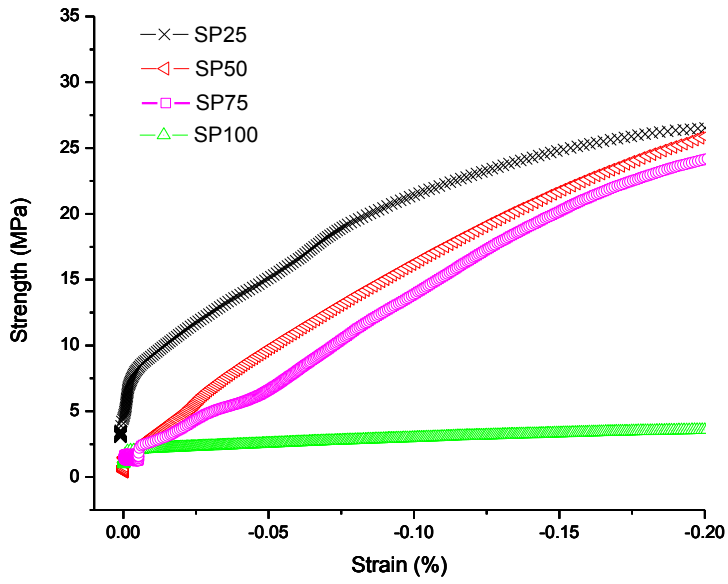


Figure 3-12 Stress-strain curves of shotcrete samples

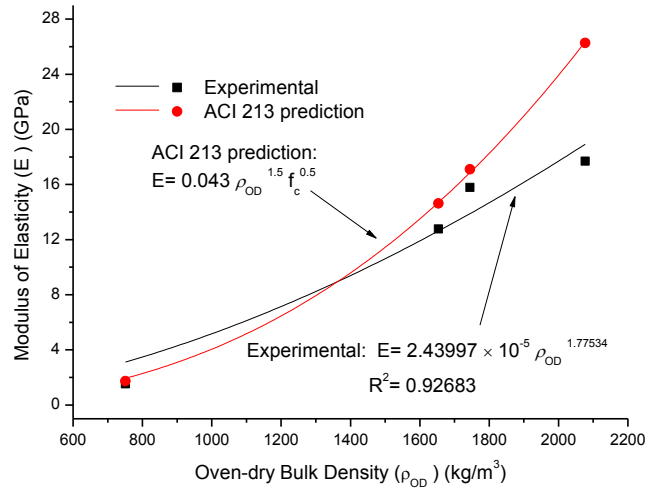
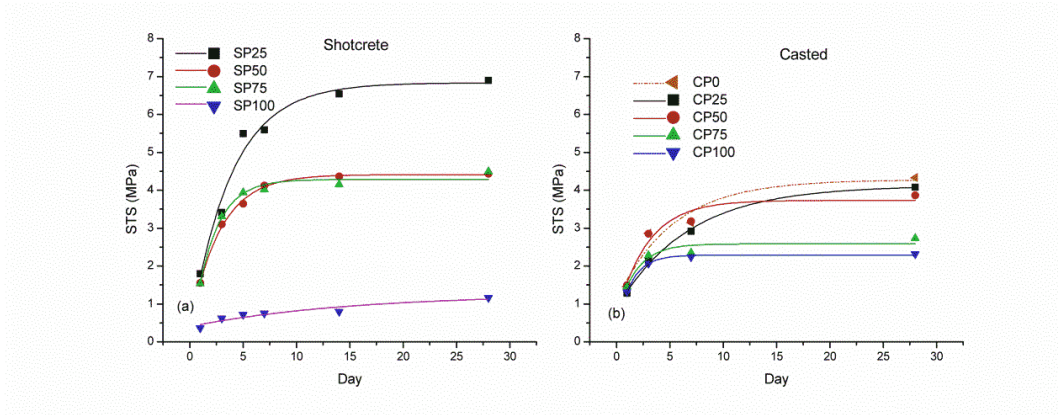


Figure 3-13 Effects of EPA on the modulus of elasticity of shotcrete



(a) Shotcrete samples;

(b) Cast samples

Figure 3-14 STS developments with days

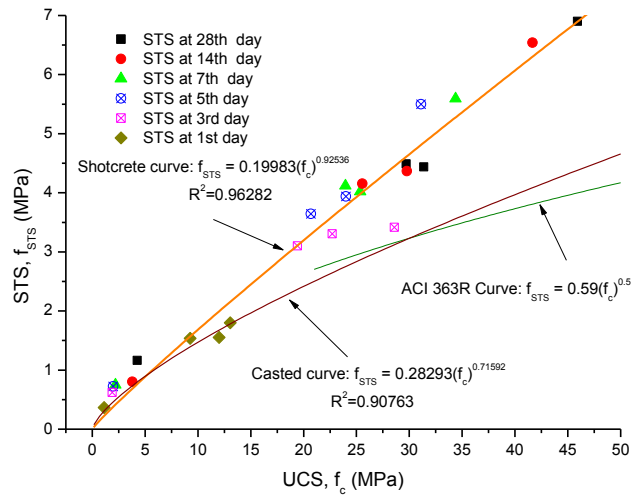
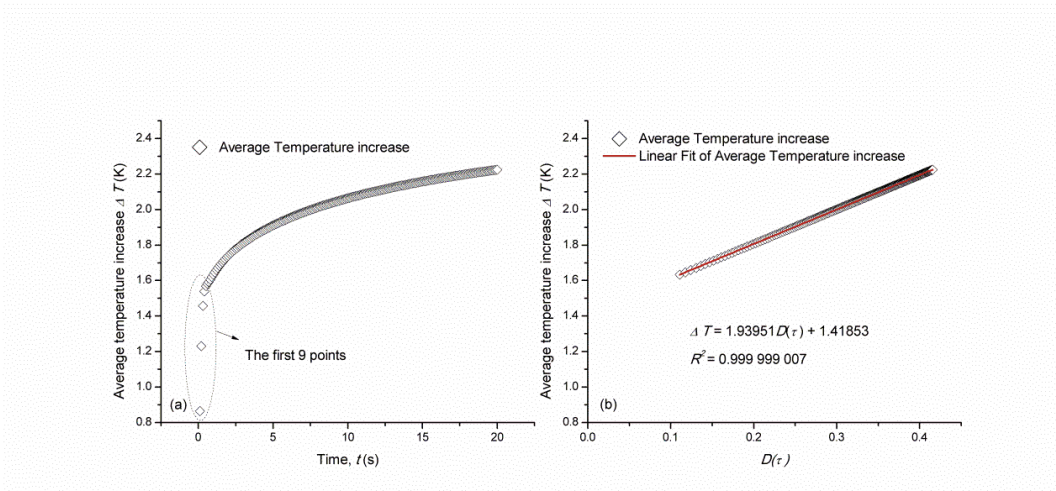
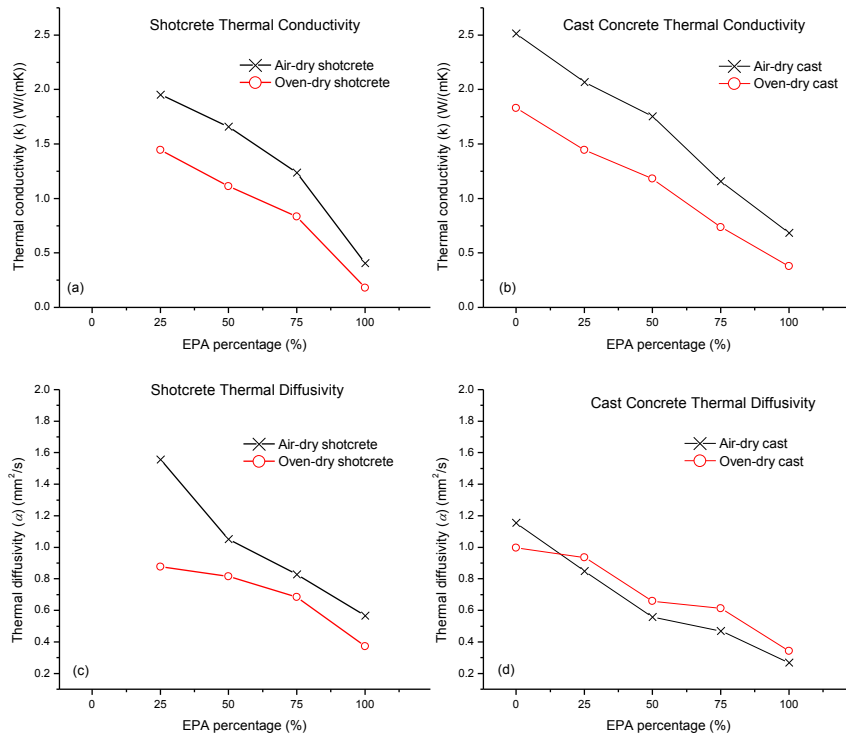


Figure 3-15 Correlation between UCS and STS



(a) Average temperature increase versus measuring time; (b) Linear fitting between Average temperature increase and the dimensionless specific time function

Figure 3-16 Original temperature data of SP25 from TPS



(a) Thermal conductivity of shotcrete samples; (b) Thermal conductivity of cast samples;
 (c) Thermal diffusivity of shotcrete samples; (d) Thermal diffusivity of cast samples

Figure 3-17 Thermal conductivity and diffusivity of samples

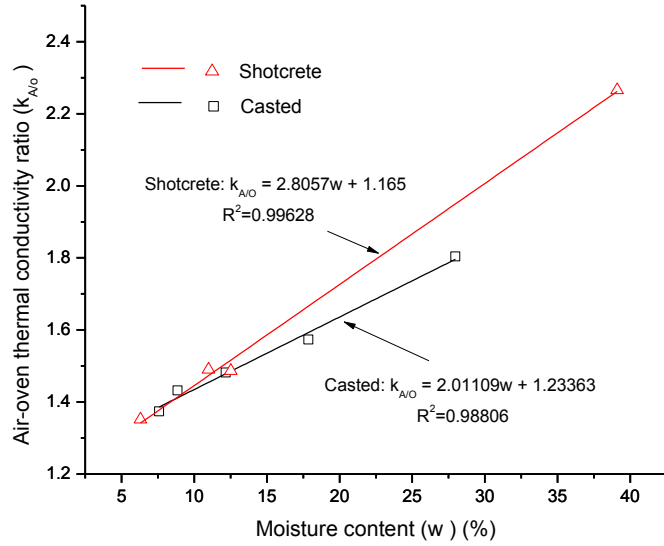


Figure 3-18 Linear fitting between moisture contents and the air-dry by oven-dry thermal conductivity ratio

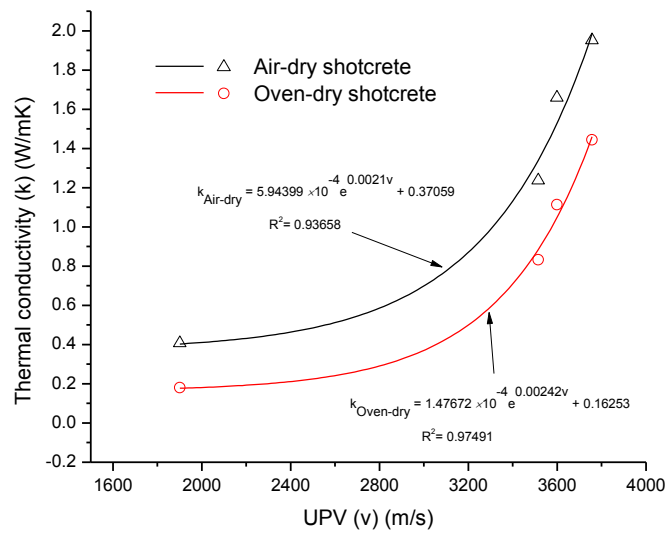


Figure 3-19 Correlation between UPV and thermal conductivity

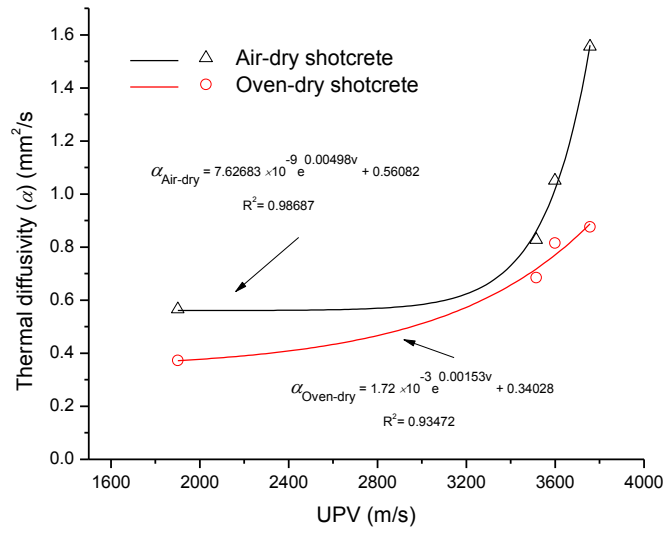


Figure 3-20 Correlation between UPV and thermal diffusivity

References

- Abaqus Users Manual, V. 6.10-1. *Dassault Systemes Simulia Corp., Providence, RI.*
- ACI (1992) State-of-the-Art report on high-strength concrete (ACI-363R). Farmington Hills, MI, American Concrete Institute.
- ACI (1995) Specification for shotcrete (ACI 506.2-95). Farmington Hills, MI, American Concrete Institute.
- ACI (2003) Guide for structural lightweight aggregate concrete (ACI 213R-03). Farmington Hills, MI, American Concrete Institution.
- ACI (2005) Guide to shotcrete (506R-05). Farmington Hills, MI, American Concrete Institute.
- ACI (2009) Guide for specifying underground shotcrete (506.5R-09). Farmington Hills, MI, American Concrete Institute.
- Al-Ajlan, S. A. (2006) Measurements of thermal properties of insulation materials by using transient plane source technique. *Applied Thermal Engineering*, 26, 2184-2191.
- Anon (1961) Perlite roof deck and insulating concrete. *Concrete Construction*, 6, 95-97.
- Armelin, H. & Banthia, N. (1998a) Development of a general model of aggregate rebound for dry-mix shotcrete—(Part II). *Materials and Structures*, 31, 195-202.
- Armelin, H. & Banthia, N. (1998b) Mechanics of aggregate rebound in shotcrete—(Part I). *Materials and Structures*, 31, 91-98.
- Armelin, H. S. & Helene, P. (1995) Physical and mechanical properties of steel-fiber reinforced dry-mix shotcrete. *ACI Materials Journal*, 92.
- ASTM (2002) Standard test method for static modulus of elasticity and poisson's ratio of concrete in compression (ASTM C 469). West Conshohocken, Pennsylvania, ASTM International.
- ASTM (2005) Standard test method for obtaining and testing drilled cores of shotcrete (C1604/C1604M-05). West Conshohocken, Pennsylvania, ASTM International.
- ASTM (2006a) Standard test method for density, absorption, and voids in hardened concrete (ASTM C642 -06). West Conshohocken, Pennsylvania, ASTM International.
- ASTM (2006b) Standard test method for sieve analysis of fine and coarse aggregate (ASTM C126-06). West Conshohocken, Pennsylvania, ASTM International.

- ASTM (2008) Splitting tensile strength of intact rock core specimens (ASTM D3967-08). West Conshohocken, Pennsylvania, ASTM International.
- ASTM (2009a) Standard specification for mixing rooms, moist cabinets, moist rooms, and water storage tanks used in the testing of hydraulic cements and concretes (C511-09). West Conshohocken, Pennsylvania, ASTM International.
- ASTM (2009b) Standard test method for pulse velocity through concrete (ASTM C 597-09). West Conshohocken, Pennsylvania, ASTM International.
- ASTM (2011) Standard practice for preparing and testing specimens from shotcrete test panels (C1140/C1140M-11). West Conshohocken, Pennsylvania, ASTM International.
- ASTM (2012) Standard test method for obtaining and testing drilled cores and sawed beams of concrete (ASTM C42 M-12). West Conshohocken, Pennsylvania, ASTM International.
- Banthia, N., Trottier, J. F. & Beaupré D. (1994) Steel-fiber-reinforced wet-mix shotcrete: comparisons with cast concrete. *Journal of Materials in Civil Engineering*, 6, 430-437.
- Bartlett, F. M. & MacGregor, J. G. (1994) Effect of core diameter on concrete core strengths. *ACI Materials Journal*, 91.
- Bažant, Z. P. (1984) Size effect in blunt fracture: concrete, rock, metal. *Journal of engineering mechanics*, 110, 518-535.
- Bažant, Z. P., Kazemi, M. T., Hasegawa, T. & Mazars, J. (1991) Size effects in Brazilian split-cylinder tests: Measurements and fracture analysis. *ACI Materials Journal*, 88, 325-333.
- Beaupré D. (1994) Rheology of high-performance shotcrete. Canada, The University of British Columbia (Canada).
- Bentz, D. P. (2007) Transient plane source measurements of the thermal properties of hydrating cement pastes. *Materials and Structures*, 40, 1073-1080.
- Bindiganavile, V. & Banthia, N. (2009) Effect of particle density on its rebound in dry-mix shotcrete. *Journal of Materials in Civil Engineering*, 21, 58-64.
- Bottomley, P. (1985) The reduction in heat flow due to the insulation of rock surfaces in mine airways. *2nd US Mine Ventilation Symposium*. Reno, NV.
- Bottomley, P. & van Rensburg, B. (1987) The insulation of rock surfaces-an empirical study. *Journal of the Mine Ventilation Society of South Africa*, 40, 41-45.
- Bouguerra, A., A ĩ-Mokhtar, A., Amiri, O. & Diop, M. B. (2001) Measurement of thermal conductivity, thermal diffusivity and heat capacity of highly

- porous building materials using transient plane source technique. *International Communications in Heat and Mass Transfer*, 28, 1065-1078.
- Brouk, J. J. (1949) Perlite aggregate: Its properties and uses. *Journal of the American Concrete Institute*, 46, 185-190.
- Chellam, S. (1992) Thermal insulation of underground mine workings at deep levels. *Department of Mining Engineering*. Rapid City, South Dakota, South Dakota School of Mines and Technology.
- Ciullo, P. A. (1996) The industrial minerals. *Industrial minerals and their uses: a handbook and formulary*. Westwood, New Jersey, Noyes Publication.
- CSA (2009) *CAN/CSA A23.1/A23.2: Concrete Materials and Methods of Concrete Construction/Methods of Tests and Standard Practices for Concrete*, Mississauga, Ontario, Canada, Canadian Standard Association.
- Demirboğa, R. & Gül, R. (2003) The effects of expanded perlite aggregate, silica fume and fly ash on the thermal conductivity of lightweight concrete. *Cement and Concrete Research*, 33, 723-727.
- Gallus, J. P., Watters, L. T. & Pyle, D. E. (1979) Performance of oilwell cementing compositions in geothermal wells. *Old SPE Journal*, 19, 233-241.
- Gardner, N. J. & Poon, S. M. (1976) Time and temperature effects on tensile, bond, and compressive strengths. *Journal of the American Concrete Institute*, 73, 405-409.
- Gustafsson, S. E. (1990) Transient plane source techniques for thermal conductivity and thermal diffusivity measurements of solid materials. *Review of Scientific Instruments*, 62, 797-804.
- Hartman, H. L., Mutmanský, J. M., Ramani, R. V. & Wang, Y. J. (1998) Heat sources and effects in mines. *Mine ventilation and air conditioning. Third Edition*.
- Hoek, E. & Brown, E. T. (1990) Chapter 15: Shotcrete support. *Underground excavations in rock*. Spon Press.
- Huang, L. & Liu, L.-S. (2009) Simultaneous determination of thermal conductivity and thermal diffusivity of food and agricultural materials using a transient plane-source method. *Journal of Food Engineering*, 95, 179-185.
- ISO (2008) *Plastics — Determination of thermal conductivity and thermal diffusivity — Part 2: Transient plane heat source (hot disc) method*. Geneva, Switzerland, International Organization for Standardization.
- Kaiser, P. K. & Tannant, D. D. (2001) The role of shotcrete in hard-rock mines. *Underground Mining Methods: Engineering Fundamentals and International Case Studies*, 579-592.

- Karakoc, M. B. & Demirboga, R. (2010) HSC with expanded perlite aggregate at wet and dry curing conditions. *Journal of Materials in Civil Engineering*, 22, 1252-1259.
- Khan, M. I. (2002) Factors affecting the thermal properties of concrete and applicability of its prediction models. *Building and Environment*, 37, 607-614.
- Kramar, D. & Bindiganavile, V. (2010) Mechanical properties and size effects in lightweight mortars containing expanded perlite aggregate. *Materials and Structures*, 44, 735-748.
- Kumar, M. P. & Monteiro, J. M. (1993) *Concrete: Microstructure, properties, and materials*, The McGraw Hill Companies Inc, College Custom Series.
- Leung, C. K. Y., Lai, R. & Lee, A. Y. F. (2005) Properties of wet-mixed fiber reinforced shotcrete and fiber reinforced concrete with similar composition. *Cement and Concrete Research*, 35, 788-795.
- Liu, W. V., Apel, D. B. & Bindiganavile, V. (2011) Thermal characterisation of a lightweight mortar containing expanded perlite for underground insulation. *International Journal of Mining and Mineral Engineering*, 3, 55-71.
- Log, T. & Gustafsson, S. E. (2004) Transient plane source (TPS) technique for measuring thermal transport properties of building materials. *Fire and Materials*, 19, 43-49.
- Morgan, D. R., Rich, L. & Lobo, A. (1998) About face: Repair at port of Montreal. *Concrete International*, 20, 66-73.
- Nguyen, T. T., Picandet, V., Carre, P., Lecompte, T., Amziane, S. & Baley, C. (2010) Effect of compaction on mechanical and thermal properties of hemp concrete. *European Journal of Environmental and Civil Engineering*, 14, 545-560.
- Oluokun, F. A., Burdette, E. G. & Deatherage, J. H. (1991) Splitting tensile strength and compressive strength relationships at early ages. *ACI Materials Journal*, 88, 115-121.
- Pirogov, A. A., Yutina, A. S., Rakina, V. P. & Volkov, N. V. (1972) Heat-insulating concretes. *Refractories (English translation of Ogneupory)*, 13, 211-215.
- Probert, S. D. & Giani, S. (1976) Thermal insulants. *Applied Energy*, 2, 83-116.
- Reichard, T. W. (1971) Mechanical properties of insulating concretes. *Reprint: Mechanical Properties of Insulating Concretes*. United States.
- Rispin, M. & Brooks, J. (2001) A shotcrete in North American underground mines: Yesterday, today and tomorrow. *CIM bulletin*, 94, 76-79.

- Sekhar, T. S. & Rao, P. S. (2008) Relationship between compressive, split tensile, flexural strength of self compacted concrete. *International Journal of Mechanics and Solids*, 3, 157-168.
- Sengul, O., Azizi, S., Karaosmanoglu, F. & Tasdemir, M. A. (2010) Effect of expanded perlite on the mechanical properties and thermal conductivity of lightweight concrete. *Energy and Buildings*, 43, 671-676.
- Singh, M. & Garg, M. (1991) Perlite-based building materials - a review of current applications. *Construction and Building Materials*, 5, 75-81.
- Steiger, R. W. & Hurd, M. K. (1978) Lightweight insulating concrete for floors and roof decks. *Concrete Construction - World of Concrete*, 23, 411-413, 415, 420, 422.
- Sukhatme, S. P. (2011) Some thermophysical properties of selected materials. *A Text Book on Heat Transfer*. Cambridge, Massachusetts, Phlogiston Press.
- Topçu, İ. B. & Işıklıdağ, B. (2008) Effect of expanded perlite aggregate on the properties of lightweight concrete. *Journal of Materials Processing Technology*, 204, 34-38.
- USBM (1994) An 'insulating' shotcrete for heat abatement in deep mines. *Technology News* 434.
- Warner, J. (1995) Understanding shotcrete – the fundamentals. *Concrete International*, 59-64.
- Yi, X. (1996) Characteristics of different types of support in rockburst conditions. *Proc. of the 2nd North American Rock Mechanics Symposium*.
- Yoggy, G. D. (2000) The history of shotcrete. *Shotcrete American Shotcrete Association*, 2, 28-29.

Chapter 4 Comparison of methods in theoretical analysis of thermal insulation for underground tunnels³

4.1 Introduction

Nowadays, underground mines are going increasingly deeper to keep up with the increase in the demand for minerals. The geothermal heat emanating from the rock mass, increases significantly with mining depth and, is considered to be the primary contributor (Pickering and Tuck, 1997, Rawlins and Phillips, 2001) of total heat load in deep mines. Therefore, the requirements of ventilation and mine-cooling systems also rise proportionately, making substantial costs of the operational and cooling system. One possible way of reducing this heat load is to use appropriate materials to insulate the rock surface of mine openings. The insulation layer functions as a thermo-barrier to abate the heat flow from the rock mass to the atmosphere inside the mine. Usually such a material is chosen keeping a balance between its capacity to support the overburden rock mass and its thermal insulation.

³ The content of this Chapter has been submitted and under peer review in a journal manuscript: Liu, W. V., Apel, D. B., Bindiganavile, V. S. & Szymanski, J. K. (2012) Comparison of methods in theoretical analysis of thermal insulation for underground tunnels. *CIM Journal (under peer review)*.

The problem of heat flow into underground tunnels is actually an issue, which has a radial transient diffusion of heat inside an infinite rock mass region with an internal boundary made by the tunnels or shafts of the mine which are mostly cylindrical, as shown in Figure 4-1(a), rock temperature profile experiences a drop near the tunnel surface, but maintains constant as virgin rock temperature (T_v) far away. One difficulty in the application of both theoretical and empirical models is in determining the outer boundary in the infinite rock mass region. The application of insulation makes it even more complicated. To simplify the analysis, the thermal flow problem in cylindrical systems is considered as a one-dimensional transient heat conduction problem in a two-layer slab, with the rock mass layer having infinite length. Even with this assumption, the analytical solutions of simplified transient conduction in composite slabs are found to be too sophisticated to solve, especially the solutions relating to eigenvalues (de Monte, 2000, de Monte 2006, Lu and Tervola, 2005, Sun and Wichman, 2004).

Many attempts have been made to provide theoretical proofs for the thermal insulation in underground mines, but so far none of them has generated a generalised approach. For instance, Bottomley (Bottomley, 1985) used the Equivalent Surface Heat Transfer Coefficient to predict thermal flow effects, and this method assumed that thermal capacity of insulation layer can be neglected, however, no proof was performed to show the reliability of the results. Ashworth

(Ashworth, 1992) established and solved the analytical conduction models but only for the steady-state heat flow, which cannot represent the transient phenomenon in reality, and is further influenced by the definition of the outer boundary. Chellam (Chellam, 1992) simulated thermal insulation in underground openings assuming a 50 m outer boundary. On the other hand, Rao (Rao et al., 1994) assumed a 32 m outer boundary. In all such cases, the boundary dimension appears to be arbitrary. It is clear therefore that existing reports do not provide sufficient confidence on a model to implement in general practice.

In the study reported here from the University of Alberta, shotcrete was examined as the insulating layer. Employed typically as rock support in underground mines, the use of shotcrete as thermal insulation was initiated by the U.S Bureau of Mines in 1994 (USBM, 1994). More recently, Bindiganavile and Banthia (Bindiganavile and Banthia, 2009) studied the effect of lightweight aggregates on shotcrete production and the present authors examined thermal properties for shotcrete mixes containing expanded perlite (Liu et al., 2011). Coupled process of shotcrete as a mechanical support and as thermal insulation can now be maturely simulated by the continuum method, finite element method (FEM), and FEM is currently the mainstream numerical tool in rock engineering, because of its benefits and maturity in processing the non-linearity and non-homogeneity of rock mass, the complexity of opening geometry, rock/structure interaction and the

tunnelling method (Jing, 2003, Jing and Hudson, 2002, Liu et al., 2008). In order to study the comprehensive behaviour of shotcrete in both aspects, FEM software ABAQUS[®] was chosen to establish the numerical models (DSIMULIA, 2004).

4.2 One-dimensional slab model

The one dimensional slab model (Sukhatme, 2011b) describes heat conduction through isotropic solid materials such as rock mass and shotcrete. The fundamental governing equation is given below:

$$\frac{\partial^2 T}{\partial x^2} = \frac{1}{\alpha} \frac{\partial T}{\partial t} \quad (4.1)$$

As shown in Figure 4-1(b), the right side of the boundary (outer boundary) in the rock mass is taken for practical purposes as infinite. Before ventilation and cooling, the initial temperature (T_0) of the whole model is the same as the virgin rock temperature (T_V), which is the temperature of the rock mass at certain depth before excavation. After cooling, the left boundary of rock mass (tunnel surface) is cooled by the air flow with temperature of air temperature (T_a), thus the heat flows from the high temperature rock mass towards the tunnel, developing into two different zones namely, the influenced zone and the virgin zone. The influenced zone is the area affected by the cooling process, whereas the virgin zone is the area where the temperature is kept constantly at the virgin rock

temperature (T_v). The distance between the tunnel surface to the interface of two zones is called heat penetration depth (D_p). These one-dimensional slab models are important to understand the heat transfer in the rock mass as well as in the thermal insulation. The description of these models is given in Table 4-1, in which the model names are defined in the following sections.

4.2.1 Heat flow through one-dimensional slab model with a semi-infinite boundary

4.2.1.1 Analytical models without insulation

For the model without insulation, the rock-air interface (tunnel wall surface) experiences three heat transfer processes at the same time namely, (i) conduction, (ii) convection and (iii) radiation. The *Dirichlet boundary condition* (Cheng and Cheng, 2005) is based on the assumption that the heat transfer coefficient is large enough to be considered as infinity, thus the temperature at the rock-air interface is maintained at the air temperature (T_a). Whereas, the *Neumann boundary condition* (Cheng and Cheng, 2005) is the more realistic case, solutions of this condition containing convection and radiation are also included in this study, by providing a heat transfer coefficient (h). The Equation (4.1) is transformed into a non-dimensional form in Equation (4.2) as follows:

$$\frac{\partial^2 \theta}{\partial \xi^2} = \frac{\partial \theta}{\partial Fo} \quad \text{for } \xi \in [0, \infty), Fo \in [0, \infty) \quad (4.2)$$

Initial condition:

$$\theta_0 = \theta(\zeta, 0) = 0 \quad (4.3)$$

$$\text{Boundary condition (1):} \quad \theta(\infty, Fo) = 0 \quad (4.4)$$

Boundary condition (2), two cases are discussed,

Model A in Dirichlet boundary condition:

$$\theta(0, Fo) = 1 \quad (4.5)$$

Model C in Neumann boundary condition:

$$\left. \frac{\partial \theta}{\partial \xi} \right|_{\xi=0} = -Bi[\theta(0, Fo) - 1] \quad \text{at } \zeta = 0 \quad (4.6)$$

Laplace transformation of the equations

Laplace transformation (Carslaw and Jaeger, 1959) was performed to solve

Equation (4.2), which yields

$$\frac{d^2 \bar{\theta}}{d\xi^2} = p\bar{\theta} - \theta_0 = p\bar{\theta} \quad \text{for } \zeta \in [0, \infty) \quad (4.7)$$

where $\theta_0 = 0$, as the initial condition;

a bar over function $\theta(\zeta, Fo)$ designates its Laplace transformation on Fo ,

$$\bar{\theta}(\xi, p) = \mathcal{L}\{\theta(\xi, Fo)\} = \int_0^\infty e^{-pFo} \theta dFo \quad (4.8)$$

where p is a number in the above integral, its real part, $Re(p)$, is always positive and large enough to ensure the convergence.

Applying the boundary conditions,

$$\text{Boundary condition (1) of (4.4) yields:} \quad \bar{\theta}(\infty) = 0 \quad (4.9)$$

Boundary condition (2) of (4.5) in Model A yields: $\bar{\theta}(0) = \frac{1}{p}$ (4.10)

Boundary condition (2) of (4.6) in Model C yields: $\frac{d\bar{\theta}}{d\xi} \Big|_{\xi=0} = -Bi[\bar{\theta}(0) - \frac{1}{p}]$ (4.11)

Solving, Model A, Equation (4.7) which satisfies *boundary condition (1)* of Equation (4.9) and *boundary condition (2)* of Equation (4.10) is,

$$\bar{\theta} = \frac{1}{p} e^{-\sqrt{p}\xi} \quad (4.12)$$

Then applying the inverse Laplace transformation, we obtain

$$\theta(\xi, Fo) = \text{Erfc}\left(\frac{\xi}{2\sqrt{Fo}}\right) \quad (4.13)$$

where *Erfc* is the complementary error function (Gautschi, 1992);

Incidentally, Equation (4.13) is also accomplished and verified by the *Method of Similarity* (Sukhatme, 2011b).

For Model C, Equation (4.7) which satisfies *boundary condition (1)* of Equation (4.9) and *boundary condition (2)* of Equation (4.11) yields:

$$\bar{\theta} = \frac{Bi}{(Bi + \sqrt{p})p} e^{-\sqrt{p}\xi} \quad (4.14)$$

Performing the inverse Laplace transformation with respect to the Table of Laplace transforms (Carslaw and Jaeger, 1959), we obtain:

$$\theta(\xi, Fo) = \text{Erfc}\left(\frac{\xi}{2\sqrt{Fo}}\right) - e^{(Bi\xi + Bi^2 Fo)} \text{Erfc}\left(\frac{\xi}{2\sqrt{Fo}} + Bi\sqrt{Fo}\right) \quad (4.15)$$

Equation (4.15) is also similar to the solution given by Sukhatme (Sukhatme, 2011b).

4.2.1.2 Analytical models with insulation of shotcrete

This model considers an insulating shotcrete layer and the semi-infinite rock mass. It is simplified into a one-dimensional composite slab problem, with one layer of the slab i.e. the rock mass, being semi-infinite. For $-\delta < x < 0$, the material is considered as the shotcrete layer, and for $x > 0$, it is taken as the rock mass. As previously mentioned both the *Dirichlet* and the *Neumann boundary conditions* are also listed here individually, to understand the insulation effects better. The dimensionless governing equations and the corresponding conditions have the following forms:

$$\frac{\partial^2 \theta_1}{\partial \xi^2} = \lambda \frac{\partial \theta_1}{\partial Fo} \quad \text{for } \zeta \in [-1, 0], \quad Fo \in [0, \infty) \quad (4.16)$$

$$\frac{\partial^2 \theta_2}{\partial \xi^2} = \frac{\partial \theta_2}{\partial Fo} \quad \text{for } \zeta \in [0, \infty), \quad Fo \in [0, \infty) \quad (4.17)$$

where $Fo = \frac{\alpha_2 t}{\delta^2}$, $\lambda = \frac{\alpha_2}{\alpha_1}$, the subscript "1" means shotcrete layer, "2" means rock;

Initial condition:

$$\theta_0 = \theta_1(\zeta, 0) = \theta_2(\zeta, 0) = 0 \quad (4.18)$$

It was assumed that the thermal contact resistance was negligible at the interface between the shotcrete layer and the rock mass. Thus, the *boundary conditions* at $x = 0$ are:

Boundary condition (1):

$$\theta_1(0, Fo) = \theta_2(0, Fo), \text{ at } \zeta = 0, \text{ based on continuity of temperature} \quad (4.19)$$

Boundary condition (2):

$$k_1 \frac{\partial \theta_1}{\partial \xi} \Big|_{\xi=0} = k_2 \frac{\partial \theta_2}{\partial \xi} \Big|_{\xi=0} , \text{ at } \zeta = 0, \text{ based on conservation of energy} \quad (4.20)$$

$$\text{Boundary condition (3): } \theta_2(\infty, Fo) = 0 \quad (4.21)$$

Boundary condition (4):

$$\text{Model B in Dirichlet boundary condition: } \theta_1(-1, Fo) = 1 \quad (4.22)$$

Model D in Neumann boundary condition:

$$\frac{\partial \theta_1}{\partial \xi} \Big|_{\xi=-1} = -Bi[\theta_1(-1, Fo) - 1] \quad \text{at} \quad \zeta = -1 \quad (4.23)$$

where $Bi = \frac{h\delta}{k_1}$

Laplace transformation was conducted on the governing Equation (4.16) and

Equation (4.17), to get

$$\frac{d^2 \bar{\theta}_1}{d\xi^2} = \lambda(p\bar{\theta}_1 - \theta_0) = \lambda p\bar{\theta}_1 \quad \text{for } \zeta \in [-1, 0], \quad Fo \in [0, \infty) \quad (4.24)$$

$$\frac{d^2 \bar{\theta}_2}{d\xi^2} = p\bar{\theta}_2 - \theta_0 = p\bar{\theta}_2 \quad \text{for } \zeta \in [0, \infty), \quad Fo \in [0, \infty) \quad (4.25)$$

Transforming corresponding *boundary conditions* from (4.19) to (4.25), to

$$\text{Boundary condition (1): } \bar{\theta}_1(0) = \bar{\theta}_2(0) \quad (4.26)$$

$$\text{Boundary condition (2): } k_1 \frac{\partial \bar{\theta}_1}{\partial \xi} \Big|_{\xi=0} = k_2 \frac{\partial \bar{\theta}_2}{\partial \xi} \Big|_{\xi=0} \quad (4.27)$$

$$\text{Boundary condition (3): } \bar{\theta}_2(\infty) = 0 \quad (4.28)$$

Boundary condition (4):

$$\text{Model B, } \bar{\theta}_1(-1) = \frac{1}{p} \quad (4.29)$$

$$\text{Model D, } \frac{d\bar{\theta}_1}{d\xi} \Big|_{\xi=-1} = -Bi[\bar{\theta}_1(-1) - \frac{1}{p}] \quad (4.30)$$

Solutions to the above are listed below:

For Model B, Equation (4.24) and Equation (4.25) which satisfy *boundary condition* (1), (2), (3) of Equations from (4.26) to (4.28) and *boundary condition* (4) of Equation (4.29) are,

$$\bar{\theta}_1 = \frac{k_1\sqrt{\lambda}\cosh(\xi\sqrt{p\lambda}) - k_2\sinh(\xi\sqrt{p\lambda})}{k_2p\sinh(\sqrt{p\lambda}) + k_1p\sqrt{\lambda}\cosh(\sqrt{p\lambda})} \quad (4.31)$$

$$\bar{\theta}_2 = \frac{k_1\sqrt{\lambda}e^{-\sqrt{p}\xi}}{k_2p\sinh(\sqrt{p\lambda}) + k_1p\sqrt{\lambda}\cosh(\sqrt{p\lambda})} \quad (4.32)$$

For Model D, Equation (4.24) and Equation (4.25) which satisfy *boundary condition* (1), (2), (3) of Equations from (4.26) to (4.28) and *boundary condition* (4) of Equation (4.30) are,

$$\bar{\theta}_1 = \frac{\text{Bi}k_2\sinh(\xi\sqrt{p\lambda}) - \text{Bi}k_1\sqrt{\lambda}\cosh(\xi\sqrt{p\lambda})}{p\sinh(\sqrt{p\lambda})(k_1\sqrt{p\lambda} - \text{Bi}k_2) + p\sqrt{\lambda}(k_2\sqrt{p} - \text{Bi}k_1)\cosh(\sqrt{p\lambda})} \quad (4.33)$$

$$\bar{\theta}_2 = \frac{\text{Bi}k_1\sqrt{\lambda}e^{-\sqrt{p}\xi}}{p(\sinh(\sqrt{p\lambda})(\text{Bi}k_2 - k_1\sqrt{p\lambda}) + \sqrt{\lambda}(\text{Bi}k_1 - k_2\sqrt{p})\cosh(\sqrt{p\lambda}))} \quad (4.34)$$

The inverse Laplace transformations of Equations from (4.31) to (4.34) were to be done. Since it is found that the transformation results in some cases could not be directly taken from transformation tables, the *Mellin's Inverse Formula*, also called the *Bromwich Integral* (Carslaw and Jaeger, 1959, Ramm, 1986) was applied to those cases to get corresponding results .

$$\theta(\xi, Fo) = \mathcal{L}^{-1}\{\bar{\theta}(\xi, p)\} = \frac{1}{2\pi i} \int_{c-i\infty}^{c+i\infty} e^{pFo} \bar{\theta}(\xi, p) dp \quad (4.35)$$

where c is the real part of p , $c = \text{Re}(p)$;

Unfortunately, even with the help of the inverse Laplace transformation function of *MATLAB*[®] (Guide, 1998) and *Mathematica*[®] (Wolfram, 1999), analytical

expressions to the solutions could not be obtained directly. However, many existing numerical algorithms, like *Durbin*, *Stehfest*, *Crump*, *Weeks and Piessens* (Crump, 1976, Durbin, 1974, Piessens, 1971, Stehfest, 1970, Weeks, 1966), are able to yield a reliable precision. Davies and Martin (Davies and Martin, 1979) have made comparisons of 16 different numerical methods for inverse Laplace transformation, it was concluded that the *Stehfest* algorithm (Stehfest, 1970) is fast and statistical reliable, with an average execution time of 0.043 s, and with low root-mean-square deviation between exact and numerical solutions. Sutradhar *et al.* (Sutradhar et al., 2002) and Moridis (Moridis, 1992) have also mentioned that the *Stehfest* algorithm is a very accurate method, which can overcome the possible problems of error magnification during inverse transformation found in some other algorithms. Thus, in this paper, the *Stehfest* algorithm is adopted to do the numerical inverse Laplace transformations for complicated expressions.

The *Stehfest* algorithm is given as follows,

$$\theta(fo) = \frac{\ln 2}{fo} \sum_{n=1}^N K_i \bar{\theta} \left(\frac{\ln 2}{fo} n \right) \quad (4.36)$$

where

$$K_i = (-1)^{\binom{N}{2}+n} \sum_{m=(n+1)/2}^{\min(n, N/2)} \frac{m^{N/2}(2m)!}{(N/2-m)!m!(m-1)!(n-m)!(2m-n)!} \quad (4.37)$$

Equation (4.36) and (4.37) have been used in *Mathematica*[®] (Wolfram, 1999), as a loaded package, to solve this problem, where N is an artificial number, which is set to be 16 in the applied algorithm.

4.2.2 Analysis of heat flow through one-dimensional slab model with a finite length boundary

4.2.2.1 Analytical models

4.2.2.1.1 Model E

Separation of Variables Method is the classical method for transient heat conduction problems with finite length boundary. Hence, an analytical solution of Model E was obtained by this *Separation of Variables Method*, using Sturm-Liouville equation comparison, and orthogonality application (Sukhatme, 2011a), the dimensionless expression was obtained as:

$$\theta(\xi, Fo) = -\left(\frac{\delta}{L}\right)\xi - \sum_{n=1}^{\infty} \frac{2}{n\pi} \exp\left[-\left(\frac{n\delta\pi}{L}\right)^2 Fo\right] \sin\left(\frac{n\delta\pi}{L}\xi\right) + 1 \quad (4.38)$$

4.2.2.1.2 Model F

Model F in dimensionless form is after previous solutions (Carslaw and Jaeger, 1959). Here, $-\delta < x < 0$ represents the shotcrete layer, and $0 < x < L$ indicates the rock mass layer.

$$\theta_1 = \frac{k_1 L - k_2 \delta \xi}{k_1 L + k_2 \delta} - 2 \sum_{n=1}^{\infty} \frac{[\cos(\delta \xi \beta_n) \sin(L K_s \beta_n) - K_e \sin(\delta \xi \beta_n) \cos(L K_s \beta_n)] e^{-\delta^2 K_s^2 \beta_n^2 Fo}}{\beta_n [(L K_e K_s + \delta) \sin(\delta \beta_n) \sin(L K_s \beta_n) - (L K_s + \delta K_e) \cos(\delta \beta_n) \cos(L K_s \beta_n)]} \quad (4.39)$$

$$\theta_2 = \frac{k_1(L - \delta \xi)}{k_1 L + k_2 \delta} - 2 \sum_{n=1}^{\infty} \frac{\sin(K_s \beta_n)(L - \delta \xi) e^{-\delta^2 K_s^2 \beta_n^2 Fo}}{\beta_n [(L K_e K_s + \delta) \sin(\delta \beta_n) \sin(L K_s \beta_n) - (L K_s + \delta K_e) \cos(\delta \beta_n) \cos(L K_s \beta_n)]} \quad (4.40)$$

$$\cos(\beta_n \delta) \sin(K_s \beta_n L) + K_e \sin(\beta_n \delta) \cos(K_s \beta_n L) = 0 \quad (4.41)$$

where $K_s = \sqrt{\frac{\alpha_1}{\alpha_2}}$, $K_e = \frac{k_2 K_s}{k_1}$, $Fo = \frac{\alpha_2 t}{\delta^2}$; $\beta_1 < \beta_2 < \dots < \beta_n < \dots$ (n = 1, 2,

3...)

Solution to Equation (4.41) which is a transcendental equation, known as the *Characteristic Equation*, gives roots, β_n , also known as eigenvalues, which are real, distinct, infinite and non-zero. Therefore, each β_n can give corresponding solutions for Equations (4.39) and (4.40), which were found to converge after a certain number of eigenvalues.

4.2.2.2 Numerical models

Numerical Models G, H, I, J were established with the help of ABAQUS[®] software, which is capable of simulating thermal behaviour in solids. These numerical models were all considered to be one dimensional with finite length boundary. For these models, mesh elements can be an influencing factor for the results, normally, smaller sizes of elements can give more precise results, but with more executing time.

4.2.3 Equivalent overall heat transfer coefficient model

Since the thickness of insulation is relatively very small in comparison with that of rock mass, it was assumed that the insulation layer can reach a steady-state throughout the thickness rapidly. The application of one insulation layer gives us an equivalent overall heat transfer coefficient (h_{eff}), which is from the steady-state solution. Thus the heat flux is equal to,

$$q_s = h_{eff}(T_s - T_a) \quad (4.42)$$

This would reduce the complicated two layers' problem into one layer problem with an equivalent heat transfer coefficient. Due to different steady-state solutions, it has to be formulated in both the slab model and cylindrical model, individually.

4.2.3.1 Slab model

In slab model, the equivalent overall heat transfer coefficient (h_{eff}) from the straightforward steady-state solution is,

$$h_{eff} = \frac{1}{\frac{1}{h} + \frac{\delta}{k_1}} \quad (4.43)$$

4.2.3.2 Cylindrical model

For the insulation layer in cylindrical coordinate system, the steady-state solution can also be easily achieved, and then the equivalent overall heat transfer coefficient is obtained as follows,

$$h_{eff} = \frac{1}{\frac{1}{h} + \frac{r_o \ln(r_{in}/r_o)}{k_1}} \quad (4.44)$$

4.3 Discussion

4.3.1 Parameters used in analysis

4.3.1.1 Input parameters

The selected slab model for practical calculations consists of two materials, namely, rock and insulation shotcrete. Rock thermal properties are after Bottomley (Bottomley, 1985), and insulation shotcrete's data is fetched from

previous studies (Liu et al., 2011). Mine environmental conditions are assumed based on Pickering and Tuck (Pickering and Tuck, 1997, Tuck, 1997). These input parameters used in models are given in Table 4-2.

4.3.1.2 Output parameters

4.3.1.2.1 Heat flux through surface

For the ‘no insulation’ models, the surface heat flux is from the rock mass to the atmosphere air, and is given as:

$$q_s = k \frac{\partial T}{\partial x} \Big|_{x=0} = \frac{k(T_a - T_V)}{\delta} \frac{\partial \theta}{\partial \xi} \Big|_{\xi=0} \quad (4.45)$$

For models that include insulations, the surface heat flux is from the rock mass to the insulation layer, then to the atmosphere air and is expressed as:

$$q_s = k_1 \frac{\partial T_1}{\partial x} \Big|_{x=-\delta} = \frac{k_1(T_a - T_V)}{\delta} \frac{\partial \theta}{\partial \xi} \Big|_{\xi=-1} \quad (4.46)$$

4.3.1.2.2 Average heat flux through surface

$$\bar{q}_s = \frac{1}{\tau} Q_s = \frac{1}{\tau} \int_0^\tau q_s dt \quad (4.47)$$

where Q_s (J/m^2) is the total accumulated heat flow through surface, τ is the ending time to calculate the total heat flow.

4.3.2 Comparisons of models

The links and differences between different models in Table 4-1 were studied to verify the reliability of predictions.

4.3.2.1 Comparison between models A, E and G

Model A, Model E and Model G were compared from different aspects. Figure 4-2, Figure 4-3 and Figure 4-4 demonstrate the relationships between these three models. As shown in Figure 4-2, the temperature profiles with respect to the distance from wall surface at the end of time of 1 year were predicted in Model A, Model E and Model G, respectively. It is found that Model A and Model E, both of which were analytical solutions, gave extremely similar temperature results. Results of Model G, which was a numerical model, also coincided fairly well with that of Model A and Model E's combined curve. Only a minor temperature difference, which was less than 1 K between the curves, was noticed. It is interesting to mention that these curves tend to become flat from a certain location, corresponding to the heat penetration depth (D_p). From Model A, this heat penetration depth can be easily calculated, by just letting $\theta = 0$, and referring to the properties of the *Error Function* (Gautschi, 1992), we can get the following expression:

$$D_p(t) = 6\sqrt{\alpha t} \quad (4.48)$$

Figure 4-3 describes the surface heat flux with time in these three models. It is seen that the values relating to all three models from the starting time to the ending time of 1 year, matched pretty well with no noticeable difference. Also, after magnification within a smaller range of time, similar findings were obtained

like Figure 4-2. Model A and Model E were totally identical and differed only slightly from Model G, which gave lower heat flux values. Further, Figure 4-4 is a plot of location versus temperature for the cases of Models A, E and G to show that all these models gave very similar values in Figure 4-2 and 4-3. Though, in the case of Model G, there was a slight difference but that was negligible. Both Model E and Model G have finite outer boundaries, which were taken as 60 m in Table 4-2. Theoretically, the finite outer boundary has to be larger than the heat penetration depth (D_p), which was approximately 50 m, estimated from Equation (4.48). To confirm this, Figure 4-5 is plotted. This figure indicates that if the outer boundary length is smaller than the heat penetration depth (D_p), then results of Model E or Model G would no longer be the same as Model A.

From the above comparisons, it can therefore be said that Model E and Model G can fully represent Model A, only as long as the outer boundary length is larger than the corresponding heat penetration depth (D_p). This significant point provides us the evidence and conditions to use finite boundary length models for describing semi-infinite boundary problems. Further, for this reason, all models here with semi-infinite boundaries can be assigned the thickness of 60 m with enough confidence.

4.3.2.2 Comparative analysis of Models B, F and H

In this part, one more insulation shotcrete layer was introduced into the models to be discussed, Models B, F, H were all bearing the *Dirichlet boundary condition* on the left boundary of the wall surface, referring to Figure 4-1(b). It is meaningful to mention that Model F has some difficulties to be implemented due to the existence of the transcendental Equation (4.41). Fortunately, graphical representation shown in Figure 4-6 can be plotted to obtain eigenvalues within a certain range by simply making a function $f(\beta)$ to be equal to Equation (4.41):

$$f(\beta) = \text{Cos}(\beta\delta)\text{Sin}(K_s\beta L) + K_e \text{Sin}(\beta\delta)\text{Cos}(K_s\beta L) \quad (4.49)$$

As seen in Figure 4-6, the intersection points between the function $f(\beta)$ and the β -axis, which are the eigenvalues, can be extracted accurately by using *Mathematica*[®]. Since the number of eigenvalues is infinity, only a certain range of numbers can be reached due to the limitation of computer volume. Briefly, the first 22 eigenvalues ($n = 1, 2, \dots, 22$) obtained within the β -axis from 0 to 3, are listed in Table 4-3. Further summations were also done by taking more eigenvalues, i.e., 145 eigenvalues ($n = 1, 2, \dots, 145$) and 343 eigenvalues ($n = 1, 2, \dots, 343$), which were named as Model F($n=145$) and Model F($n=343$), separately.

Interface temperature (T_{in}) is an important parameter to be considered for thermal insulation, because the adhesion of the insulation layer would primarily be influenced by this temperature. From Figure 4-7(a), it can be seen that the

interface temperature (T_{in}) between the insulation shotcrete layer and the rock mass dropped significantly from the initial temperature of 323 K to 308 K within a short time, that is in about 2.5×10^6 s (about 1 month). Thereafter, it decreased very slowly to 305 K until the end of 1 year (3.15×10^7 s); it is also found that the prediction in Model H was a little greater than that in other models, but here also the trend was similar. Figure 4-7(b), which is the enlarged figure as circled in Figure 4-7(a), concentrates specifically for small time scales, say, from 0 to 6000 s. All models in Figure 4-7(b) matched fairly well with the exception of Model F (n=22), in which case, a lower temperature of about 316.5 K was noticed. This has proved that taking only a few terms of the eigenvalue series could result in errors for small time scales.

Surface heat flux is another essential parameter to be assessed for the insulation, surface heat flux in Models B, F, and H were compared in Figure 4-8, and Figure 4-8(a) showed a nice match for these models, it is important to pay attention to Figure 4-8(b), which is an enlarged figure in small time scales. These figures demonstrate that Model H gave a distinctive curve for heat flux, which was smaller than that in other models, and there is an increasing trend at the very beginning from 0 to about 3.0×10^4 s (about 1/3 day). Model F with only 22 eigenvalues (n=22) was different from the other Model Fs where more eigenvalues are taken, and with the Model B shown in Figure 4-7. Figure 4-8(c)

illustrates the clear relationships of models from short term of 1.0×10^7 s (about 5 months) to long term of 3.15×10^7 s (1 year). The values from Model F(n=22), Model F(n=145), Model F(n=343), and Model B coincided with each other thus proving that the choice of the number of terms from the eigenvalue series did not have any significant difference in the results. Whereas, the results from Model H were somewhat larger than other models for large time scales, in comparison with that in small time scales.

It can be concluded from the preceding discussion that, finite Model F and Model H can represent well, Model B, the semi-infinite boundary of rock mass. According to the comparisons between them, there is a good matching between the interface temperature and surface heat flux; although a slight difference was found with respect to Model H. If the number of eigenvalues of Model F is small, the results in small time scales would be influenced, however it is also seen that the results in large time scales are not that sensitive to the choice of the number of eigenvalues to be taken. Even with 22 eigenvalues, results were still accurate enough for practical applications.

4.3.2.3 Comparative analysis of Models C with I and Models D with J

Models C, I, D and J are all with the *Neumann boundary condition* on the wall surface (the left boundary). As shown in Figure 4-9(a), the heat flux pattern was

similar in both Models C and I when the time elapsed was large. Whereas, for small time scales, as in Figure 4-9(b), the heat flux in Model I increased from 0 to 160, then started to get closer to the Model C curve. This goodness of fit can be clearly observed in the enlarged Figure 4-9(c). Thus Model I can represent Model C for large time conditions. Figure 4-10 shows the comparison between Models D and J. The surface heat flux in Model D was far larger than that in Model J, in small time condition, and a similar phenomenon is seen in Figure 4-9. Again, when the time lapsed was large enough, both the models showed similar trends. This is clearly seen in Figure 4-10. It can therefore be safely concluded that when the time frame is large the Models I and J, can very well replace the Models C and D, respectively.

4.3.3 Effects of thermal insulation in slab models

Since the surface heat flux (q_s) is prone to change with time, q_s at only one point of time cannot really reflect the effects of the thermal insulation over an elapsed period of time. Therefore, in this paper, the principle of average heat flux through the entire surface was adopted, as shown in Equation (4.47), which gave a better insight to the thermal insulation effects. Taking Model A for example, Figure 4-11(a) is a plot of the surface heat flux with time for this model, which is the area formed between the curve and the time-axis, or the integration in Equation (4.47), and is called accumulated heat flux (Q_s), as illustrated in Figure 4-11(b).

Based on their descriptions in Table 4-1, all the slab models were compared in the first 7 groups for the insulation effects as shown in Table 4-4. Table 4-4 shows that all these groups except Group 4, indicate a heat abatement of about 14% when shotcrete insulation is used. In Group 4, both Model G and Model H, with a *Dirichlet boundary condition* wall surface, were observed. Minor differences were seen between Models A, G and H on the one hand and between Models B, F and H on the other hand, in terms of the smaller heat flux values of Model G in Figure 4-3, whereas larger heat flux values of Model H as seen in Figure 4-8(c). This resulted in a cumulative effect and gave a much lower average heat flux abatement ratio of 3.56%, which definitely can be considered as an error as well. In other words, this analysis has also proved that, in numerical methods, errors may be small in individual models, but when a set of models are compared, any parametric error may be amplified many times. Needless to add, it is important to properly simulate theoretical models if the end results have to be sufficiently reliable for practical use.

In brief, the foregoing discussions have shown that insulation with shotcrete is an effective way to reduce the heat flux. Equally important, these comparative analyses give us the evidence that Model K, an equivalent overall heat transfer coefficient model, can predict the thermal insulation properties with great satisfaction when the interface temperature is negligible. Therefore, Model K is a

very practical and effective way to evaluate thermal insulation effects for applications in mine tunnels.

4.4 Effects of thermal insulation in cylindrical models

Compared to slab models, models with cylindrical geometry as shown in Figure 4-1(a) would be more similar to the shape of underground tunnels. In this study, based on the confidence gained from the insulation effects prediction in slab models, Model K was imposed on cylindrical models again.

4.4.1 Analytical cylindrical model without insulation

Similar to the input parameters in Table 4-2, in this model, which is designated as Model M, as shown in Figure 4-1(a), the radius of the tunnel opening is defined to be r_o and the rock mass region is for $r > r_o$. T_0 , the initial temperature, was kept at T_V throughout the rock, and at time t larger than 0 ($t > 0$), the inner wall surface is taken to be under *Neumann boundary condition* with an air flow temperature of T_a . The solution of this model is given as follows (Carslaw and Jaeger, 1959):

$$\theta(\xi, Fo) = \frac{2}{\pi} \int_0^{\infty} \frac{J_0(u\xi) \left[\left(\frac{u}{Bi} \right) Y_1(u) + Y_0(u) \right] - Y_0(u\xi) \left[\left(\frac{u}{Bi} \right) J_1(u) + J_0(u) \right]}{u \{ [(u/Bi)J_1(u) + J_0(u)]^2 + [(u/Bi)Y_1(u) + Y_0(u)]^2 \}} \cdot e^{-u^2 Fo} du + 1 \quad (4.50)$$

where $Fo = \frac{\alpha t}{r_o^2}$, $\xi = \frac{r}{r_o}$, $Bi = \frac{r_o h}{k}$; u is the variable for integration;

The surface heat flux patterns of Model M with 4 different tunnel diameters and those in Model C are given in Figure 4-12(a). On the same figure, the flux pattern

is plotted for Model C also. Figure 4-12 (b) shows an enlarged view of this. It is found that underground tunnels with smaller diameters would have higher surface heat flux, for a diameter $r_o = 2$ m, in Model M the heat flux was the highest. It is worthwhile to mention here that if the diameter of the tunnel increased the surface heat flux did not necessarily decrease proportionately. For instance, for a diameter of $r_o = 2 \times 10^9$ m, the surface heat flux did not decrease substantially. Instead, a limit would be reached in the heat flux reduction. As seen in Figure 4-12(b), the pattern of the flux in Model M for a diameter of ($r_o = 1 \times 10^9$ m or ∞), the curves approached that in Model C with both the curves practically coinciding. This can be easily understood from the geometry aspect of the cylindrical tunnel openings: As the tunnel diameter approaches infinity, the curvature approaches 0. In other words, it can be said that the cylinder model becomes a slab model when the radius approaches infinity and it has been shown that in that case the surface heat flux is the lowest.

4.4.2 Model K for cylindrical insulation

As for the insulation effects, Model K was used for a quick evaluation of thermal insulation on Model M. The 4 different tunnel diameters were marked as M-1, M-2, M-3 and M-4, respectively in Table 4-4, which listed the average heat flux reduction for each case. It was observed that the influence of insulation would be better in cylindrical models with a reduction of even 28.5% for a diameter of 2 m

when compared to the corresponding slab models. It is interesting to notice the identical results between Group 6 and Group 11, which has proved that slab models, are also basically a typical case of cylindrical models with insulation. We can also say that the results from cylindrical models show that they can provide a stronger theoretical approach for tackling the thermal insulation problems in underground tunnels.

4.5 Concluding remarks

Upon comparing the theoretical models related to thermal insulation for underground tunnels, several points can be made as follows:

1. For heat conduction problems in the infinite rock mass, finite length models can represent semi-infinite models, as long as the finite outer boundary length is larger than the heat penetration depth (D_p).
2. ABAQUS[®] can give relatively good results for simulation of thermal insulation in underground tunnels. Therefore, it can be considered as a reliable tool for analysing in case of larger scale projects with respect to heat related issues.
3. Equivalent overall Heat Transfer Coefficient Method, which was used as the empirical method here, has proven to be trustworthy. This method can predict the thermal insulation effects with satisfactory results, as long as the interface temperature (T_{in}) is not concerned in the analysis.

4. Thermal insulation with shotcrete is an effective way to reduce surface heat flux over 14 % average heat flux abatement can be achieved in slab models, while in case of cylindrical models the reduction can be even as high as 28.5% for a 2-m diameter tunnel.

This study therefore establishes theoretical justification for the use of thermal insulation in underground tunnels in mines.

Nomenclature in Chapter 4

D_p Heat penetration depth (m)

T Temperature (K)

T_0 Initial Temperature (K)

T_V Virgin rock temperature (K)

T_R Reference temperature (K)

T_a Air temperature (K)

T_s Tunnel surface temperature (K)

T_{in} Interface temperature (K)

x Space coordinate (m)

r Distance with respect to axis of cylindrical opening (m)

r_o Cylindrical opening radius (m)

δ Thickness of the insulation layer (m)

L Outer boundary length (m)

t Time (s)

τ Ending time (s)

k, k_1, k_2 Thermal conductivity (W / (m K))

C_p Specific heat capacity (J/(Kg K))

$\alpha, \alpha_1, \alpha_2$ Thermal diffusivity (m² / s)

λ Dimensionless parameter α_2 / α_1

K_s Expression for convenience: $K_s = \sqrt{\frac{\alpha_1}{\alpha_2}}$

K_e Expression for convenience: $K_e = \frac{k_2 K_s}{k_1}$

h Heat transfer coefficient (W / (m² K))

h_{eff} Equivalent overall heat transfer coefficient (W / (m² K))

θ Dimensionless temperature: $\theta = (T - T_V) / (T_a - T_V)$

ζ Dimensionless length: $\zeta = x / \delta$

Fo Dimensionless time, known as *Fourier number*, $Fo = (\alpha t) / \delta^2$

Bi Dimensionless heat transfer coefficient, known as *Biot number*,

$$Bi = (h \delta) / k$$

q_s Surface heat flux (W/m²)

Q_s Total accumulated heat flow through surface (J/m²)

\bar{q}_s Average surface heat flux (W/m²)

β Eigenvalues

p Parameter in Laplace transformation

$Re(p)$ Real part of p

Tables in Chapter 4

Table 4-1 Models descriptions

	Model	Method	Wall surface BC	Outer BC scale	Layers	Thermal application
	A	Analytical	<i>Dirichlet</i>	Semi-infinite	1	No insulation
	B	Analytical	<i>Dirichlet</i>	Semi-infinite	2	Insulation
	C	Analytical	<i>Neumann</i>	Semi-infinite	1	No insulation
	D	Analytical	<i>Neumann</i>	Semi-infinite	2	Insulation
Slab	E	Analytical	<i>Dirichlet</i>	Finite length	1	No insulation
	F	Analytical	<i>Dirichlet</i>	Finite length	2	Insulation
	G	Numerical	<i>Dirichlet</i>	Finite length	1	No insulation
	H	Numerical	<i>Dirichlet</i>	Finite length	2	Insulation
	I	Numerical	<i>Neumann</i>	Finite length	1	No insulation
	J	Numerical	<i>Neumann</i>	Finite length	2	Insulation
	K	Empirical	<i>Neumann</i>	Semi-infinite	2	Insulation
Cylinder	M	Analytical	<i>Neumann</i>	Semi-infinite	1	No insulation

where BC means *boundary condition*

Table 4-2 Input parameters

Parameters	Input values
Air temperature (T_a)	301.0 K
Virgin rock temperature (T_V)	323.0 K
Heat transfer coefficient (h)	10.0 W / (m ² K)
Thermal conductivity of shotcrete (k_I)	0.3799 W / (m K)
Density of shotcrete (ρ_I)	1169.1 kg/m ³
Specific heat capacity of shotcrete (C_{pI})	945.2 J / (kg K)
Thermal diffusivity of shotcrete (α_I)	3.438×10^{-7} m ² / s
Insulation shotcrete thickness (δ)	0.1 m
Thermal conductivity of rock (k_2)	6.00 W / (m K)
Density of rock (ρ_2)	2700.0 kg/m ³
Specific heat capacity of rock (C_{p2})	925.9 J / (kg K)
Thermal diffusivity of rock (α_2)	2.40×10^{-6} m ² / s
Outer boundary length for finite models (L)	60 m

Table 4-3 Eigenvalues of Model F

β_m	Value of β_m	β_m	Value of β_m	β_m	Value of β_m	β_m	Value of β_m
β_1	0.1348	β_6	0.8101	β_{12}	1.6259	β_{18}	2.4470
β_2	0.2696	β_7	0.9457	β_{13}	1.7625	β_{19}	2.5842
β_3	0.4046	β_8	1.0814	β_{14}	1.8991	β_{20}	2.7214
β_4	0.5396	β_9	1.2173	β_{15}	2.0359	β_{21}	2.8588
β_5	0.6748	β_{10}	1.3533	β_{16}	2.1728	β_{22}	2.9962
		β_{11}	1.4896	β_{17}	2.3099		

Table 4-4 Thermal insulation effects in different models at 1 year

Group	No insulation	Average heat flux (W/m ²)	Insulation	Average heat flux (W/m ²)	Abatement (W/m ²)	Abatement ratio
1	Model A	17.121	Model B	14.713	2.407	14.06%
2	Model C	16.115	Model D	13.783	2.331	14.47%
3	Model E	17.099	Model F	14.702	2.397	14.02%
4	Model G	16.149	Model H	15.574	0.575	3.56%
5	Model I	17.155	Model J	14.655	2.500	14.58%
6	Model C	16.115	Model K	13.841	2.273	14.11%
7	Model I	17.155	Model K	14.523	2.632	15.34%
8	Model M-1	34.967	Model K	25.016	9.950	28.46%
9	Model M-2	23.831	Model K	18.826	5.004	21.00%
10	Model M-3	21.048	Model K	17.102	3.946	18.75%
11	Model M-4	16.115	Model K	13.841	2.273	14.11%

Figures in Chapter 4

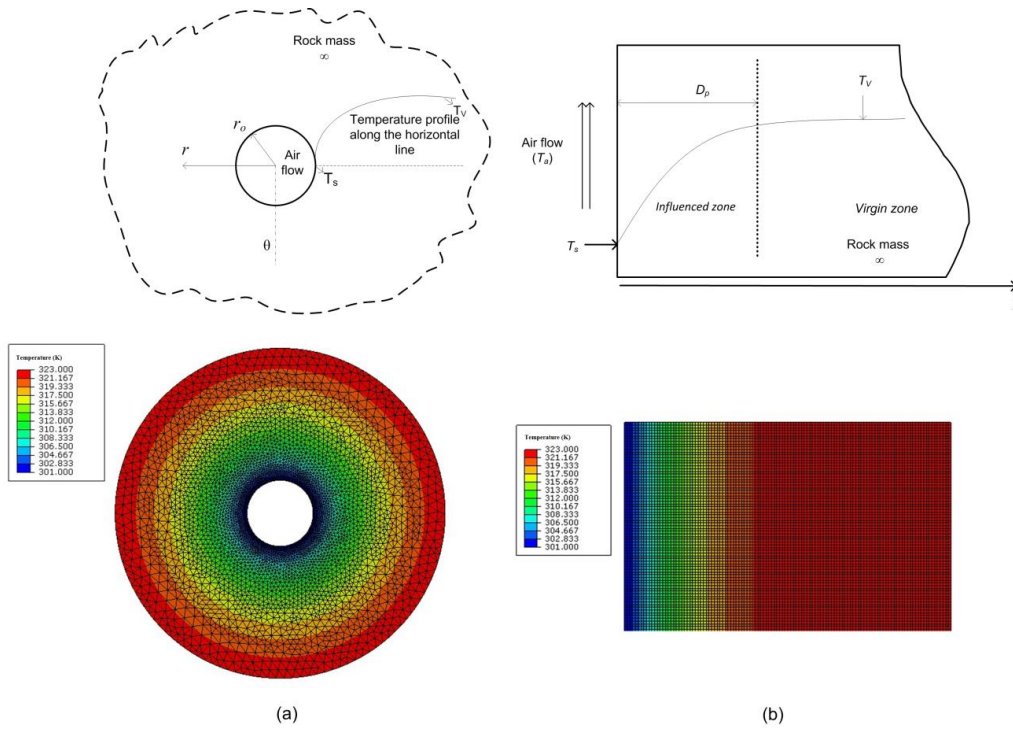


Figure 4-1 Schematic of underground temperature distribution

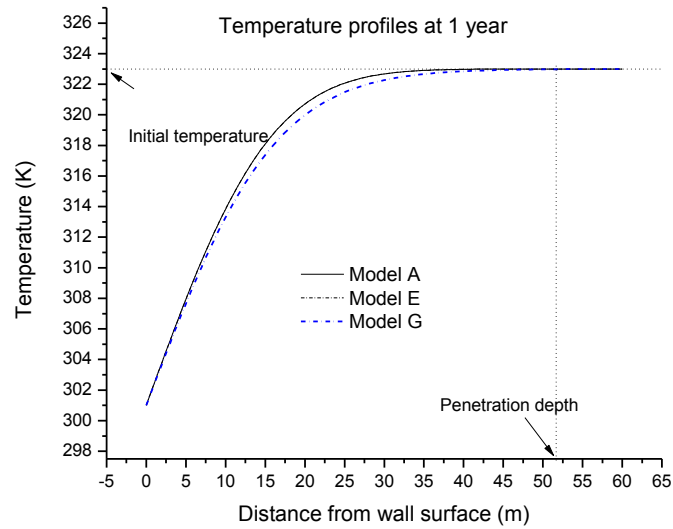


Figure 4-2 Temperature profiles of Model A, E and G at 1 year

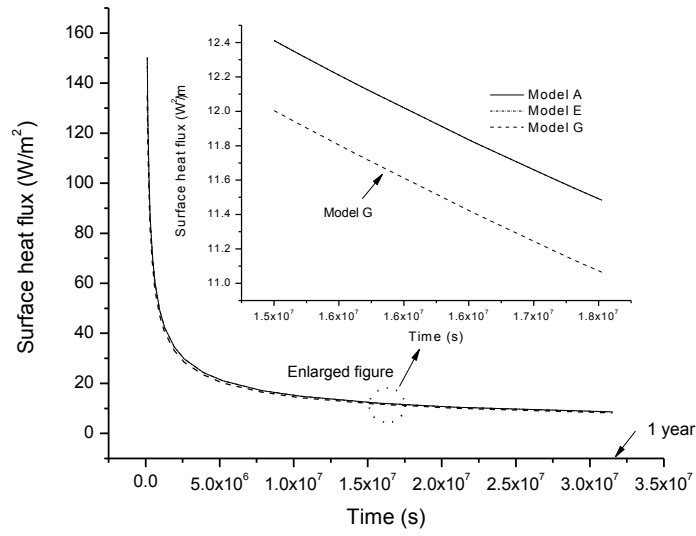


Figure 4-3 Surface heat fluxes of Model A, E and G with time

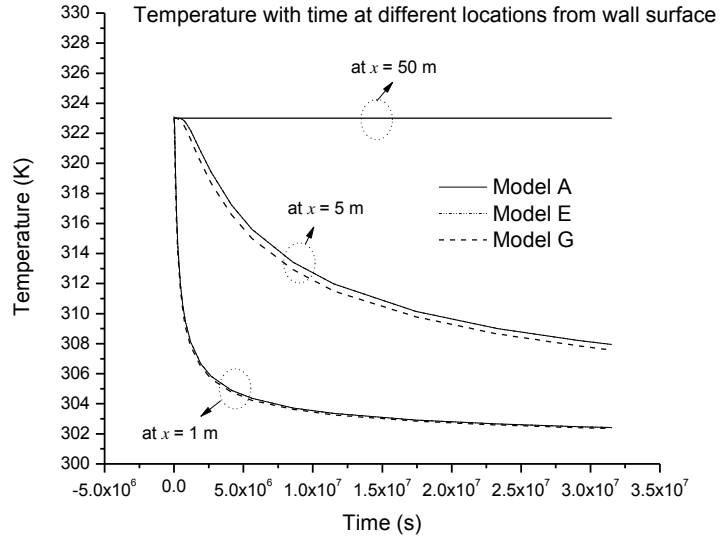


Figure 4-4 Temperature changes of Model A, E and G with time at different locations

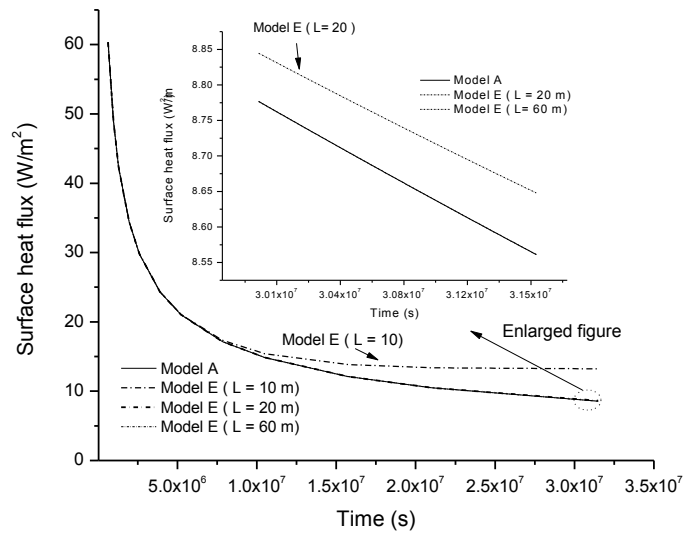


Figure 4-5 Sensitivity analysis of Model E's outer boundary length

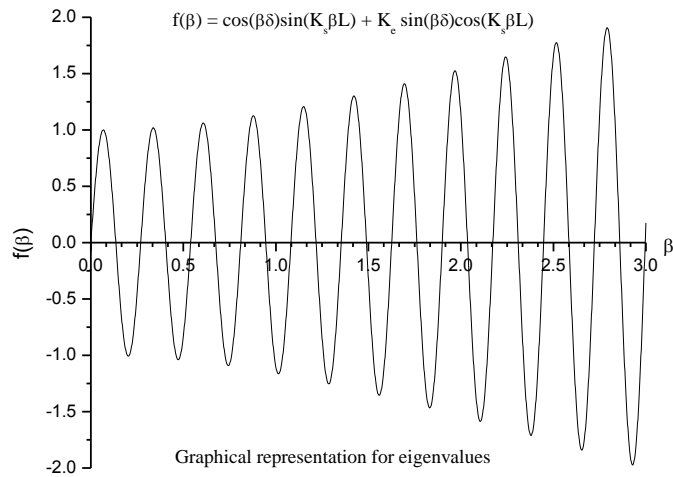


Figure 4-6 Eigenvalues

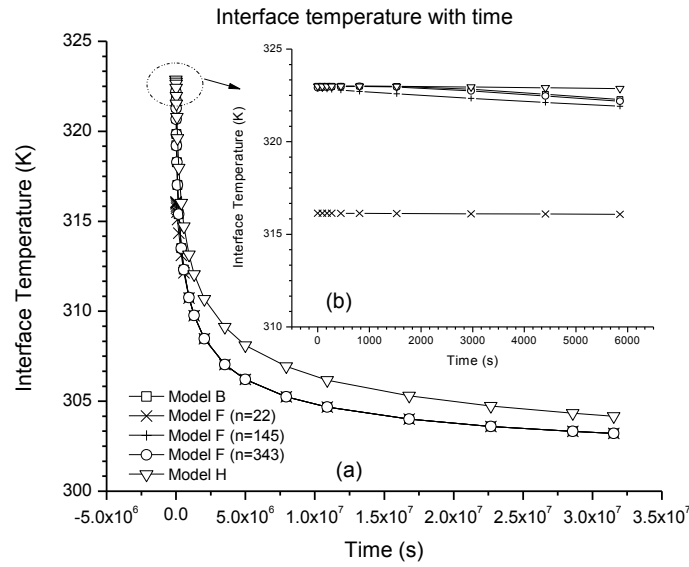


Figure 4-7 Interface temperatures of Model B, F and H with time

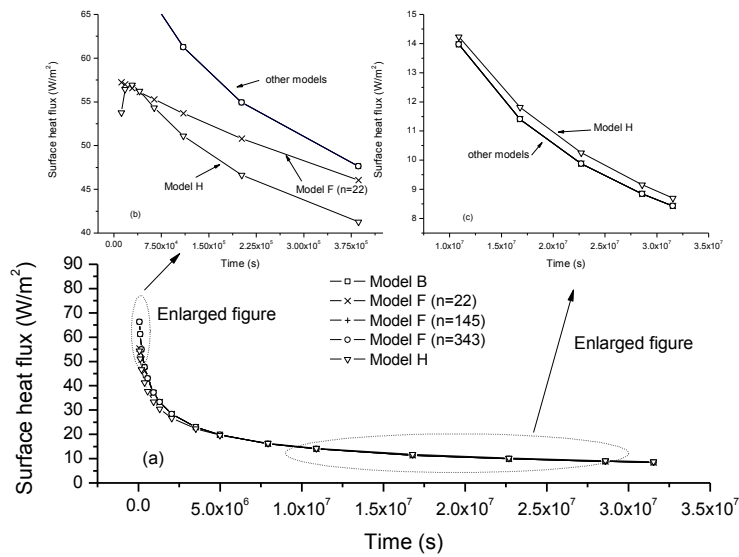


Figure 4-8 Surface heat fluxes of Model B, F, and H with time

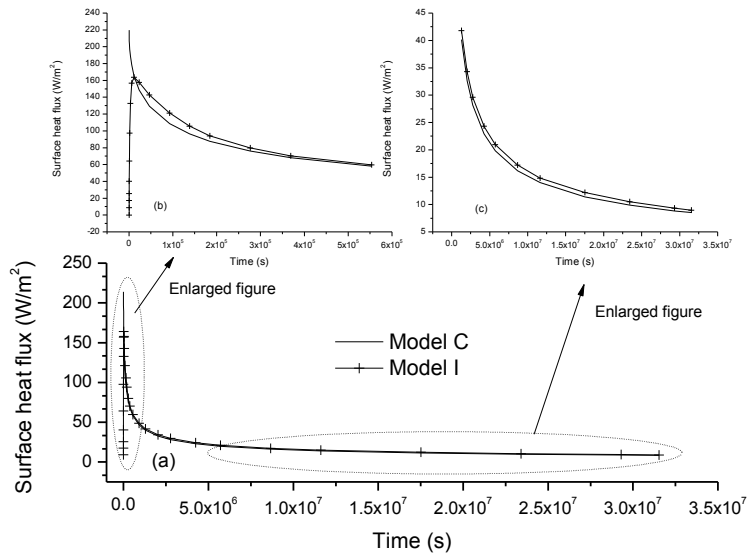


Figure 4-9 Surface heat fluxes of Model C and I with time

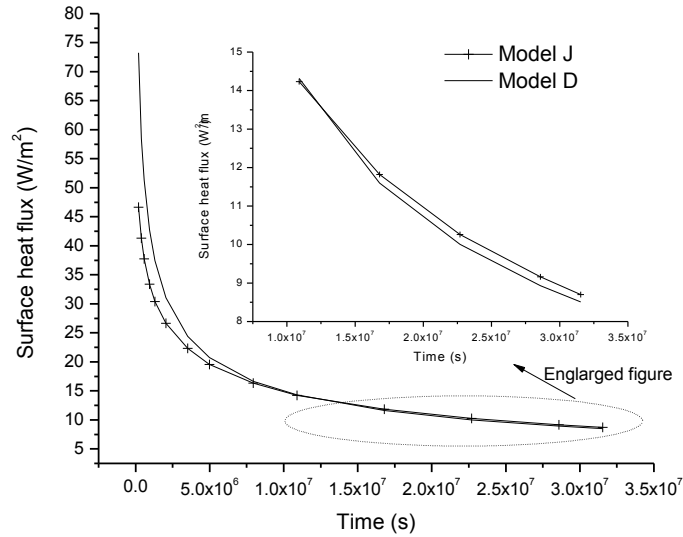


Figure 4-10 Surface heat fluxes of Model D and J with time

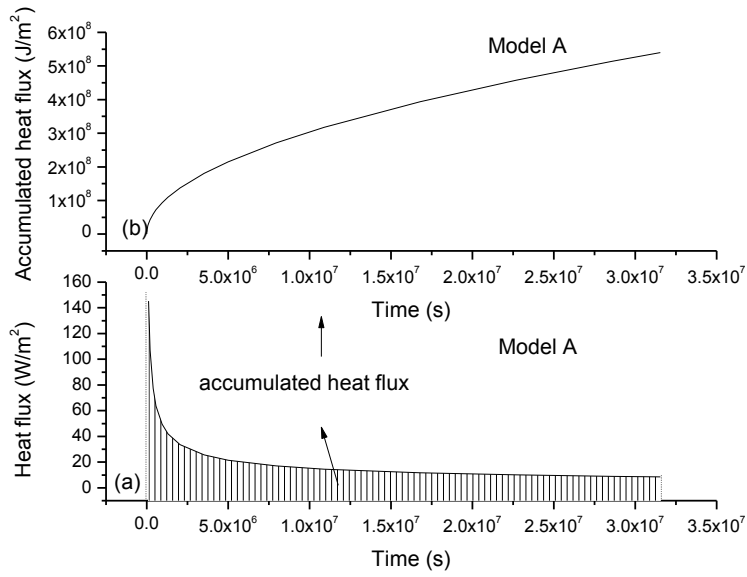


Figure 4-11 Integration for accumulated heat flux

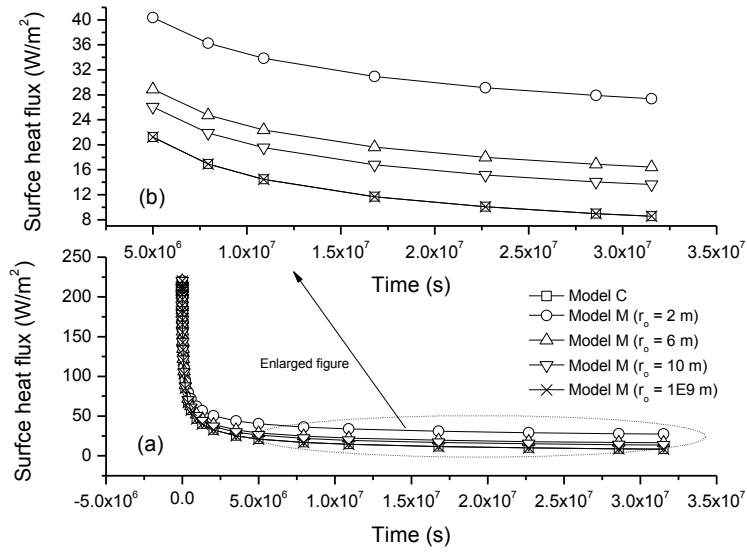


Figure 4-12 Surface heat fluxes of Model C and M with time

References

- Ashworth, E. (1992) Heat flow into underground openings: Significant factors. *Mining Engineering*. University of Arizona, USA.
- Bindiganavile, V. & Banthia, N. (2009) Effect of particle density on its rebound in dry-mix shotcrete. *Journal of Materials in Civil Engineering*, 21, 58.
- Bottomley, P. (1985) The reduction in heat flow due to the insulation of rock surfaces in mine airways. *2nd US Mine Ventilation Symposium*. Reno, NV.
- Carslaw, H. S. & Jaeger, J. C. (1959) *Conduction of heat in solids*, Oxford: Clarendon Press, 2nd ed.
- Chellam, S. (1992) Thermal insulation of underground mine workings at deep levels. *Department of Mining Engineering*. Rapid City, South Dakota, South Dakota School of Mines and Technology.
- Cheng, A. H. D. & Cheng, D. T. (2005) Heritage and early history of the boundary element method. *Engineering Analysis with Boundary Elements*, 29, 268-302.
- Crump, K. S. (1976) Numerical inversion of Laplace transforms using a Fourier series approximation. *Journal of the ACM (JACM)*, 23, 89-96.
- Davies, B. & Martin, B. (1979) Numerical inversion of the Laplace transform: a survey and comparison of methods. *Journal of computational physics*, 33, 1-32.
- de Monte, F. (2000) Transient heat conduction in one-dimensional composite slab. A natural analytic approach. *International Journal of Heat and Mass Transfer*, 43, 3607-3619.
- de Monte, F. (2006) Multi-layer transient heat conduction using transition time scales. *International Journal of Thermal Sciences*, 45, 882-892.
- DSIMULIA (2004) Heat Transfer and Thermal-Stress Analysis with Abaqus.
- Durbin, F. (1974) Numerical inversion of Laplace transforms: an efficient improvement to Dubner and Abate's method. *Computer Journal*, 17, 371-376.
- Gautschi, W. (1992) Error function and Fresnel integrals. *Handbook of Mathematical Functions with Formulas, Graphs, and Mathematical Tables*, M. Abramowitz and IA Stegun, eds., Dover Publications, Inc., New York, NY, 295-329.
- Guide, M. U. (1998) The MathWorks. Inc., Natick, MA, 5.
- Jing, L. (2003) A review of techniques, advances and outstanding issues in numerical modelling for rock mechanics and rock engineering. *International Journal of Rock Mechanics and Mining Sciences*, 40, 283-353.

- Jing, L. & Hudson, J. A. (2002) Numerical methods in rock mechanics. *International Journal of Rock Mechanics and Mining Sciences*, 39, 409-427.
- Liu , H. Y., Small, J. C. & Carter, J. P. (2008) Full 3D modelling for effects of tunnelling on existing support systems in the Sydney region. *Tunnelling and Underground Space Technology*, 23, 399-420.
- Liu, W. V., Apel, D. B. & Bindiganavile, V. (2011) Thermal characterisation of a lightweight mortar containing expanded perlite for underground insulation. *International Journal of Mining and Mineral Engineering*, 3, 55-71.
- Lu, X. & Tervola, P. (2005) Transient heat conduction in the composite slab-analytical method. *Journal of Physics A: Mathematical and General*, 38, 81.
- Moridis, G. (1992) Alternative formulations of the Laplace transform boundary element (LTBE) numerical method for the solution of diffusion-type equations. Berkeley ,California, United States, Lawrence Berkeley Lab., CA (United States).
- Pickering, A. J. & Tuck, M. (1997) Heat: sources, evaluation, determination of heat stress and heat stress treatment. *Mining Technology*, 79, 147-56.
- Piessens, R. (1971) Gaussian quadrature formulas for the numerical integration of Bromwich's integral and the inversion of the Laplace transform. *Journal of Engineering Mathematics*, 5, 1-9.
- Ramm, A. G. (1986) Inversion of the Laplace transform. *Inverse problems*, 2, L55.
- Rao, K. S., Sastry, B. S. & Misra, B. (1994) Planing for insulation of mine roadways for reduction of strata heat flow into air stream. *Mine Planning and Equipment Selection 1994*.
- Rawlins, C. A. & Phillips, H. R. (2001) Reduction of mine heat loads. *7th International Mine Ventilation Congress*. Krakow, Poland.
- Stehfest, H. (1970) Numerical inversion of Lapalce transforms. *Communications of the ACM*, 13, 47-49 and 624.
- Sukhatme, S. P. (2011a) Analysis of heat conduction and some steady one-dimensional problems. *A Text Book on Heat Transfer*. Cambridge, Massachusetts, Phlogiston Press.
- Sukhatme, S. P. (2011b) Transient and multidimensional heat conduction. *A Text Book on Heat Transfer*. Cambridge, Massachusetts, Phlogiston Press.
- Sun, Y. & Wichman, I. S. (2004) On transient heat conduction in a one-dimensional composite slab. *International Journal of Heat and Mass Transfer*, 47, 1555-1559.

- Sutradhar, A., Paulino, G. H. & Gray, L. J. (2002) Transient heat conduction in homogeneous and non-homogeneous materials by the Laplace transform Galerkin boundary element method. *Engineering Analysis with Boundary Elements*, 26, 119-132.
- Tuck, M. A. (1997) Control of mine climate. *Mining Technology*, 79, 215-220.
- USBM (1994) An 'insulating' shotcrete for heat abatement in deep mines. *Technology News* 434.
- Weeks, W. T. (1966) Numerical inversion of Laplace transforms using Laguerre functions. *Journal of the ACM (JACM)*, 13, 419-426.
- Wolfram, S. (1999) *The Mathematica book*, Cambridge University Press.

Chapter 5 Theoretical study on cylindrical models of heat flow and thermo-elastic stress in underground tunnels⁴

5.1 Introduction

As the demand for minerals is increasing the world over, the mining industry goes ever deeper into the belly of the Earth in order to extract them. The geothermal heat diffusing from the surrounding rock mass into these underground mine tunnels is proportional to the mining depth. In fact, this increase in the heat flow into the working face of the mine is very rapid as the depth of the mine increases (Hartman et al., 1998, Spalding, 1949). So much so, cost effective dissipation of heat and providing a safe working environment inside these tunnels is the major develop concern of all deep hot mines. One of the proposed methods of reducing the heat inside the tunnels is the application of insulation materials on the tunnel surface, imparting low thermal conductivity and thereby prevents geothermal heat migration from the infinite rock mass to the working areas inside (Bottomley, 1985, Howarth and Gillies, 1987, Wagner, 2010). Furthermore, it is also equally

⁴ The content of this Chapter has been prepared and submitted as a journal manuscript: Liu, W. V., Apel, D. B., Bindiganavile, V. S. & Szymanski, J. K. (2012) Theoretical study on cylindrical models of heat flow and thermo-elastic stress in underground tunnels. *Energy and Buildings* (submitted)

important that such an insulating layer acts as a structural support to the rock excavation.

The underground mine opening is, ideally considered to be cylindrical in shape and is surrounded by an infinite rock mass. As a result, geothermal heat emanating from the rock mass continues to flow into the cylindrical opening. As shown in Figure 5-1(a), after a certain time of ventilation and cooling, the rock surface of the tunnel initially at the virgin rock temperature (T_v), cools down to a lower tunnel surface temperature (T_s). However, it may be taken as virgin rock temperature (T_v) at a certain far enough distance inside the rock mass. This consequent ideal phenomenon may be considered mathematically, as a one-dimensional transient heat conduction problem in a cylindrical opening with an infinite, outer boundary. It is to be recognized that the temperature change causes thermal stresses inside the surrounding rock mass, which may even threaten the stability of the tunnel. Therefore, in order to choose a suitable insulation for the tunnel surfaces inside the rock mass, a reliable solution is to be found. Such a solution must necessarily account for the temperature field inside the rock mass and the temperature gradient, both of which are time-dependent.

The use of shotcrete as an insulating liner in tunnels was first proposed by the U.S Bureau of Mines in 1994 (USBM, 1994). It has been shown previously that lightweight aggregates the shotcreting process (Bindiganavile and Banthia, 2009)

and the present authors reported recently on the thermal properties of such mixes (Liu et al., 2011). In this paper, a detailed discussion on the theoretical evaluation of the heat flow problem into underground openings and the effect of thermal insulation as well as that of thermal stresses are presented. The study is grouped into two sections here, namely, the analytical analysis and the numerical analysis. The analytical analysis comes from the modified mathematical closed-form expressions (Carslaw and Jaeger, 1959, Gibson, 1976, Goch and Patterson, 1940, Starfield, 1969) for the specific problem as described above. And the numerical analysis originates from the finite element method (FEM) based ABAQUS[®] software (Abaqus Users Manual), as the FEM software lends itself suitable for studying shotcrete both as a rock support and as a thermal insulation (DSIMULIA, 2004, Jing, 2003, Jing and Hudson, 2002, Liu et al., 2008).

The objective of this study is to review and summarize previous mathematical closed-form expressions (Carslaw and Jaeger, 1959, Gibson, 1976, Goch and Patterson, 1940, Starfield, 1969), and by which to verify the reliability of numerical modelling in FEM software for thermal insulation on the infinite rock mass, in sequence, to assess the effects of using shotcrete for thermal insulation in applications.

5.2 One-dimensional cylindrical model

A deep underground excavation may be considered to be in the infinite or semi-infinite rock mass, because the area of underground opening is much too small compared to the earth and rock mass through which the opening is excavated. In this paper, a simplified model namely, a one-dimensional cylindrical model for the underground tunnel is discussed. Further, it is assumed that the temperature distribution does not vary with the z -direction, which represents the axis of the tunnel. Also, this distribution is assumed to be symmetrical with respect to the angle (θ) in the cylindrical coordinate system. As shown in Figure 5-1(a), in such a coordinate system (r, θ), the original tunnel radius is r_o , and the direction that is perpendicular to the plan view is the z -direction.

The governing equations of the heat conduction (Sukhatme, 2011) in the insulation shotcrete and rock mass, both of which are assumed as homogeneous and isotropic, is expressed in dimensionless form of Equation (5.1) and Equation (5.2) as follows:

$$\frac{1}{\xi} \frac{\partial}{\partial \xi} \left(\xi \frac{\partial \psi_1}{\partial \xi} \right) = \lambda \frac{\partial \psi_1}{\partial Fo} \quad \text{for } \frac{r_{in}}{r_o} < \xi < 1 \quad (5.1)$$

$$\frac{1}{\xi} \frac{\partial}{\partial \xi} \left(\xi \frac{\partial \psi_2}{\partial \xi} \right) = \frac{\partial \psi_2}{\partial Fo} \quad \text{for } 1 \leq \xi < \infty \quad (5.2)$$

where ξ is the dimensionless length: $\xi = r / r_o$; r is the radius from origin in coordinate system as shown in Figure 5-1; r_o is the radius (m) of the tunnel before

applying any shotcrete; r_{in} is the radius (m) of the tunnel after shotcreting; ψ is the dimensionless temperature: $\psi = (T - T_V) / (T_a - T_V)$; T is the temperature (K) in shotcrete or rock mass, it depends on the location and time; T_a is the temperature of atmosphere (K); T_V is the virgin rock temperature (K); Fo is the dimensionless time, known as *Fourier number*: $Fo = (\alpha_2 t) / r_o^2$; α_2 is thermal diffusivity (m^2 / s) of rock; t is the time (s); λ is the dimensionless parameter, $\lambda = \alpha_2 / \alpha_1$; α_1 is thermal diffusivity (m^2/s) of shotcrete; Besides, the subscript "1" indicates shotcrete insulation layer and "2" represents rock mass. These definitions apply to all the equations in this paper, details can also be found in *Nomenclature*.

When it comes to the tunnel without thermal insulation, only Equation (5.2) for rock mass is used for thermal analysis and the initial and boundary conditions have the following forms:

Initial condition

$$\psi_2(\xi, 0) = 0 \quad (5.3)$$

Boundary condition

$$\psi_2(\infty, Fo) = 0 \quad (5.4)$$

$$\frac{\partial \psi_2}{\partial \xi} \Big|_{\xi=1} = Bi[\psi_2(1, Fo) - 1] \quad (5.5)$$

where Bi is the dimensionless heat transfer coefficient, known as *Biot number*:

$Bi = (h r_o) / k_2$; k_2 is the thermal conductivity (W/(m K)) of rock.

In the following analysis, for the case of ‘no insulation’, subscript "2" gets eliminated for convenience, i.e. ψ_2 becomes simply, ψ .

5.2.1 Solutions for a cylindrical model with a semi-infinite boundary

Many researchers have derived the temperature results previously by solving Equation (5.2) (Carslaw and Jaeger, 1959, McPherson, 1986, Starfield, 1969) and here, they are discussed in the following sections.

5.2.1.1 Carslaw and Jaeger's solution

This analytical solution of the temperature field obtained by Carslaw and Jaeger (Carslaw and Jaeger, 1959), can be considered to be fairly classical and its dimensionless form is as follows:

$$\psi(\xi, Fo) = \frac{2}{\pi} \int_0^{\infty} \frac{J_0(u\xi) \left[\left(\frac{u}{Bi} \right) Y_1(u) + Y_0(u) \right] - Y_0(u\xi) \left[\left(\frac{u}{Bi} \right) J_1(u) + J_0(u) \right]}{u \{ [(u/Bi)J_1(u) + J_0(u)]^2 + [(u/Bi)Y_1(u) + Y_0(u)]^2 \}} \cdot e^{-u^2 Fo} du + 1 \quad (5.6)$$

where u is just the variable for integration, however without any physical meaning in the heat conduction problem; $Y_0(x)$, $Y_1(x)$, $J_0(x)$, $J_1(x)$ are *Bessel functions* with respect to x (McLachlan, 1955), as shown in Equation (5.6), the variable u and $(u \xi)$ are in *Bessel functions as "x"*.

Equation (5.6) itself imposed considerable difficulty on its application, due to the existence of integration and *Bessel functions*. However, it was solved by the

present authors for exact solutions, which were discussed in the following sections.

5.2.1.2 Gibson's solution

Gibson's solution (Gibson, 1976) as given by McPherson (McPherson, 1986) is utilised to predict the dimensionless temperature gradient at tunnel surface (G_s). Accordingly,

$$G_s = \frac{r_o}{T_V - T_a} \frac{\partial T(r,t)}{\partial r} \Big|_{r=r_o} = - \frac{\partial \psi(\xi, Fo)}{\partial \xi} \Big|_{\xi=1} \quad (5.7)$$

G_s , related to Fo and Bi , is determined by using a numerical algorithm (Gibson, 1976) in Appendix 5-1. Also, a dimensionless form of temperature on the tunnel surface is depicted from Equation (5.5) as follows,

$$\psi(1, Fo) = 1 - \frac{G_s}{Bi} \quad (5.8)$$

However, this method just has a limited application on the tunnel surface, instead of the descriptions of other locations in rock mass, because it only applies to $\xi = 1$, where it is the tunnel surface, as shown in Equation (5.8).

2.1.3 Starfield-Bleloch's solution

Starfield and Bleloch (Starfield and Bleloch, 1983) proposed a 'quasi-steady' method to estimate this cylindrical, semi-infinite, outer boundary problem, by defining a time dependant outer boundary R (Fo), which is also dimensionless depending on the *Fourier number* Fo . Therefore, according to this solution, the

transient heat transfer problem was simplified to be steady at a given moment with a specified dimensionless outer boundary R . From this perspective, Equation (5.2), (5.4) and (5.5) become very simple as the steady state. Therefore, eliminating parts which are related to Fo , the governing equation now becomes:

$$\frac{1}{\xi} \frac{\partial}{\partial \xi} \left(\xi \frac{\partial \psi}{\partial \xi} \right) = 0 \quad \text{for } 1 \leq \xi < R \quad (5.9)$$

For the two *boundary conditions* in steady state, the Equation (5.9) will take the following form:

$$\text{Boundary condition (1): } \psi(\xi = R) = 0 \quad (5.10)$$

$$\text{Boundary condition (2): } \frac{\partial \psi}{\partial \xi} \Big|_{\xi=1} = Bi[\psi(\xi = 1) - 1] \quad (5.11)$$

Governing Equation (5.9) is solved with two boundary conditions as in Equation (5.10) and (5.11), and yields the following:

$$\psi(\xi) = \frac{-BiLn(\xi/R)}{1+BiLn(R)} \quad (5.12)$$

A parameter, named as Goch-Patterson flux (G_p) (Goch and Patterson, 1940), was defined as in Equation (5.13),

$$G_p(Fo) = \frac{4}{\pi^2} \int_0^\infty \frac{e^{-Fo u^2}}{J_0^2(u) + Y_0^2(u)} \frac{du}{u} = \frac{1}{Ln(R)} \quad (5.13)$$

where u is again the variable for integration, same as that in Equation (5.6), besides, Y_0 and J_0 are *Bessel functions* (McLachlan, 1955).

Now, Equation (5.13) becomes the key component to be solved, once R is derived in Equation (5.13), dimensionless temperature ψ with ξ can be obtained immediately in Equation (5.12). Starfield and Bleloch (Starfield, 1969, Starfield

and Bleloch, 1983) found an algorithm to obtain the R in Equation (5.13), however only applicable in cases where Fo is larger than 1.5. In other words, Starfield and Bleloch's solutions cannot cover the early stages of tunnel development, that is for small time scales as when Fo is smaller than 1.5. In the present study, the current authors managed to solve Equation (5.13) for all time scales. Hence, Equation (5.12) can now be transformed, by using G_p in Equation (5.13). Therefore, the following Equation (5.14) becomes a new form of transient solutions, substituted by G_p , which is solely related to Fo :

$$\psi(\xi, Fo) = \psi(\xi) = \frac{Bi[1-G_p Ln(\xi)]}{G_p + Bi} \quad (5.14)$$

The results of Equation (5.14) are discussed later on, together with other solutions.

5.2.2 ABAQUS model with finite length boundary

The present authors adopted the ABAQUS[®] software, owing to its compatibility in describing both thermal and mechanical behaviour in solids. The heat transfer model was established with finite length boundary and input parameters were kept the same as that in the analytical models, as shown in Table 5-1.

5.2.3 Theory related to thermal stresses

Thermal stresses induced by temperature variations at different locations in the rock mass, is well interpreted by Timoshenko and Goodier (Timoshenko and Goodier, 1951) in general forms first, assuming that the material is only under

elastic deformation. These general forms are transformed into dimensionless forms as shown below,

$$u_{11} = \frac{u_r}{r_o} = \frac{1+\nu}{1-\nu} \frac{\alpha_e(T_a-T_V)}{\xi} \int_1^\xi \psi \xi d\xi + A_1 \xi + \frac{A_2}{\xi} \quad (5.15)$$

$$s_{11} = \frac{\sigma_r}{E} = -\frac{1}{1-\nu} \frac{\alpha_e(T_a-T_V)}{\xi^2} \int_1^\xi \psi \xi d\xi + \frac{1}{1+\nu} \left(\frac{A_1}{1-2\nu} - \frac{A_2}{\xi^2} \right) \quad (5.16)$$

$$s_{22} = \frac{\sigma_\theta}{E} = \frac{1}{1-\nu} \frac{\alpha_e(T_a-T_V)}{\xi^2} \int_1^\xi \psi \xi d\xi - \frac{\alpha_e(T_a-T_V)\psi}{1-\nu} + \frac{1}{1+\nu} \left(\frac{A_1}{1-2\nu} + \frac{A_2}{\xi^2} \right) \quad (5.17)$$

$$s_{33} = \frac{\sigma_z}{E} = -\frac{\alpha_e(T_a-T_V)\psi}{1-\nu} + \frac{2\nu A_1}{(1+\nu)(1-2\nu)} \quad (5.18)$$

where A_1 and A_2 are integration constants that have to be determined by *boundary conditions*; As shown in Figure 5-1, u_{11} is the dimensionless radial displacement: $u_{11} = u_r/r_o$; u_r is the radial displacement (m); r_o is the radius (m) of the tunnel; α_e is the linear coefficient of thermal expansion (1/K); s_{11} is the dimensionless radial stress: $s_{11} = \sigma_r/E$; σ_r is the radial stress (Pa); E is the Young's modulus (GPa); s_{22} is the dimensionless tangential stress: $s_{22} = \sigma_\theta/E$; σ_θ is the tangential stress (Pa); s_{33} is the dimensionless axial stress: $s_{33} = \sigma_z/E$; σ_z is the axial stress (Pa); ν is Poisson's ratio;

Kumar and Singh (Kumar and Singh, 1989) took the *boundary conditions* as the inner surface of the tunnel and the outer boundary of the rock mass at infinity, in order to obtain the specific solutions of thermal stresses in the case of underground tunnels surrounded by infinite rock mass. Thus for:

$$\text{Boundary condition (1): } s_{11} = \frac{\sigma_r}{E} = 0 \quad ; \text{ at } \xi = 1, \text{ inner surface of the tunnel;} \quad (5.19)$$

$$\text{Boundary condition (2): } s_{11} = \frac{\sigma_r}{E} = 0 \text{ ; at } \xi = \infty, \text{ far infinity of the rock mass;} \quad (5.20)$$

Further, from Equation (5.4), ψ tends to be zero at infinity for the rock mass and so, it is deduced that $A_1 = A_2 = 0$, in Equation (5.16), with the *boundary conditions* (5.19) and (5.20). Thus, the shortened thermo-elastic equations after eliminating the integration constants A_1 and A_2 become:

$$u_{11} = \frac{u_r}{r_o} = \frac{1+\nu}{1-\nu} \frac{\alpha_e(T_a-T_V)}{\xi} \int_1^\xi \psi \xi \, d\xi \quad (5.21)$$

$$s_{11} = \frac{\sigma_r}{E} = -\frac{1}{1-\nu} \frac{\alpha_e(T_a-T_V)}{\xi^2} \int_1^\xi \psi \xi \, d\xi \quad (5.22)$$

$$s_{22} = \frac{\sigma_\theta}{E} = \frac{1}{1-\nu} \frac{\alpha_e(T_a-T_V)}{\xi^2} \int_1^\xi \psi \xi \, d\xi - \frac{\alpha_e(T_a-T_V)\psi}{1-\nu} \quad (5.23)$$

$$s_{33} = \frac{\sigma_z}{E} = -\frac{\alpha_e(T_a-T_V)\psi}{1-\nu} \quad (5.24)$$

In this paper, solutions to the dimensionless temperature parameter, ψ were incorporated into Equations (5.21) to (5.24) to study the thermo-elastic effects.

5.3 Discussion

5.3.1 Sources of parameters used in analysis

In Table 5-1, the tunnel radius and the rock thermal properties are as given by Bottomley (Bottomley, 1985) and Chellam (Chellam, 1992), and the mechanical properties of rock are as shown by Rahmani *et al.* (Rahmani et al., 2011). The characteristics of the shotcrete insulation layer have been taken from an earlier study by the present authors (Liu et al., 2011). The mine environmental conditions

were assumed based on investigations from Pickering and Tuck (Pickering and Tuck, 1997, Tuck, 1997).

5.3.2 Comparative analysis of cylindrical models

5.3.2.1 Surface dimensionless temperature profile

Dimensionless surface temperature (ψ_s) profile with *Fourier number* (Fo) on the tunnel surface is shown in Figure 5-2. As seen therein, no significant difference is observed in the overall trend among the various solutions discussed above, Figure 5-2(a). A rapid temperature change from 0 to 0.8, with respect to Fo from 0 to 2 can be seen. Magnified plots corresponding to the small and large time-scale portions are shown in Figure 5-2(b) and Figure 5-2(c), respectively. In Figure 5-2(b), it is seen that for the results using Starfield and Bleloch's solution, the difference with regard to temperature from other solutions started to become noticeable, as Fo increases from 0 to 0.8. Whereas in Figure 5-2(c), only a minor temperature difference can be seen even after magnification with regard to the plot from using ABAQUS[®] software solution, the difference being insignificant. It was found to be actually less than 0.01. Therefore, from this discussion, it can be concluded that the ABAQUS model over a finite length outer boundary can be used to describe, quite reliably, the tunnel surface temperature in a semi-infinite rock mass.

5.3.2.2 Dimensionless temperature profile after 1 year time lapse

The dimensionless temperatures (ψ) at several locations from the tunnel wall surface were plotted in Figure 5-3 for the three analytical and ABAQUS[®] numerical solutions. It is seen that using the Gibson solutions, referring to Equation (5.8), it is not possible to depict values at other rock locations than the tunnel surface. From Figure 5-3, it is seen that, after 1 year, temperatures at several different locations from the tunnel surface as derived from different solution approaches match each other very well, showing the same decreasing trend. However, differences do become noticeable for the values $\xi > 5$, compared to those for $\xi < 5$. Again, this temperature profile study also indicates that the use of ABAQUS[®] software offers a reliable tool to predict temperature at any location inside the rock mass at any time regarding the heat transfer problem with semi-infinite outer boundary.

5.3.2.3 Dimensionless temperature gradient

The heat flux through tunnel surface (q_s) in the unit of W/m^2 is directly related to the dimensionless surface temperature gradient (G_s) as shown in Equation (5.25), thus G_s is discussed in this section for both analytical and numerical analysis.

$$q_s = k \frac{\partial T}{\partial r} \Big|_{r=r_o} = \frac{k(T_a - T_V)}{r_o} \frac{\partial \psi}{\partial \xi} \Big|_{\xi=1} = - \frac{k(T_a - T_V)}{r_o} G_s \quad (5.25)$$

where k is the thermal conductivity of rock ($\text{W/m}^2 \text{ K}$), q_s is the heat flux through tunnel surface (W/m^2); G_s is the dimensionless temperature gradient.

As shown in Equation (5.25), the dimensionless temperature gradient at surface (G_s) forms the key part in expressing the surface heat flux (q_s). In other words, provided that the dimensionless temperature gradient (G_s) is known, the surface heat flux (q_s) can be easily calculated from Equation (5.25), by multiplying G_s with a constant factor. Thus, the curved profile of G_s is the same as that of q_s .

Figure 5-4 displays the relationship between surface temperature gradient (G_s) and time, in the form of a curve of G_s and Fo . In Figure 5-4(a), it can be seen that the plot using ABAQUS software shows values different from other solutions in the initial stages, i.e. for Fo from 0 to 0.005. A magnified version as shown in Figure 5-4(b) clearly throws up this difference after 0.005. For the range of Fo from 0 to 0.005, the corresponding G_s shows a steep increase from 0 to about 2.5, whereas from using other analytical solutions, G_s dropped from 3.5 to about 2.5 for the same range of Fo ; Also, it can be seen that for Fo greater than 0.005, all three curves namely, those derived from ABAQUS, Carslaw and Jaeger's solution and Gibson's solution – almost coincided with one another. However, Starfield and Bleloch's solution of G_s is 0.5 lower than that from other solutions but with a similar trend. Figure 5-4(c) shows this closer similarity of G_s values from all three models. Although from ABAQUS[®] software, the initial values for G_s ($Fo < 0.005$)

differs from those from other models and so, it may not be so reliable. Yet, it gives a trustworthy result for higher values of Fo for temperature gradients at other locations away from the tunnel surface and inside the infinite rock mass. A more general form of temperature gradient for other locations is displayed in Equation (5.26),

$$G = \frac{r_o}{T_V - T_a} \frac{\partial T(r,t)}{\partial r} = - \frac{\partial \psi(\xi, Fo)}{\partial \xi} \quad (5.26)$$

Gibson's solution is not found suitable to other locations inside the rock mass except for the tunnel surface. Figure 5-5 displays the dimensionless temperature gradient (G) at different locations from the tunnel surface: It can be noted that for values of $\zeta < 5$, the results from all three solutions matched with one another quite well, whereas for values of $\zeta > 5$, Starfield and Bleloch's solution began to differ slightly from the other two. By substituting Equation (5.12) into Equation (5.26), a simple expression of G from Starfield and Bleloch's solution can be shown as below,

$$G = - \frac{Bi}{1 + Bi \ln(R)} \frac{1}{\xi} = \frac{G_s}{\xi} \quad (5.27)$$

Equation (5.27) provides us an easy and quick way to precisely estimate temperature gradient or heat flux in the area near the tunnel rock surface (i.e. $\zeta < 5$), and also evaluate reasonably these values in the areas away from the surface and in the rock mass (i.e. $\xi > 5$), without the derivation of complex *Bessel equations* in Equation (5.6), provided of course, the surface temperature gradient

is known. In summary, therefore, our study shows that the ABAQUS[®] model can be confidently used for cases of finite length outer boundary of rock mass, to get the description of temperature and the heat flux for different locations and at different times to get reliable values. A simple expression as shown in Equation (5.27) has been found to get the relationship between surface temperature gradient and temperature gradients at other locations with the rock mass.

5.3.2.4 Heat Penetration depth

The concept of heat penetration depth (D_p) has been mentioned earlier by the present authors, Liu *et al.* (Liu et al., 2012). Basically, D_p gets deeper into the rock mass, as time grows. And the expression of D_p can be transformed from Equation (5.13) (Starfield, 1969), as below,

$$D_p(F_o) = r_0 R = r_0 e^{\frac{1}{G_p(F_o)}} \quad (5.28)$$

Equation (5.28), the development of D_p with time, in terms of F_o , is displayed in Figure 5-6. With the aim of outer boundary length comparisons, three characteristic points are selected on the curve of Figure 5-6, namely point A, B and C, D_p of 5 m and 10 m are marked at points A ($F_o = 0.8$), at B ($F_o = 5.3$), and at point C at the end of 1 year ($F_o = 18.9$), and with D_p of 17.1 m.

As for the importance of outer boundary location in the ABAQUS[®] model, one sensitivity analysis of outer boundary location on that was conducted in the form

of surface temperature gradient, as shown in Figure 5-7 and Figure 5-8. Three locations of outer boundaries in the cylindrical coordinate system are chosen at $L = 21$ m, $L = 10$ m and $L = 5$ m, the latter two being in accordance with the characteristic points in Figure 5-6. Then, the surface dimensionless temperature gradient is plotted in Figure 5-7 within the time period of 1 year ($Fo = 18.9$). Results are also compared with Carslaw and Jaeger's solution. In Figure 5-7, it can be seen that the ABAQUS solution at location ($L = 5$ m) started to differ from Carslaw and Jaeger's analytical solution at an early stage, and ABAQUS solution for location ($L = 10$ m) distinguished from Carslaw and Jaeger's solution as time elapses that is, starting from Fo of about 5.3. The ABAQUS solution for location ($L = 21$ m) matched nicely with Carslaw and Jaeger's solution without any noticeable difference. It is worth mentioning that no apparent difference was detected in the range ($Fo < 0.8$) between ABAQUS models as well as Carslaw and Jaeger's solution for all three locations chosen. But, in Figure 5-8, it is found that at $L = 5$ m, ABAQUS solution began to be distinct from other solutions for values of $Fo > 0.8$. As seen from Figure 5-6, the *Fourier numbers* (Fo) for heat penetration depth ($D_p = 5$ m, $D_p = 10$ m, $D_p = 17$ m) were at about 0.8, 5.3, and 18.9 respectively; Then from Figure 5-7 and Figure 5-8, it is found that the ABAQUS solution ($L = 5$ m) and ABAQUS solution ($L = 10$ m) start to separate from the exact Carslaw and Jaeger's solution at Fo of about 0.8 and 5.3, and

ABAQUS solution ($L = 21$ m) shows no notable difference with Carslaw and Jaeger's solution. In a word, after seeing Figure 5-6, Figure 5-7 and Figure 5-8, we may conclude that the scale of finite length outer boundary (L) does influence the reliability and precision of ABAQUS model to depict the semi-infinite rock mass problem. The finite outer boundary length (L) has to be defined larger than the heat penetration depth (D_p) within a specified time period to ensure the accuracy of this semi-infinite problem in ABAQUS model, otherwise, if L is not adequate as the ABAQUS solution ($L = 5$ m) and ABAQUS solution ($L = 10$ m) as shown in Figure 5-7 and Figure 5-8, results would differ from the real values from the time the heat penetration depth (D_p) has reached the smaller finite length outer boundary (L).

5.3.3 Effects of thermal insulation

The effects of thermal insulation on the heat abatement were evaluated by the Equivalent Overall Heat Transfer Coefficient Method. Since the thickness of insulation layer is negligible, when compared with that of the rock mass, the steady-state equilibrium in the insulation layer can be taken to reach rapidly. Thus, the dimensionless temperature gradient (G_s) can be now expressed by the following simplified version, given in Equation (5.31) (Liu et al., 2012), in which Bi_{eff} of Equation (5.30) is the effective *Biot Number*, and h_{eff} in Equation (5.29) is the effective heat transfer coefficient ($W/(m^2 \text{ K})$) determined from the initial heat

transfer coefficient h ($\text{W}/(\text{m}^2 \text{ K})$) of tunnel surface before applying shotcrete; k_1 is the thermal conductivity of shotcrete ($\text{W}/(\text{m K})$); r_o is the radius (m) of the tunnel before applying any shotcrete; r_{in} is the radius (m) of the tunnel after shotcreting.

$$h_{eff} = \frac{1}{\frac{1}{h} + \frac{r_o \ln(r_{in}/r_o)}{k_1}} \quad (5.29)$$

$$Bi_{eff} = \frac{h_{eff} r_o}{k} \quad (5.30)$$

$$G_s = -Bi_{eff}(\psi_s - 1) \quad (5.31)$$

As seen in Figure 5-2, the dimensionless surface temperature gradient (G_s) tends to be different for different dimensionless times (Fo); therefore, without taking into account the cumulative effects due to a certain time period, G_s or q_s , at one specific time can hardly reflect the real thermal effects of the insulation on the mine atmosphere. Therefore, in this paper, the average dimensionless surface temperature gradient ($\overline{G_s}$) is introduced to be the index of thermal effects of insulation, as in Equation (5.32). The average dimensionless surface temperature gradient ($\overline{G_s}$) is

$$\overline{G_s} = \frac{1}{\tau} \int_0^\tau G_s dF_o \quad (5.32)$$

where $\overline{G_s}$ is the average dimensionless surface temperature gradient; Q_s is the surface temperature gradient accumulation; τ is the ending time (s) over which the integration is carried out.

From Carslaw and Jaeger's solution, the dimensionless surface temperature gradient (G_s) is plotted with dimensionless time (Fo), as shown in Figure 5-9(a)

and in Figure 5-9(b). In Figure 5-9(a), the area under the curve depicts the cumulative dimensionless surface temperature gradient (Q_s). And in Figure 5-9(b), the accumulative gradient is plotted against Fo . Table 5-2 lists the results of thermal insulation shotcrete as the insulation layer; it can be seen that the heat reduction ratio from these four different groups of solutions varied from 26.8% to 29.3%, with the average of $28.4\% \pm 1.1\%$. This has proved that all models of the solutions can be used to estimate the effects of thermal insulation by shotcrete without much difference. The foregoing discussion also establishes that providing a thermal insulation is an effective way of achieving considerable reduction in surface temperature (i.e. in this case study, $28.4\% \pm 1.1\%$ reduction by using shotcrete), with sufficient heat abatement into underground tunnels.

5.3.4 Thermal stresses

It is well known that any solid body undergoing temperature changes in it experiences thermal strains due to restricted expansion or contraction and hence thermal stresses. In this paper, the thermal stresses induced in the tunnel are discussed both through the analytical solutions and through modelling with ABAQUS. In the approach through the Carslaw-Jaeger's solutions, the time dependent temperature field is substituted into the thermo-elastic Equations (5.21) through (5.24), whereas in the ABAQUS solutions, previous time dependant temperature field with an outer boundary length of 21 m is considered as a

predefined analysis step. Comparisons of results from both approaches lead to the following observations:

Thermal stresses on the opening surface from the two methods are compared in Figure 5-10 and Figure 5-11. It is to be noted here that the compressive stress is taken as negative (–), while the tensile stress is taken to be positive (+) throughout this paper. As shown in Figure 5-10, the dimensionless radial stress s_{11} is considered to be zero due to the free surface in radial direction (the r direction in Figure 5-1), as predicted from Equation (5.22). However, it can be seen from Figure 5-10, that on the tunnel surface, the sign of radial stress s_{11} from the ABAQUS model fluctuates initially at the same specific time, even though it is not possible to have two values at one time. However, since the fluctuations are within a tiny range very near to zero from -3.5 to 4.5, these values can be taken as zero itself compared to the large scale adopted in Figure 5-10 and Figure 5-11, after comparing to the stress scale in the forthcoming figures, s_{11} in ABAQUS is still considered as zero, though it is not as exact as that in analytical solutions. In Figure 5-11(a), the figure shows the relationship of the tangential stress s_{22} and axial stress s_{33} with respect to dimensionless time Fo , similar to the curve shape in Figure 5-2, both s_{22} and s_{33} experience a steep increase from 0, then they level out to a stable level of about 120×10^{-6} . In Figure 5-11(a) and (b), the equivalence between s_{22} and s_{33} is noticed in analytical solutions and ABAQUS solutions

individually. This equivalence can be explained from Equation (5.23) and (5.24), when ζ comes to 1 at the surface, the integral part in Equation (5.23) grows to 0, leading to the equality between s_{22} and s_{33} . In addition, the curve from ABAQUS solution has a minor difference from the analytical solution, it seems like s_{22} and s_{33} in the analytical solutions are a little bit larger than that in ABAQUS solutions. Referring to Figure 5-11(b), which is the enlarged plot at Fo range between 0 to 0.01, shows the same difference.

Figure 5-12(a), (b), (c) and (d) have shown the location distributions of dimensionless displacement (u_{11}), dimensionless radial stress (s_{11}), dimensionless tangential stress (s_{22}), dimensionless axial stress (s_{33}), deep into the rock mass along with radial axis, at Fo of 18.9, which equals to the elapsed time of one year. Figure 5-12(a) illustrates the displacement evolution from the tunnel surface to the far-away rock mass, with ζ as large as 10, here, in terms of the displacement of u_{11} , a good matching between analytical and ABAQUS curves has been found, with ζ less than about 2.25, whereas, after reaching this location, they start to differ from each other. In Figure 5-12(b), two paralleled curves of s_{11} , first increase with the distance from surface, after reaching the peak points at ζ of about 2.25, then drop continuously at further distance, it is important to mention that the ABAQUS solution of s_{11} at the tunnel surface ($\zeta = 1$) can still be thought as 0, due to its fluctuations at surface, as clarified in Figure 5-10. Then as shown in Figure 5-12(c)

and (d), unlike s_{11} , s_{22} and s_{33} have a larger scale of stress values, viewing the dimensionless stress from 0 to 125×10^{-6} ; their maximum stress values first appear at the tunnel surface, and then decrease gradually with the dimensionless ξ , as a result, for application purpose, we may just focus on the area near tunnel surface. As seen from Table 5-12(b) and (c), stresses of s_{11} and s_{33} are all under tension, whereas in Table 5-12(c), it is also interesting to note that s_{22} initially functions under tension, then after reaching a certain distance, it becomes to be compressive, however at a very small scale. After above discussions, it is not difficult to draw the conclusion that the thermal stress provoked by temperature field can be predicted by analytical equations or FEM software ABAQUS[®], the good correlations from above figures have proved the validity of both of the theoretical ways for this specific underground cooling problem surrounded with semi-infinite boundary, and the thermal stresses here can be superposed on the excavation induced stresses (Hoek et al., 1995).

5.4 Concluding remarks

On the basis of the discussions in the comparative study of analytical models and numerical models, several conclusions can be draw as follows:

1. Thermal insulation with shotcrete has been confirmed as an effective heat abatement method, by comparing cylindrical models with three different

analytical solutions as well as one ABAQUS numerical simulation. The annual average heat flux reduction of 28.4% can be expected at the end of one year.

2. In hot mines, the thermal stresses induced by the temperature field change in the infinite rock mass are almost considered as tensile stresses, under the circumstance of ventilation and cooling.

3. ABAQUS[®] is the software we can trust in simulating heat transfer process in the infinite rock mass region bounded internally by the tunnels, more complex full three dimensional models can be explored in forthcoming studies. However, the model boundary setup has to be very careful to ensure the finite outer boundary length is larger than the penetration depth (D_p), analytical prediction of D_p is preferred.

This work has established the theoretical confidence of using shotcrete as the thermal insulation layer in underground mines.

Appendix

Appendix 5-1 Gibson's algorithm (After Gibson) (McPherson, 1986, McPherson and Hinsley, 1993)

$$f_1 = \text{Log}_{10}(Fo)$$

$$b_1 = \text{Log}_{10}(Bi)$$

$$c_1 = f_1(0.000104f_1 + 0.000997) - 0.001419$$

$$c_2 = -\{f_1[f_1(f_1c_1 - 0.046223) + 0.315553] + 0.006003\}$$

$$d_1 = b_1 - [f_1(4f_1 - 34) - 5]/120$$

$$d_2 = 0.949 + 0.1e^{-2.69035d_1^2}$$

$$m = \sqrt{(b_1 - c_2)^2 + \frac{216+5f_1}{70} [0.0725 + 0.01 \tan^{-1}(\frac{f_1}{0.7048})]}$$

$$n = \frac{b_1 + c_2 - m}{2}$$

$$G = 10^n/d_2$$

Nomenclature in Chapter 5

A_1, A_2 Integration constants

u variable for integration in *Bessel* equations, without any physical meanings

Y_0, Y_1, J_0, J_1 Bessel equations

D_p Heat penetration depth (m)

T Temperature (K)

T_0 Initial Temperature (K)

T_V Virgin rock temperature (K)

T_R Reference temperature (K)

T_a Air temperature (K)

T_s Tunnel surface temperature (K)

T_{in} Interface temperature (K)

r Distance with respect to axis of cylindrical opening (m)

r_o Cylindrical opening radius after shotcreting (m)

r_{in} Cylindrical opening radius before shotcreting (m)

δ Thickness of the insulation layer (m)

t Time (s)

k, k_1, k_2 Thermal conductivity (W/(m K))

$\alpha, \alpha_1, \alpha_2$ Thermal diffusivity (m²/s)

α_e Linear coefficient of thermal expansion (1/K)

- λ Dimensionless parameter α_2 / α_1
- h Heat transfer coefficient (W / (m² K))
- ψ Dimensionless temperature: $\psi = (T - T_V) / (T_a - T_V)$
- ψ_s Surface dimensionless temperature: $\psi_s = (T_s - T_V) / (T_a - T_V)$
- θ The angle in cylindrical coordinate system
- G Dimensionless temperature gradient
- G_s Tunnel surface dimensionless temperature gradient
- Q_s Accumulative dimensionless surface temperature gradient
- \overline{G}_s The average tunnel surface dimensionless temperature gradient
- G_p Goch-patterson flux
- ξ Dimensionless length: $\xi = r / r_o$
- Fo Dimensionless time, known as *Fourier number*: $Fo = (\alpha_2 t) / r_o^2$
- Bi Dimensionless heat transfer coefficient, known as *Biot number*:
- $$Bi = (h r_o) / k_2$$
- q_s Surface heat flux (W/m²)
- R Dimensionless time dependant outer boundary
- ν Poisson's ratio
- E Young's modulus (GPa)
- u_r Radial displacement (m)
- σ_r Radial stress (Pa)

σ_θ Tangential stress (Pa)

σ_z Axial stress (Pa)

u_{11} Dimensionless radial displacement: $u_{11} = u_r / r_0$

s_{11} Dimensionless radial stress: $s_{11} = \sigma_r / E$

s_{22} Dimensionless tangential stress: $s_{22} = \sigma_\theta / E$

s_{33} Dimensionless axial stress: $s_{33} = \sigma_z / E$

Tables in Chapter 5

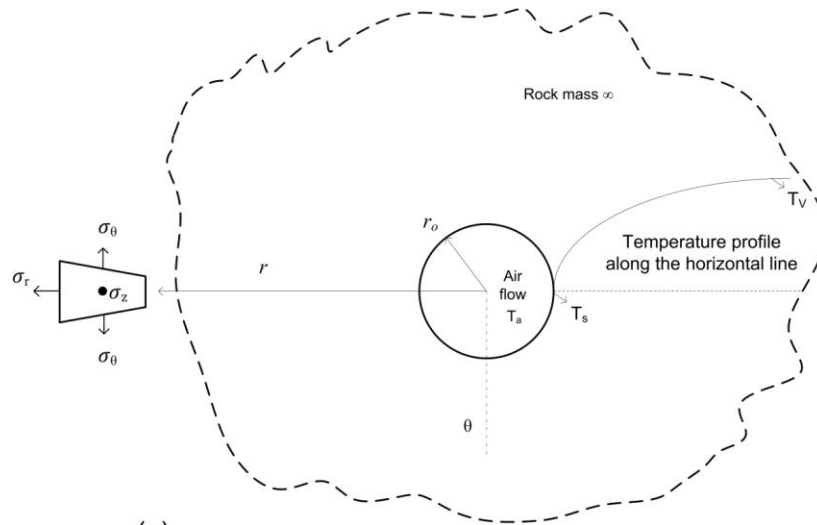
Table 5-1 Input parameters

Parameters	Input values
Air temperature (T_a)	301.0 K
Virgin rock temperature (T_V)	323.0 K
Heat transfer coefficient (h)	10.0 W / (m ² K)
Opening radius (r_o)	2 m
Outer boundary length for finite models (L)	21 m
Thermal conductivity of shotcrete (k_1)	0.3799 W / (m K)
Density of shotcrete (ρ_1)	1169.07 kg/m ³
Specific heat capacity of shotcrete (C_{p1})	945.2 J / (kg K)
Thermal diffusivity of shotcrete (α_1)	3.438×10^{-7} m ² / s
Insulation shotcrete thickness (δ)	0.1 m
Thermal conductivity of rock (k_2)	6.00 W / (m K)
Density of rock (ρ_2)	2700.0 kg/m ³
Specific heat capacity of rock (C_{p2})	925.9 J / (kg K)
Thermal diffusivity of rock (α_2)	2.40×10^{-6} m ² / s
Young's modulus of rock (E)	6 GPa
Poisson's ratio of rock (ν)	0.25
Linear coefficient of thermal expansion (α_e)	5×10^{-6} 1/K

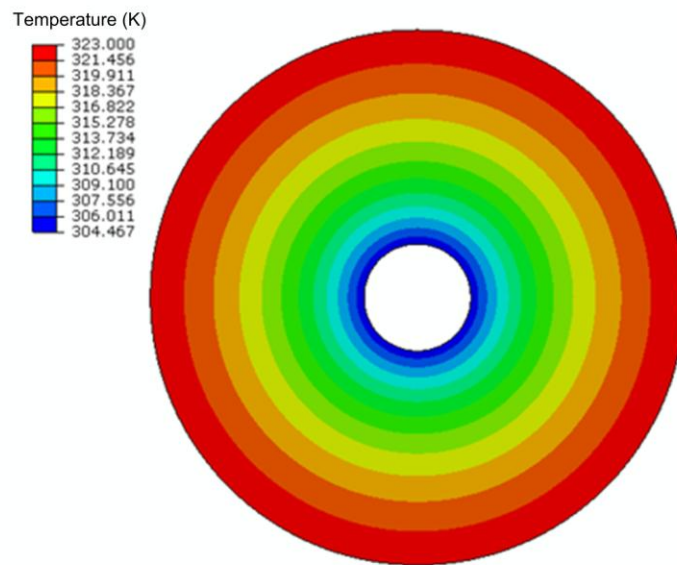
Table 5-2 Thermal insulation effects at 1 year ($Fo = 18.9$)

Solution Group	Average dimensionless surface temperature gradient (\bar{G}_s)		Abatement	Abatement ratio
	No insulation	Insulation		
	ABAQUS's	0.548		
Carslaw and Jaeger's	0.530	0.379	0.151	28.457%
Gibson's	0.525	0.384	0.141	26.806%
Starfield and Bleloch's	0.513	0.363	0.150	29.313%
Average	0.529±0.015	0.379±0.011	0.150±0.008	28.403% ±1.122%

Figures in Chapter 5



(a)



(b)

Figure 5-1 Temperature field in cylindrical tunnel

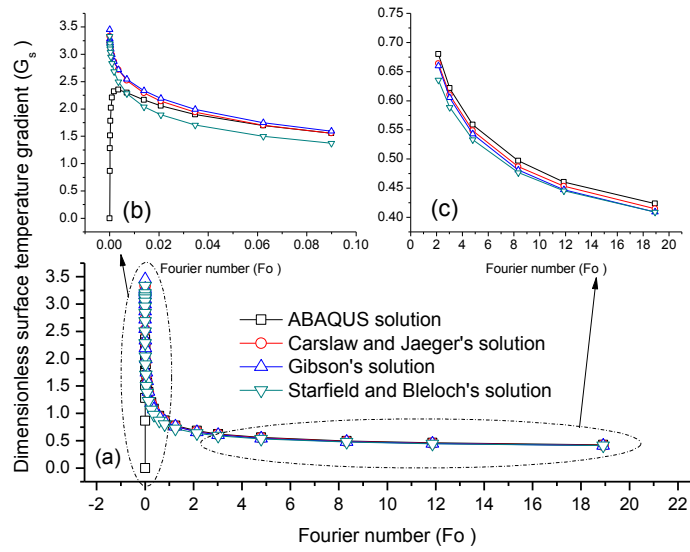


Figure 5-4 Surface temperature gradient with time

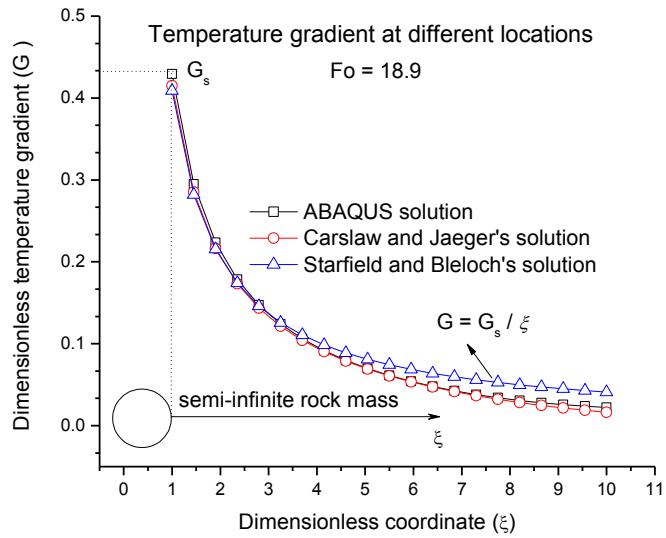


Figure 5-5 Temperature gradient distributions at one year

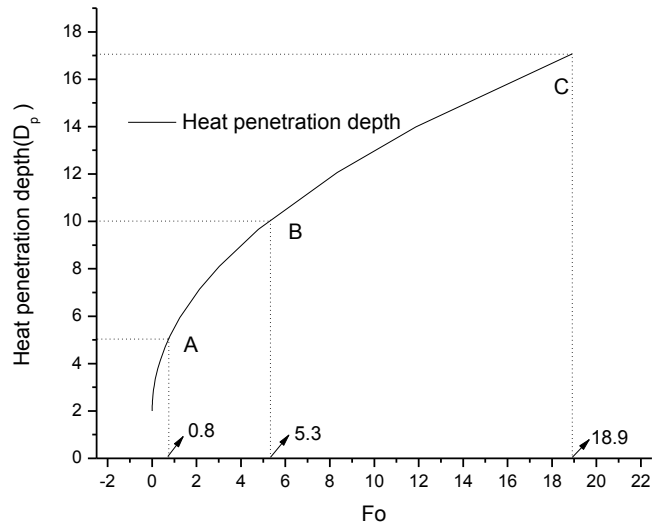


Figure 5-6 Heat penetration depth (D_p) with time

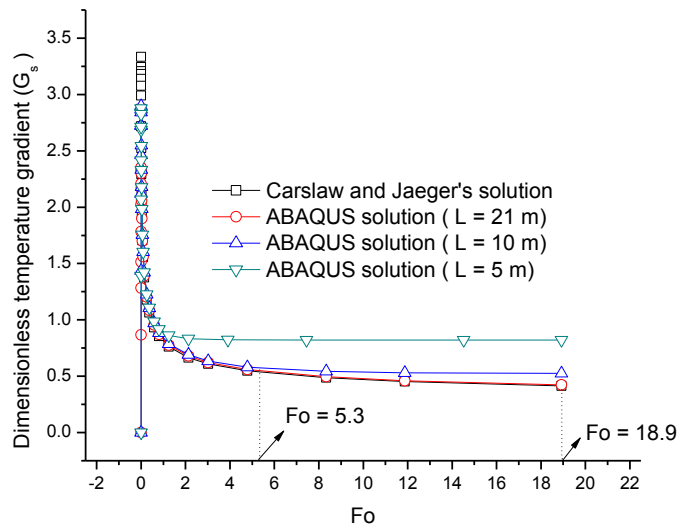


Figure 5-7 ABAQUS solutions with different outer boundary lengths

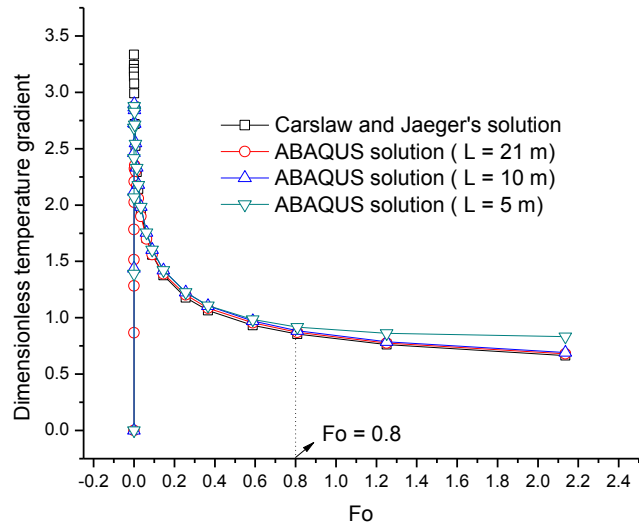


Figure 5-8 ABAQUS solutions with different out boundary lengths (small time scale)

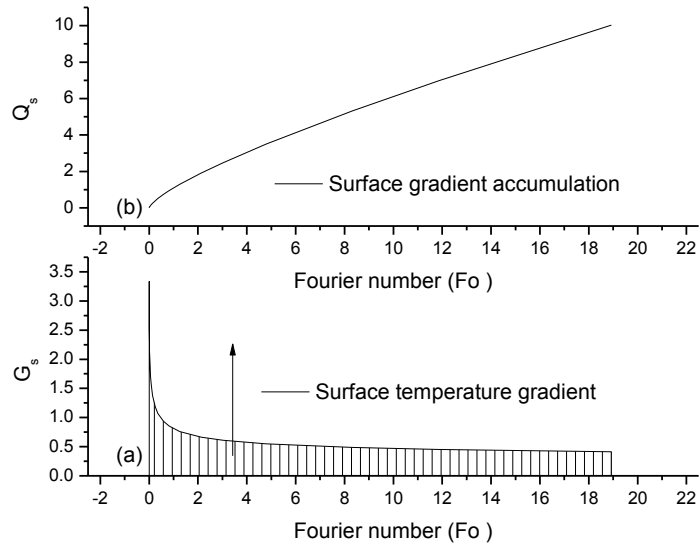


Figure 5-9 Integration of surface temperature gradient

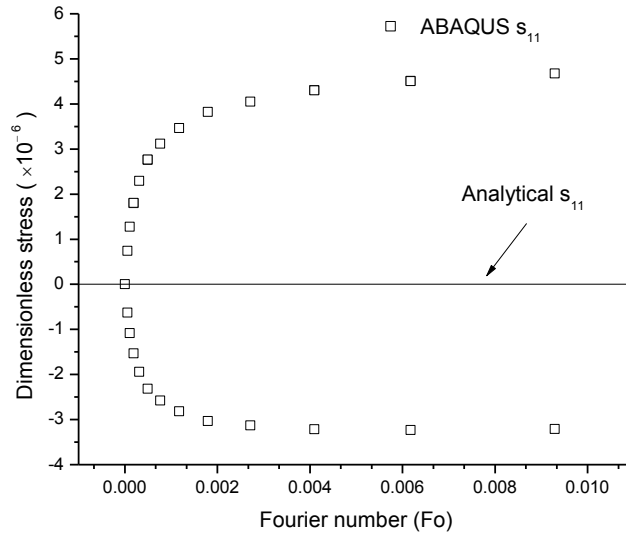


Figure 5-10 Surface s_{11} with time

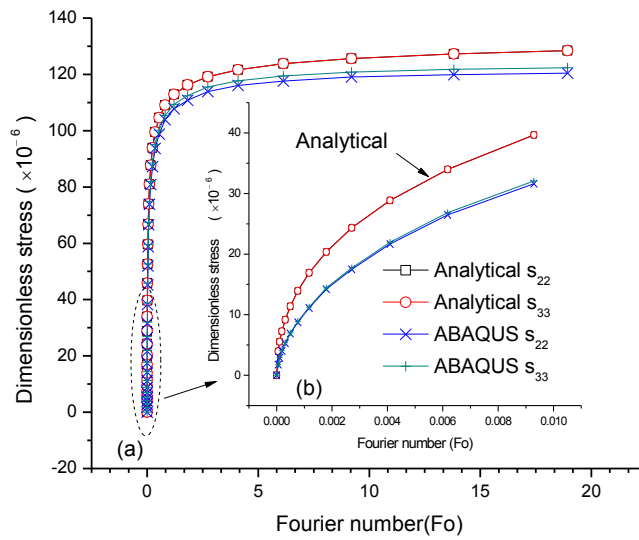


Figure 5-11 Surface s_{22} and s_{33} with time

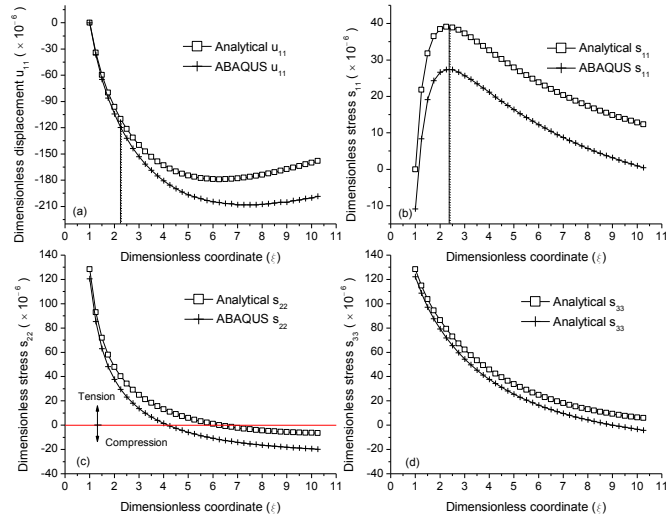


Figure 12 u_{11} , s_{11} , s_{22} and s_{33} distributions at one year

References

- Abaqus Users Manual, V. 6.10-1. *Dassault Systemes Simulia Corp., Providence, RI.*
- Bindiganavile, V. & Banthia, N. (2009) Effect of particle density on its rebound in dry-mix shotcrete. *Journal of Materials in Civil Engineering*, 21, 58-64.
- Bottomley, P. (1985) The reduction in heat flow due to the insulation of rock surfaces in mine airways. *2nd US Mine Ventilation Symposium*. Reno, NV.
- Carslaw, H. S. & Jaeger, J. C. (1959) *Conduction of heat in solids*, Oxford: Clarendon Press, 2nd ed.
- Chellam, S. (1992) Thermal insulation of underground mine workings at deep levels. *Department of Mining Engineering*. Rapid City, South Dakota, South Dakota School of Mines and Technology.
- DSIMULIA (2004) Heat Transfer and Thermal-Stress Analysis with Abaqus.
- Gibson, K. (1976) The Computer simulation of climatic conditions in underground mines. Ph. D Thesis, University of Nottingham, UK.
- Goch, D. C. & Patterson, H. S. (1940) The Heat flow into tunnels, *Journal of the Chemical, Metallurgical and Mining Society of South Africa*. Sept, 117-128.
- Hartman, H. L., Mutmansky, J. M., Ramani, R. V. & Wang, Y. J. (1998) Environmental control of the mine atmosphere. *Mine ventilation and air conditioning*. Third Edition.
- Hoek, E., Kaiser, P. K. & Bawden, W. F. (1995) *Support of underground excavations in hard rock*, Taylor & Francis.
- Howarth, D. F. & Gillies, A. D. S. (1987) An examination of insulation used on mine refrigeration chilled water pipes. *Geotechnical and Geological Engineering*, 5, 83-91.
- Jing, L. (2003) A review of techniques, advances and outstanding issues in numerical modelling for rock mechanics and rock engineering. *International Journal of Rock Mechanics and Mining Sciences*, 40, 283-353.
- Jing, L. & Hudson, J. A. (2002) Numerical methods in rock mechanics. *International Journal of Rock Mechanics and Mining Sciences*, 39, 409-427.
- Kumar, P. & Singh, B. (1989) Thermal stress analysis of underground openings. *International Journal for Numerical and Analytical Methods in Geomechanics*, 13, 411-425.

- Liu , H. Y., Small, J. C. & Carter, J. P. (2008) Full 3D modelling for effects of tunnelling on existing support systems in the Sydney region. *Tunnelling and Underground Space Technology*, 23, 399-420.
- Liu, W. V., Apel, D. B. & Bindiganavile, V. (2011) Thermal characterisation of a lightweight mortar containing expanded perlite for underground insulation. *International Journal of Mining and Mineral Engineering*, 3, 55-71.
- Liu, W. V., Apel, D. B., Bindiganavile, V. S. & Szymanski, J. K. (2012) Comparison of methods in theoretical analysis of thermal insulation for underground tunnels. *CIM Journal (under peer review)*.
- McLachlan, N. W. (1955) *Bessel functions for engineers*, Clarendon Press Oxford.
- McPherson, M. J. (1986) The analysis and simulation of heat flow into underground airways. *Geotechnical and Geological Engineering*, 4, 165-195.
- McPherson, M. J. & Hinsley, F. B. (1993) Chapter 15: Heat flow into subsurface openings. *Subsurface ventilation and environmental engineering*. Chapman & Hall London.
- Pickering, A. J. & Tuck, M. (1997) Heat: sources, evaluation, determination of heat stress and heat stress treatment. *Mining Technology*, 79, 147-56.
- Rahmani, N., Nikbakhtan, B., Ahangari, K. & Apel, D. (2011) Comparison of empirical and numerical methods in tunnel stability analysis. *International Journal of Mining, Reclamation and Environment*, 1-10.
- Spalding, J. (1949) *Deep Mining*. Mining Publications, London.
- Starfield, A. M. (1969) A rapid method of calculating temperature increases along mine airways. *Journal of the South African Institute of Mining and Metallurgy*. November.
- Starfield, A. M. & Bleloch, A. L. (1983) A new method for the computation of heat and moisture transfer in a partly wet airway. *Journal of the South African Institute of Mining and Metallurgy*, 263-269.
- Sukhatme, S. P. (2011) Analysis of heat conduction and some steady one-dimensional problems. *A Text Book on Heat Transfer*. Cambridge, Massachusetts, Phlogiston Press.
- Timoshenko, S. & Goodier, J. N. (1951) *Theory of Elasticity*, McGraw-Hill.
- Tuck, M. A. (1997) Control of mine climate. *Mining Technology*, 79, 215-220.
- USBM (1994) An 'insulating' shotcrete for heat abatement in deep mines. *Technology News* 434.
- Wagner, H. (2010) The management of heat flow in deep mines / . Management von Wärmeströmen in tiefliegenden Bergwerken. *Geomechanics and Tunnelling*, 3, 609-621.

Chapter 6 Full three-dimensional modelling for thermal insulation effects of shotcrete in a typical underground mine

6.1 Introduction

As underground mines go deeper with the continuous high demands of minerals all across the world, many mines would encounter the problem of higher virgin rock temperatures (VRT), once the VRT rises to the point that is higher than the temperature of mine atmosphere, heat starts to flow from the rock into airways to warm up the air. This type of heat from the hot rocks is also mentioned as geothermal heat, it is considered as the primary source of heat loads in deep underground mines (Rawlins and Phillips, 2001, Wagner, 2010). To ensure the safety and comfort of mine workers, the air temperature has to be mandatorily maintained at a standard level per different regulations (Pickering and Tuck, 1997, Tuck, 1997), thus excess heat from rock is required to be transported out of the working areas by using the ventilation and refrigeration system (Hall et al., 1984). However, there is an exponential increase of costs in the ventilation and refrigeration system along with greater depth (Bottomley and van Rensburg, 1987, Sheer et al., 1984). Therefore, economic and feasible methods which can reduce the heat loads from rock to underground openings are greatly expected to solve

this problem. It is long believed that the application of low thermal conductive insulation layer on the rock surface of openings is an effective measure to reduce heat loads (Bottomley, 1985, Bottomley and van Rensburg, 1987, Chellam, 1992, Wagner, 2010). Nevertheless, the research for the theoretical fundamental of using insulation in hot mines still appears inadequate to convince its further applications. Briefly speaking, the theoretical fundamental is inadequate in two aspects:

First, from mathematical point of view, inadequate systematic mathematical explanations and formula deductions have been found according to the authors' searching until now in regard to the insulation effects in underground openings, this problem is actually the transient heat conduction problem in a semi-infinite virgin rock mass with finite length insulation layer, which has heat convection and radiation boundary with ventilation air at the inner surface of tunnels. For example, Bottomley (Bottomley, 1985) used an equivalent heat transfer coefficient to predict lower heat loads without noting any detailed reason to use this formula. Ashworth (Ashworth, 1992) used steady-state heat conduction analytical solutions however this is a transient phenomenon in reality. Current authors have explored and compared mathematical solutions in details, and furthermore, have verified the Finite element method software (FEM) ABAQUS®

(Abaqus Users Manual) to simulate thermal insulation in underground openings (Liu et al., 2012b, Liu et al., 2012c).

Second, from the dimensional and scale point of view, most previous research focused on two dimensional simulations of thermal insulation (Ashworth, 1992, Chellam, 1992, Rao et al., 1994) and just one single tunnel without considering the actual mine ventilations networks (Gilani, 2010). No simulation until now has been found to be on the full three dimensional mine level scale. The establishment of model in mine level scale is important because tunnels under a complicated ventilation system would influence the heat transfer of each other and an overview of the thermal insulation for a larger system becomes very necessary.

In this research, shotcrete with certain strength for rock support has been developed as the thermal insulation layer, which also plays the role as structural support in underground mines (Liu et al., 2011, Liu et al., 2012a). The commercial finite element method (FEM) software ABAQUS[®] (Abaqus Users Manual) has been used for thermal modelling in this study. FEM is currently widely accepted as the most popular analysis means in numerical modeling on rock engineering applications (Jing, 2003, Jing and Hudson, 2002), primarily targeting for the results of stress and displacement. Similarly, the heat transfer problem of rocks can also be solved by using FEM with a great accuracy (Reddy and Gartling, 2010, Singiresu, 2004). Furthermore, the accuracy of this software

has been verified by detailed comparisons with mathematical solutions from the authors' previous studies (Liu et al., 2012b, Liu et al., 2012c).

The objective of this paper is to provide further theoretical evidence for the use of insulation shotcrete containing expanded perlite aggregate (EPA) on rock surface inside the mine openings. Specifically, the attention has been paid to the heat loads reductions into the whole mine level by comparing the effects of shotcrete containing EPA with that of the shotcrete without EPA.

6.2 Numerical model

6.2.1 Field access

The tunnel layout of a typical deep underground metal mine in North America was used as the modelling object. The plan view of this level is located in a 120 m × 212 m area, as shown in Figure 6-1. Also, the field data of airflow distributions has been obtained along with the ventilation nodes, as stated in Table 6-1 and Figure 6-2.

6.2.2 Geometry of model

The geometry of the model was developed with respect to the field dimensions. However, several assumptions were made for simplification. For instance, the materials of both shotcrete and rock mass were assumed to be isotropic and homogeneous, and cross sections of tunnels were deemed to be constant though

the whole mine level. After considering the infinite outer boundary and the penetration depth of this problem as described in previous research (Liu et al., 2012b, Liu et al., 2012c), the outer scale of this model was extended to be a 300 m \times 450 m \times 100 m rock mass in Figure 6-3. And from Figure 6-4 (a) and (b), we can obtain the geometry for the tunnel cross sections of full and partial-insulation, correspondingly. In both cases, the tunnels have the same square shape of 4.3 m \times 4.3 m surrounded by the shotcrete layer of 100 mm and the homogeneous solid rock mass. As seen from Figure 6-5(a), (b) and (c), overview of shotcrete was firstly noticed, then a close view of shotcrete layer has been observed in the model for full and partial insulation, respectively.

6.2.3 Simulated scenarios

In order to assess the effects of shotcrete containing expanded perlite aggregate (EPA), the composition of the model contained two solid materials, namely, rock and shotcrete. The materials of both of them are explained here. First, for the rocks, four different rocks regarding thermal properties and virgin rock temperature were simulated in this model as listed in Table 6-2 in details. Rocks A, B and C have the same rock thermal properties as that in previous studies (Liu et al., 2012b, Liu et al., 2012c), though in three different virgin rock temperatures (VRT). Rock D was initiated from the field conditions in one Arizona hot mine (ADMMR, 2004, Manske and Paul, 2002), from which, the rock has the VRT as

high as 353 K, rich in pyrite, thus it is acceptable to use the thermal properties of pyrite (Goto and Matsubayashi, 2009, Midttomme et al., 1998) as one case of the surrounding rock. Then for the shotcrete, as seen from Table 6-3, the testing thermal properties of five different shotcrete samples were treated as input for the materials assignments of the shotcrete layer (Liu et al., 2012a). The batch name CP0, SP25, SP50, SP75 and SP100 represent the volumetrically replacement ratio of sands by expanded perlite aggregate (EPA) into shotcrete mixture at 0%, 25%, 50%, 75% and 100%, respectively. Specifically, batch CP0 was used as controlling sample here, all simulation results were compared with that of CP0 for heat load reductions.

6.2.4 Heat transfer coefficient

The heat transfer coefficient (h) is the most important parameter that has to be defined for the *Neumann boundary condition* (Cheng and Cheng, 2005, Liu et al., 2012b) to calculate the heat flows into tunnels. Before the heat transfer coefficient calculation, the average Atkinson friction factor (kg/m^3) was obtained from others' field testing results (Prosser and Wallace, 1999), according to their tests, the measured value of standardized Atkinson friction factor was 0.0088 kg/m^3 for metal mine drifts. It is reasonable to use the same standardized Atkinson friction factor in this ideal modelling. In mine ventilation, the heat transfer coefficient including both convection and radiation can be evaluated according to a procedure

after McPherson (McPherson and Hinsley, 1993), in addition, one computer program was developed as shown in Appendix 6-1 for the convenience of calculations. As a result, the heat transfer coefficients for each tunnel were displayed in Table 6-1. Each inner surface of the tunnel was assigned a corresponding heat transfer coefficient for defining the field *Neumann boundary conditions*.

6.2.5 Heat transfer modelling in ABAQUS®

To make the heat transfer simulation more clear, it is very necessary to briefly describe the general procedure of problem solving in the finite element method (FEM) software. For this full three dimensional heat transfer problem in the solid part, namely, the rock with shotcrete, there are 5 basic steps inside the software to make the problem solved, in terms of the sequences (Rao, 2005): Firstly, the solid body was meshed and divided by tet elements composed of nodes as demonstrated in Figure 6-6; Secondly, unknown temperature within elements were interpolated by assigning certain shape functions, which vary with element types; Thirdly, the element matrices and vectors were obtained based on the second step; Fourthly, the system matrices were assembled from element matrices; And lastly, the solutions regarding temperature and heat flux were deprived after applying defined boundary conditions.

As for the initial and boundary conditions, the rock mass was assumed to be constant at virgin rock temperature (VRT) at the initial point, after executing the simulation, the boundary conditions were applied, particularly, every inner surface of tunnel was assigned a unique *Neumann boundary condition*, in terms of their ventilation airflows; And at the faraway outer surface, the temperature was defined as the same as VRT, since this location was considered to be far enough to avoid large heat penetration influence. One year period of transient heat transfer was simulated for this mine level scale model.

6.3 Results and discussion

On the purpose of evaluating the effects of shotcrete for thermal insulation and energy savings, more attention was paid to the average annual heat load (kW) of the whole level that is closely related to the costs in ventilation and refrigeration system. After one year period simulation, the average heat flux (W/m^2) though surface as discussed previously (Liu et al., 2012b, Liu et al., 2012c) during one year was calculated and then the average annual heat load (kW) was obtained via multiplying by the total inner surface area (m^2) of this mine level.

6.3.1 Temperature distribution

As a typical illustration, after simulating Rock D with shotcrete layer SP50 for full-insulation, an overview of the temperature distribution on this model can be

seen in Figure 6-7, in which the upper Figure 6-7(a) has shown the temperature located on the outer boundary. From the color of legends in Figure 6-7(a), it is not difficult to find the fact that the outer boundary temperature was kept as 353 K which is the virgin rock temperature (VRT), based on the fact that the outer boundary of the model was set large enough to ensure the semi-infinite outer boundary that is the virgin rock undisturbed by ventilation and cooling (Liu et al., 2012b, Liu et al., 2012c). And a middle plane that cuts the depth into halves can help us observe the temperature distribution near the areas of tunnels, and Figure 6-7(b) is the cut view after removing the upper overburden. Two areas, in terms of Area 1 and Area 2, were zoomed in as illustrated in Figure 6-8(a) and (b), respectively. General speaking, the ventilation system would generate an influence zone around tunnels. And the influence zone has lower temperatures than VRT. From Figure 6-8(a) and (b), temperature distribution was also observed on the tunnel inner surface that is actually the shotcrete layer surface. By checking with the airflows in Table 6-1, we can roughly notice the fact that larger airflows would lead to lower inner surface temperatures.

6.3.2 Factors affecting heat loads before applying shotcrete with EPA

Heat loads before applying shotcrete with EPA, in other words, with shotcrete layer of sample CP0, were obtained for the controlling sample purpose.

As listed in Table 6-2, Rocks A, B and C have the thermal conductivity of 6 W/(m K), however with different virgin rock temperatures (VRT) of 323 K, 338 K and 353 K, individually. And Rock D after a hot mine in Arizona (ADMMR, 2004) has a higher thermal conductivity of 19.2 W/(m K), with the virgin rock temperature (VRT) of 353 K. Figure 6-9 has given us a straight forward demonstration of heat loads affected by the virgin rock temperature and rock thermal properties. As shown in Figure 6-9, from columns of Rocks A, B and C, we can conclude that the average heat loads into tunnels go up with the increase of virgin rock temperatures (VRT), from about 800 kW to 2000 kW, under the VRT from 323 K to 353 K. And comparisons were also conducted between Rocks C and D, bearing the fact that these two rocks were under the same VRT, but Rock D had a larger thermal conductivity. From the above comparison, it is noticed that the heat loads in Rock D jumped to 3500 kW, even under the same VRT of 353 K. Thus, it is concluded that both the increase of virgin rock temperature (VRT) and the thermal conductivity of rocks can result in larger heat loads into underground tunnels.

6.3.3 Influence of virgin rock temperature on heat load reductions

Shotcrete layer here functions as thermo-barrier to reduce heat loads into tunnels. After full-insulation of shotcrete, Figure 6-10 has shown the heat load reductions by adding expanded perlite aggregate (EPA) into shotcrete mixes. CP0 is the

controlling sample without any EPA additions, the other 4 groups including SP25, SP50, SP75 and SP100, have volume ratio of EPA for sands of 25%, 50%, 75% and 100%, correspondingly. 4 types of virgin rocks as explained in Table 6-2 were simulated by applying shotcrete with different EPA additions. As shown in Figure 6-10, under the Rocks A, B and C, apparent heat load reductions were observed in the curves. Moreover, curves of Rocks A, B and C, have the same heat load reduction percentages from 3% to 40% with additions of EPA from 25% to 100%. It is worth mentioning that the input simulated from Rocks A, B and C have the same thermal properties, in terms of density, thermal conductivity and specific heat capacity, differing in virgin rock temperatures (VRT), as described in Table 6-2, namely, the VRT of them were 323 K, 338 K and 353 K, respectively. Therefore, we can lead to the conclusion that the additions of EPA in shotcrete can reduce the heat loads, and the virgin rock temperatures do not influence the heat load reduction ratios. This finding has explored the range of using shotcrete with EPA in hot mines having different virgin rock temperatures, because the virgin rock temperatures would not affect the heat loads reduction ratios.

6.3.4 Influence of thermal properties of the rock on heat load reductions

In Figure 6-10, the influence of heat load reductions by thermal conductivity can also be figured out after comparing Rock D with Rocks A, B and C. It is

interesting to note an apparent increase in regard to heat load reduction ratios. The heat load reduction ratios range from about 4% to 55% that is higher than that in Rocks A, B and C, by applying shotcrete with EPA from 25 to 100%. This can guide us to the fact that the mines with larger thermal conductivity of rocks would be benefited more by using shotcrete containing EPA, since the increase of thermal conductivity of rocks can improve the heat load reduction effects of shotcrete with EPA.

6.3.5 Comparisons of partial-insulation tunnels

The partially-insulated case was also simulated in this study by removing the footwall shotcrete layer as illustrated in Figure 6-4(b) and Figure 6-5(c). Since this partially-insulated situation can be common due to the existence of the production and haulage activities. The schematic of heat flux vectors for tunnel cross sections can be observed in Figure 6-11. According to the comparison, we can note the fact that the fully-insulated tunnel has a more uniform heat flux distribution than that in the partially-insulated tunnel, which has a heat flux concentration on footwall without insulation. This observation can be easily understood because un-insulated wall becomes relatively more thermal conductive in comparison with other walls, heat flux can be accumulated greatly in the footwall area to achieve the energy equilibrium. Therefore, under this footwall heat flux concentration, it is of great interest to see the insulation effects

of the shotcrete containing expanded perlite aggregate (EPA) on the annual heat reduction ratio. Figure 6-12 has provided us the comparison of annual heat reduction ratios between full and partial-insulations in Rock D. It is found that the annual heat reduction ratios of partial-insulation are slightly lower than that of full-insulation. However, adequate heat reduction ratios from about 3.5% to 40% can still be achieved with EPA replacement percentage of sands from 25% to 100%. This finding on partial-insulation is in accordance with other's research results based on one long tunnel (Gilani, 2010). Similarly, partial-insulation can be compared to the situation with shotcrete fractures, which can occur in the over-stressed underground opening covered with shotcrete. In this case, the partial-insulation with one side un-insulated would be an extreme case in which the opening has lost 25% coverage due to fractures. Even with such large loss of insulation shotcrete, the insulation shotcrete still show adequate heat load reductions from above simulations.

6.3.6 Benefits estimation

The benefits of using shotcrete containing EPA can be estimated by viewing the corresponding heat load reductions in the units of kW. As shown in Table 6-4, which was from the full-insulation results of Rock D, the heat loads by using different shotcrete, and heat load reductions as well as reduction ratios were listed in this table. As from Table 6-4, the heat load reductions vary from 127 kW to

1890 kW for this whole mine level, in regard to the EPA addition percentage from 25% to 100%. In order to illustrate the cost savings for mine refrigeration, the number for operational refrigeration cost per kW per year in underground deep mines was used in a report from Canada Centre for Mineral and Energy Technology (Hall et al., 1984), and was adjusted by the factor of inflation (Statistics, 2012), then it came to \$412 per kW per year for operational refrigeration cost. We can conclude that the benefits of operational refrigeration cost savings increase with the additions of EPA into shotcrete. Shotcrete containing EPA is an economic and green way to save operational costs and reserve energy.

6.4 Conclusions

After the full three dimensional simulation of this typical mine level, we can draw the following conclusions:

1. Shotcrete containing expanded perlite aggregate can achieve very excellent heat load reduction in both full and partial-insulations, with additions of the expanded perlite aggregate.
2. Higher virgin rock temperatures and higher rock thermal conductivities may produce higher heat loads into underground openings.

3. The virgin rock temperature does not have significant influences on the heat load reduction ratio of shotcrete containing expanded perlite.

4. The mines with larger thermal conductivity of rocks would have more benefits by using shotcrete containing expanded perlite, due to the fact that the increase of thermal conductivity of rocks can improve the heat load reduction ratios of shotcrete.

Appendix

Appendix 6-1 Heat transfer coefficient calculation (After McPherson)

(McPherson and Hinsley, 1993)

Ta=28; (*The dry-bulb temperature of mine atmosphere in Celsius degree*)

TunnelW=4.3; (*Tunnel width of 4.3 m after shotcreting*)

TunnelH=4.3; (*Tunnel height of 4.3 m after shotcreting*)

Moisture=0.015;(*The assuming moisture content is 0.015 kg/kg dry air*)

StdAtkinson=0.0088;(*Standardized Atkinson friction factor (kg/m³) *)

TunnelA=TunnelW*TunnelH; (*Area of the tunnel cross section (m²)*)

TunnelPeri=2*(TunnelW+TunnelH); (*Perimeter of the tunnel cross section (m)*)

dh=4*TunnelA/TunnelPeri; (*Hydraulic diameter of the tunnel cross section (m)*)

ka=2.2348*10⁽⁻⁴⁾*(Ta+273.15)^{0.8353}; (*Thermal conductivity of air at Ta (W/(m K))*)

viscosity=(17+0.045*Ta)*10⁽⁻⁶⁾; (*Dynamic viscosity of air at Ta (Pa s)*)

density=101.325*10³/(287.058*(Ta+273.15)); (*Density of air at Ta (kg/m³)*)

Atkinson=density*StdAtkinson/1.2; (*Atkinson friction factor at Ta (kg/m³), 1.2 kg/m³ is the standard air density at 20 °C*)

f=2*Atkinson/density; (*Actual friction coefficient at Ta *)

u=Airflow/TunnelA; (*Air velocity (m/s) *)

Reynold=density*u*dh/viscosity; (*Reynolds number*)

Nu=0.35*f*Reynold/(1+1.592*(15.217*f*Reynold^{0.2}-1)/Reynold^{0.125}); (*Nusselt number*)

hc=ka*Nu/dh; (*Convective heat transfer coefficient (W/(m² K))*)

hr=22.68*10⁽⁻⁸⁾*(Ta+273.15)³; (*Radiative heat transfer coefficient (W/(m² K))*)

ab=0.104*Log[147*(3*dh)*Moisture]; (*Radiation absorption fraction*)

h[Airflow_]=hc+ab*hr; (*Heat transfer coefficient (W/(m² K))*)

Data1=Table[h[Airflow],{ Airflow,{ 10,5,5,5,10,32,5,5,37,42,32,10,20,15,5,20,65,
65,12,77,43,120,102,222,30,252,30,282,85,30,55,30,25,15,15,15,15,30,45,15,15,1
0 } }](*)Heat transfer coefficient (W/(m² K)) with respect with airflows (m³/s)*

Export["HTCoeff.txt",Data1,"Table"] (*Results output to a .txt file*)

Tables in Chapter 6

Table 6-1 Ventilation nodes and airflows

Tunnel #	From Node #	To Node #	Air Flow (m ³ /s)	Heat transfer coefficient (W/m ² K)	Length (m)
1	1	2	10	5.3	18.8
2	2	3	5	3.8	17
3	3	4	5	3.8	45.7
4	2	4	5	3.8	36
5	4	5	10	5.3	32.6
6	1	6	32	11.3	82.3
7	5	6	5	3.8	17.6
8	5	7	5	3.8	63
9	6	7	37	12.6	41
10	7	8	42	14.0	42.9
11	8	9	32	11.3	22.2
12	8	10	10	5.3	11.5
13	10	11	20	8.1	16.4
14	11	37	15	6.7	90.5
15	11	12	5	3.8	57.2
16	12	13	20	8.1	16.3
17	13	14	65	19.9	24.7
18	14	15	65	19.9	26.1
19	16	15	12	5.8	16.9
20	15	17	77	23.0	66.9
21	18	17	43	14.2	12.7
22	17	20	120	33.7	29.4
23	19	20	102	29.2	9.3
24	20	21	222	58.3	45.2
25	22	21	30	10.8	26.1
26	21	23	252	65.4	39.3
27	38	23	30	10.8	8.9
28	23	24	282	72.5	42.3
29	25	26	85	25.0	24.5
30	26	27	30	10.8	6
31	26	28	55	17.3	100.8

32	28	29	30	10.8	17.7
33	28	36	25	9.4	63.5
34	29	30	15	6.7	28.7
35	29	32	15	6.7	20.3
36	30	31	15	6.7	20.3
37	32	31	15	6.7	28.7
38	31	35	30	10.8	18
39	35	13	45	14.7	66
40	36	34	15	6.7	38.7
41	34	35	15	6.7	27.5
42	36	10	10	5.3	92.6
Total length (m)					1512

Table 6-2 Virgin rock properties

Rock	Density (kg/m ³)	Thermal Conductivity (W/(m K))	Specific heat capacity (J/kg K)	VRT (K)
A	2700.0	6.0	925.9	323.0
B	2700.0	6.0	925.9	338.0
C	2700.0	6.0	925.9	353.0
D	5011.0	19.2	518.9	353.0

Table 6-3 Shotcrete properties

Batch	Density (kg/m ³)	Thermal Conductivity (W/(m K))	Specific heat capacity (J/kg K)
CP0	2139.2	1.8	858.0
SP25	2077.2	1.4	793.6
SP50	1744.8	1.1	783.1
SP75	1653.9	0.8	735.8
SP100	751.1	0.2	641.8

Table 6-4 Benefits of shotcrete containing EPA

Batch	Heat Load (kW)	Reduction (kW)	Reduction percentage (%)	Operation cost reduction
CP0	3443.28	-	-	-
SP25	3316.06	127.22	3.69%	\$52,415
SP50	3159.78	283.50	8.23%	\$116,803
SP75	2958.03	485.26	14.09%	\$199,925
SP100	1553.26	1890.03	54.89%	\$778,691

Operational Refrigeration cost per kW per year: \$412.00; and the results of this table are based on the properties of Rock D.

Figures in Chapter 6

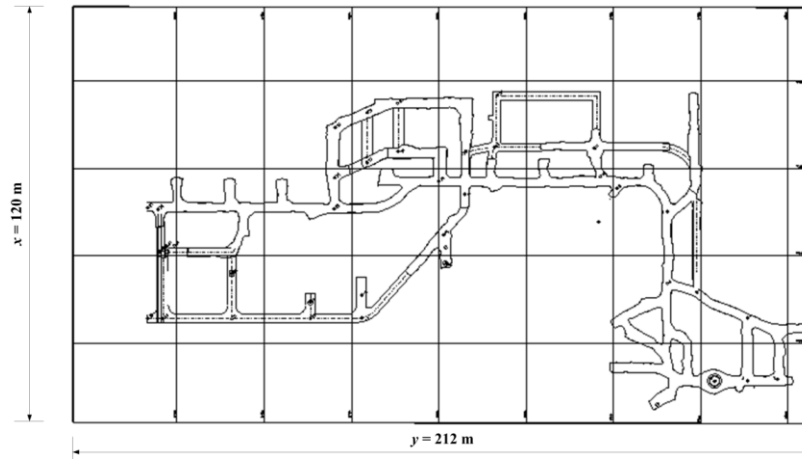


Figure 6-1 Mine tunnel layout

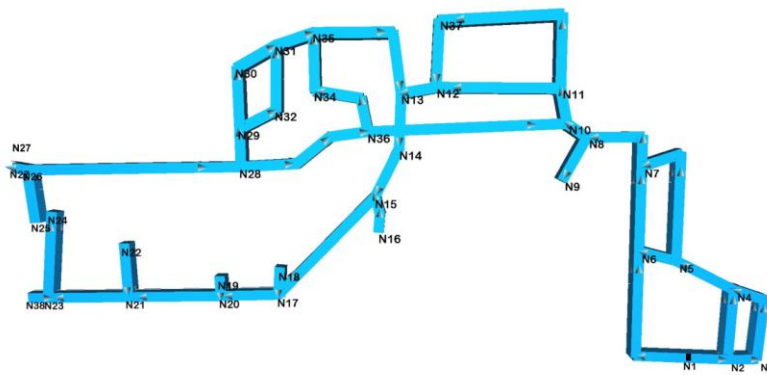


Figure 6-2 Ventilation nodes and airflow distribution

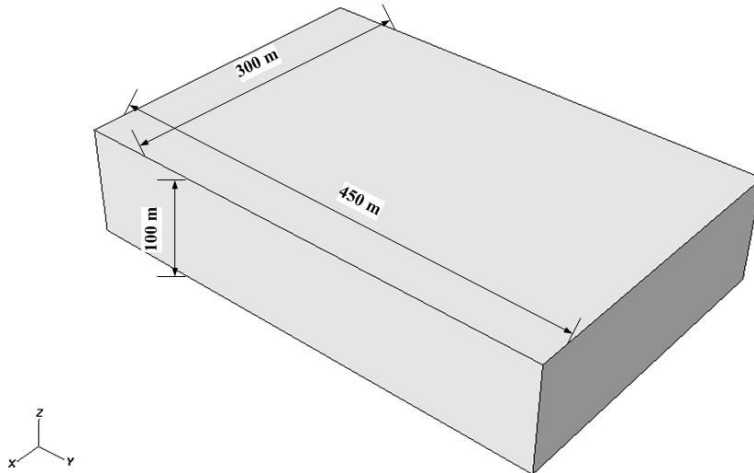


Figure 6-3 Rock mass geometry

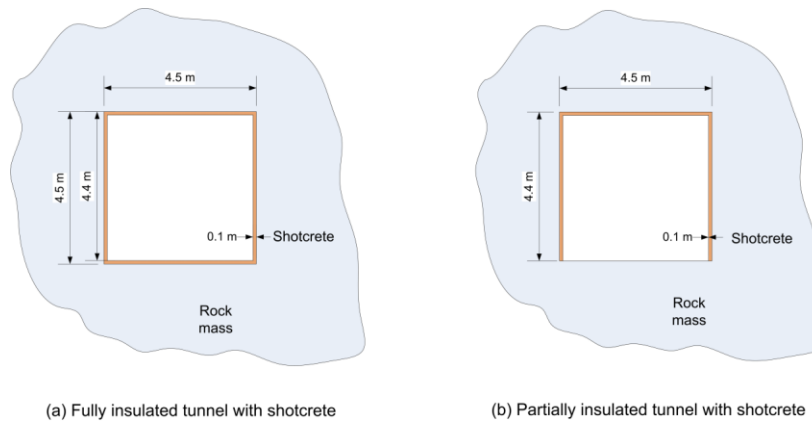
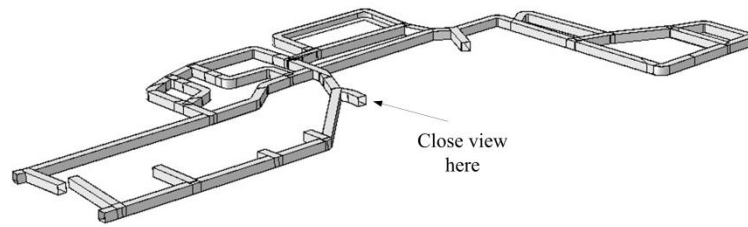
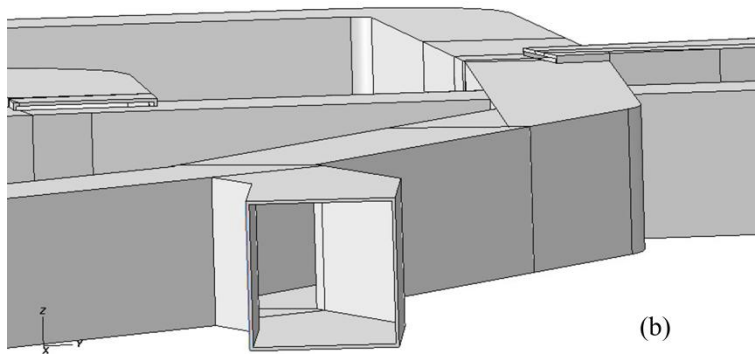


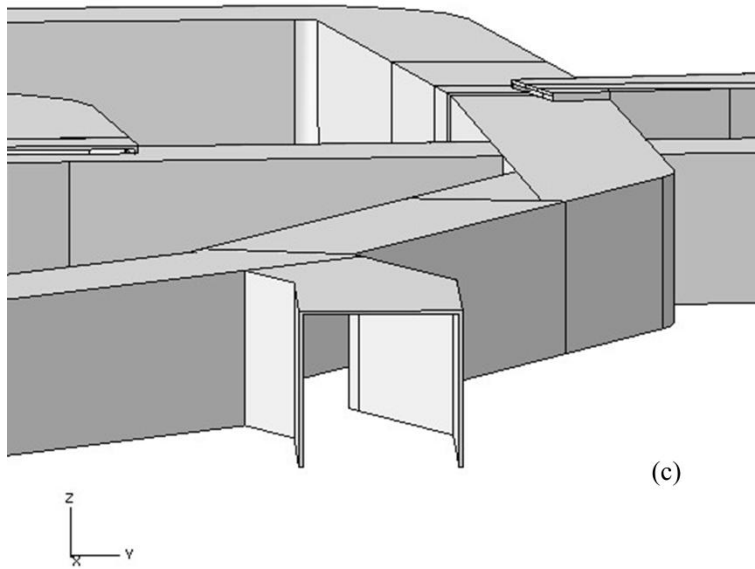
Figure 6-4 Cross section of tunnels



(a)



(b)



(c)

(a) Overview (b) Close view of fully-insulated (c) Close view of partially-insulated
Figure 6-5 Shotcrete layer

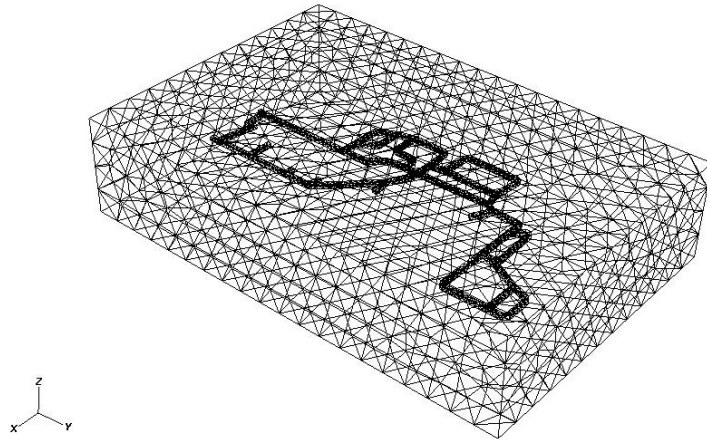


Figure 6-6 Meshing of model

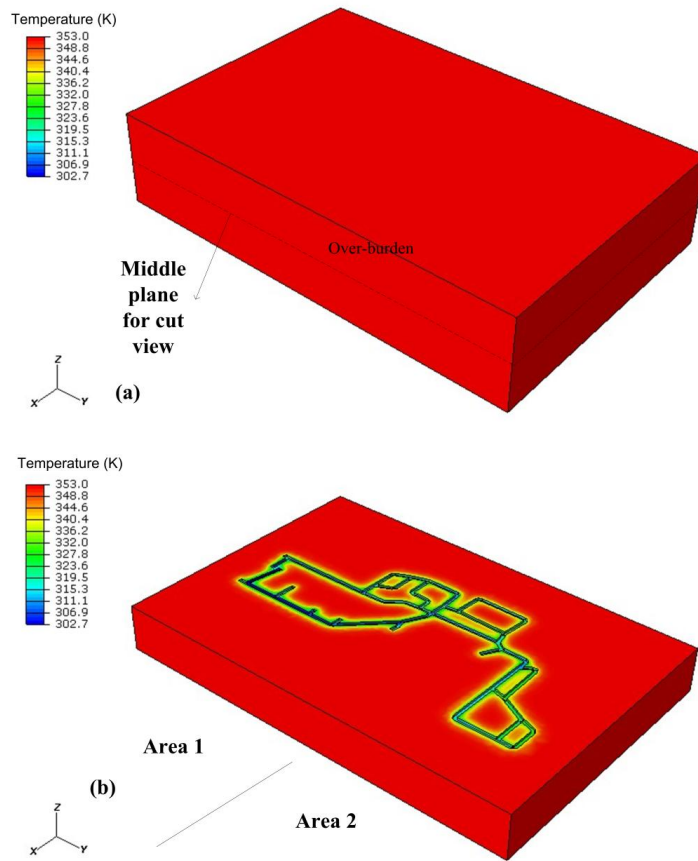
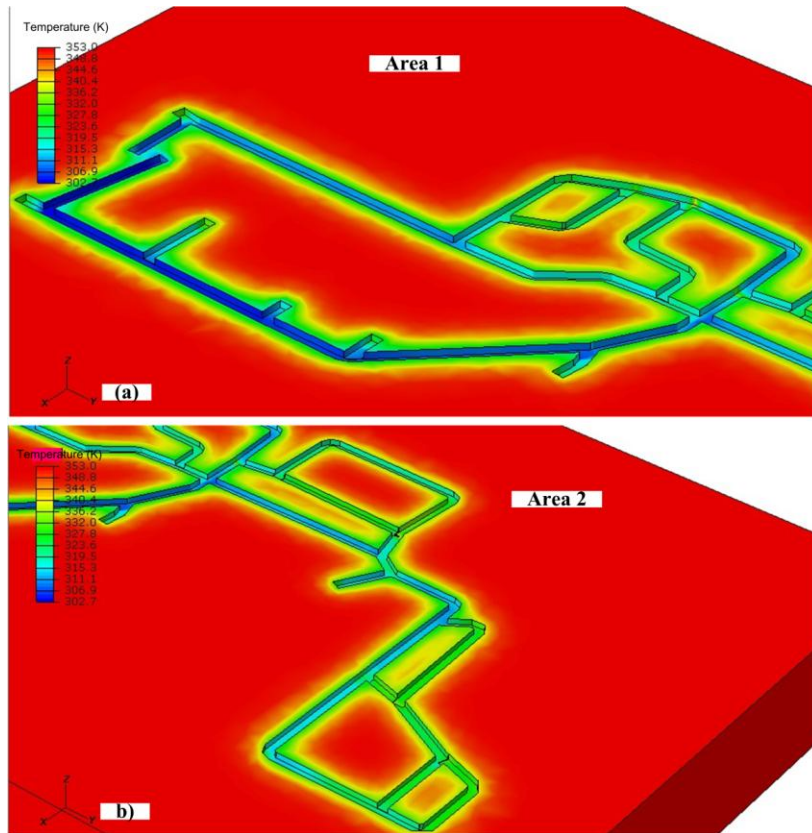


Figure 6-7 Temperature distribution



(a) Area 1

(b) Area 2

Figure 6-8 Close cut-view

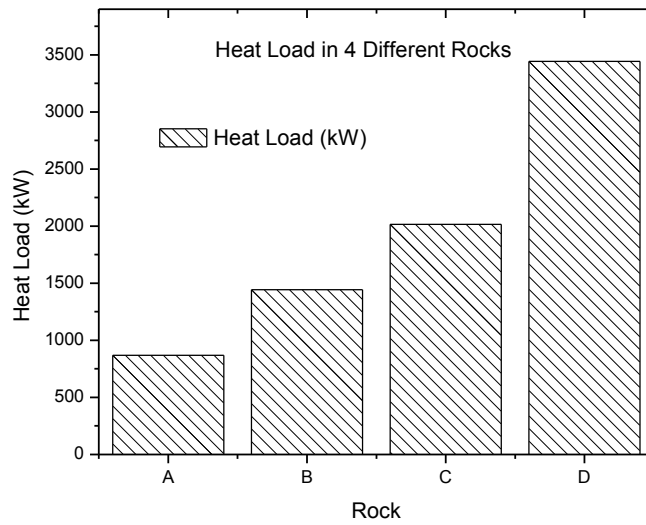


Figure 6-9 Heat load in 4 different rocks with fully-insulated shotcrete CP0

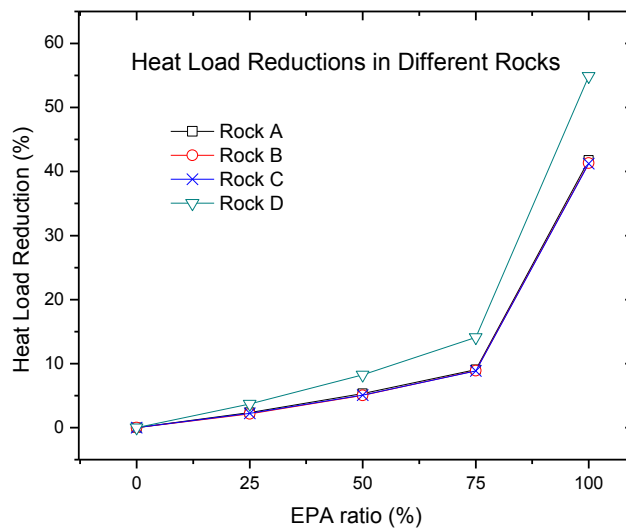
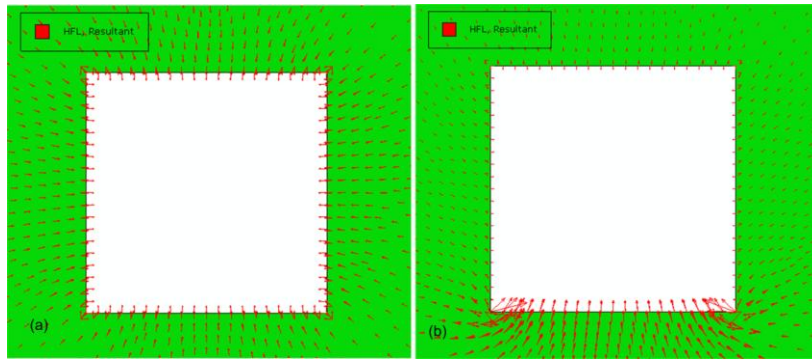


Figure 6-10 Heat load reductions in 4 different rocks with different fully-insulated shotcrete



(a) Fully-insulated

(b) Partially-insulated

Figure 6-11 Schematic of heat flux vectors

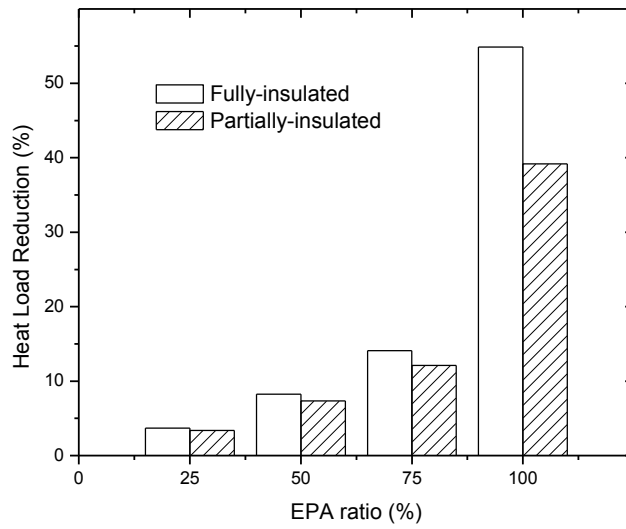


Figure 6-12 Comparison of heat load reductions in Rock D for partial-insulations

References

- Abaqus Users Manual, V. 6.10-1. *Dassault Systemes Simulia Corp., Providence, RI.*
- ADMMR (2004) Resolution Copper takes over. *Arizona Mineral Resource Newsletter.* West Washington, Arizona Department of Mines & Mineral Resource.
- Ashworth, E. (1992) Heat flow into underground openings: Significant factors. *Mining Engineering.* University of Arizona, USA.
- Bottomley, P. (1985) The reduction in heat flow due to the insulation of rock surfaces in mine airways. *2nd US Mine Ventilation Symposium.* Reno, NV.
- Bottomley, P. & van Rensburg, B. (1987) The insulation of rock surfaces-an empirical study. *Journal of the Mine Ventilation Society of South Africa,* 40, 41-45.
- Chellam, S. (1992) Thermal insulation of underground mine workings at deep levels. *Department of Mining Engineering.* Rapid City, South Dakota, South Dakota School of Mines and Technology.
- Cheng, A. H. D. & Cheng, D. T. (2005) Heritage and early history of the boundary element method. *Engineering Analysis with Boundary Elements,* 29, 268-302.
- Gilani, S. (2010) Insulation of deep and hot mines as a means of reducing heat loads. Canada, Laurentian University (Canada).
- Goto, S. & Matsubayashi, O. (2009) Relations between the thermal properties and porosity of sediments in the eastern flank of the Juan de Fuca Ridge. *Earth Planets and Space (EPS),* 61, 863.
- Hall, A. E., Mathews, K. E. & Gangal, M. K. (1984) Ventilation and refrigeration requirements and costs in deep Canadian mines. Ottawa, Ontario, Canada Centre for Mineral and Energy Technology, Mining Research Laboratories.
- Jing, L. (2003) A review of techniques, advances and outstanding issues in numerical modelling for rock mechanics and rock engineering. *International Journal of Rock Mechanics and Mining Sciences,* 40, 283-353.
- Jing, L. & Hudson, J. A. (2002) Numerical methods in rock mechanics. *International Journal of Rock Mechanics and Mining Sciences,* 39, 409-427.
- Liu, W. V., Apel, D. B. & Bindiganavile, V. (2011) Thermal characterisation of a lightweight mortar containing expanded perlite for underground insulation. *International Journal of Mining and Mineral Engineering,* 3, 55-71.

- Liu, W. V., Apel, D. B. & Bindiganavile, V. S. (2012a) Thermal properties of lightweight dry-mix shotcrete containing expanded perlite. *Indian Concrete Journal* (submitted).
- Liu, W. V., Apel, D. B., Bindiganavile, V. S. & Szymanski, J. K. (2012b) Comparison of methods in theoretical analysis of thermal insulation for underground tunnels. *CIM Journal* (under peer review).
- Liu, W. V., Apel, D. B., Bindiganavile, V. S. & Szymanski, J. K. (2012c) Theoretical study on cylindrical models of heat flow and thermo-elastic stress in underground tunnels. *Energy and Buildings* (submitted).
- Manske, S. L. & Paul, A. H. (2002) Geology of a Major New Porphyry Copper Center in the Superior (Pioneer) District, Arizona. *Economic Geology*, 97, 197-220.
- McPherson, M. J. & Hinsley, F. B. (1993) Chapter 15: Heat flow into subsurface openings. *Subsurface ventilation and environmental engineering*. Chapman & Hall London.
- Midttomme, K., Roaldset, E. & Aagaard, P. (1998) Thermal conductivity of selected claystones and mudstones from England. *Clay Minerals*, 33, 131-145.
- Pickering, A. J. & Tuck, M. (1997) Heat: sources, evaluation, determination of heat stress and heat stress treatment. *Mining Technology*, 79, 147-56.
- Prosser, B. S. & Wallace, K. G. (1999) Practical values of friction factors. *Proceedings of the 8th US Mine Ventilation Symposium*. University of Missouri, Missouri.
- Rao, K. S., Sastry, B. S. & Misra, B. (1994) Planing for insulation of mine roadways for reduction of strata heat flow into air stream. *Mine Planning and Equipment Selection 1994*.
- Rao, S. S. (2005) Chapter 16 - Three-Dimensional Problems. *The Finite Element Method in Engineering (Fourth Edition)*. Burlington, Butterworth-Heinemann.
- Rawlins, C. A. & Phillips, H. R. (2001) Reduction of mine heat loads. *7th International Mine Ventilation Congress*. Krakow, Poland.
- Reddy, J. N. & Gartling, D. K. (2010) *The finite element method in heat transfer and fluid dynamics*, Boca Raton, CRC.
- Sheer, T. J., Burton, R. C. & Bluhm, S. J. (1984) Recent developments in the cooling of deep mines. *The South African Mechanical Engineer*, 34.
- Singiresu, S. R. (2004) *The finite element method in engineering*, Elsevier Science & Technology Books
- Statistics, U. S. B. o. L. (2012) CPI Inflation Calculator. Washington, DC, http://www.bls.gov/data/inflation_calculator.htm.

- Tuck, M. A. (1997) Control of mine climate. *Mining Technology*, 79, 215-220.
- Wagner, H. (2010) The management of heat flow in deep mines / . Management von Wärmeströmen in tiefliegenden Bergwerken. *Geomechanics and Tunnelling*, 3, 609-621.

Chapter 7 Conclusion

7.1 Research summary

This research has the overall goal of developing a new type of low thermal conductive shotcrete used as thermal insulation layer on rock surfaces to reduce heat flows into underground openings, and establishing the theoretical fundamental for thermal insulation in underground space merged in the infinite rock mass.

For the insulation shotcrete developments, first, simulated shotcrete mixtures containing expanded perlite aggregate (EPA) were casted in Chapter 2 for preliminary mechanical and thermal properties. Second, in Chapter 3, based on the obtained results of Chapter 2, the field shotcreting was conducted in same mixtures for tests in mechanical and thermal properties again; comparing to the testing methods in Chapter 2, more testing methods were used in this stage for further details.

For the establishment of theoretical fundamental, first, two-layered slab models were focused in Chapter 4 in both analytical and numerical means; specifically, the analytical means is the way using closed-form solutions generated from the basic principle of heat transfer, and the numerical means comes from the finite element method (FEM) numerical simulation. Then, in Chapter 5, the cylindrical

models that are more similar to tunnels for thermal insulation were emphasized analytically and numerically for a further step to describe the heat flow into underground space. These two above steps have verified the use of FEM numerical simulation as a reliable way to describe the underground thermal insulation problem, and somehow have predicted the thermal insulation effects in their models, respectively. Finally, in Chapter 6, a full three dimensional metal mine level was numerically simulated to evaluate the heat flow reductions in both full insulation and partial insulation cases, on the basis of the thermal properties from the shotcrete containing expanded perlite aggregate (EPA).

To sum up, the developments of insulation shotcrete have given the raw data to the theoretical analysis. And the theoretical fundamental has been established targeting on the applications of insulation shotcrete. They are both core components in this research.

7.2 Conclusions

Detailed conclusions can be found in each chapter from Chapter 2 to Chapter 6, here, and more general conclusions are summarized as follows.

1. In Chapter 2, a newly developed simulated shotcrete has been developed; it is found that dramatic thermal conductivity reductions were achieved by the use of expanded perlite aggregate (EPA), in particular, 22% to 80%

thermal conductivity losses were noticed with the additions of EPA and the loss ratios of thermal conductivity are more than that of mechanical properties in the form of unconfined compressive strength (UCS) and splitting tensile strength (STS). And substantial direct tensile bond strength between various rocks and simulated shotcrete were obtained to ensure applications on rock surface.

2. In Chapter 3, the innovated shotcrete has been developed. The unconfined compressive strength (UCS) and splitting tensile strength (STS) of most shotcrete samples were found to be larger than that of cast samples in Chapter 2. The shotcreting process did not have obvious effects on the samples' thermal conductivity and diffusivity, namely, better compaction did not have obvious effects on concrete and shotcrete's thermal conductivity (k) and diffusivity (α).
3. In Chapter 4, after detailed slab model comparisons, theoretical descriptions of the thermal insulation on infinite rock mass have been fully achieved. Numerical simulation has been verified together with slab models.
4. In Chapter 5, cylindrical models were utilised to depict the heat flows into circular tunnels located in infinite rock mass. Numerical simulation has been verified together with cylindrical models.

5. In Chapter 6, after the full three dimensional simulation on a real metal mine insulated by the developed shotcrete, it is concluded that shotcrete containing expanded perlite aggregate (EPA) can achieve very excellent heat load reduction in both full and partial-insulations, with additions of the expanded perlite aggregate. And the virgin rock temperature does not have influence on the heat load reduction ratio of shotcrete containing EPA.

7.3 Contributions

This research mainly has two areas of contributions, namely, the area of insulation materials and the area of insulation theory.

As the area of insulation materials, the non-toxic, non-flammable shotcrete has been developed as the thermal insulator; this shotcrete has the benefits of low thermal conductivity, moderate unconfined compressive strength (UCS) and splitting tensile strength (STS) as well as strong bond strength to rock surfaces.

For the area of insulation theory, both slab and cylindrical analytical models have been deducted systematically to describe the complicated transient heat conduction problem in the infinite rock mass. Numerical models in either two dimensional or full three dimensional from small tunnel scale to large mine level

scale were established to evaluate the transient process of thermal insulation on the infinite rocks mass.

This research, in terms of materials and theory, mainly targets on the problems in deep hot underground mines, but is not just limited to this application. The developed shotcrete in this research can also be used in other mining or civil projects which need thermal insulation. For instance, the obtained shotcrete and theory is applicable to the insulation on tunnels in cold regions. In this case, the virgin rock temperature is very low; the insulation shotcrete can be applied as the role to prohibit heat from mine atmosphere into the cold rock mass, thus a certain amount of energy for heating up the atmosphere can be saved.

7.4 Recommendations for future research

In the areas of insulation shotcrete developments and numerical modelling of thermal insulation, some recommendations for future research based on the author's knowledge are listed as follows,

1. Non-metallic fiber reinforcements, can be considered in the insulation shotcrete mixture, since the non-metallic fiber reinforcement from one hand can improve the ductility of shotcrete, from another hand does not jeopardise the thermal resistance of the insulation shotcrete.

2. Since many underground mines are also using wet-mix shotcrete. Therefore, wet-mix shotcrete should be studied further. However, it is expected that the wet-mix shotcrete would possess similar mechanical and thermal properties in comparison with the ones obtained from cast concrete. Besides, some other kinds of lightweight aggregates similar to expanded perlite may also be introduced into the shotcrete for thermal insulation.
3. Exploring the influence of temperature (20 to 100 °C), on mechanical strength and thermal properties of insulation shotcrete.
4. The stress induced fractures or cracks on the insulation shotcrete may be studied together with the permeability as well as the relationships with thermal properties.
5. The thermal insulation in more real underground mines can be simulated in full three dimensional for the application in various mine layouts. Due to confidential requirements of mining corporations, only one name removed level was utilised in this study.
6. The rock mass used in the numerical simulation is assumed to be continuous, homogeneous, isotropic and elastic for simplification. Inversely, the rock mass in reality is discontinuous, non-homogeneous,

anisotropic and non-elastic. Thus, further improvements of numerical simulation are required.

7. Scale model platform can be established to study the underground insulation effects. Furthermore, experimental study can be conducted for heat loads from the underground hot mines applied with the developed insulation shotcrete.